A thesis
entitled

"THE ADSORPTION OF ALKALI METALS ON AN ALUMINIUM (111) SURFACE"

by

STEPHEN DAVID PARKER, B.Sc., A.R.C.S.

Submitted for the Degree of Doctor of Philosophy of
the University of London
and for the Diploma of Imperial College

Imperial College of Science and Technology
London
1983

ABSTRACT

LEED, AES, work function and EELS are used to study the adsorption of potassium and caesium on Aluminium (111). The results are compared with existing data for the adsorption of Sodium on Al (111) and Al (100) where behaviour that is not typical of alkali metal adsorption has been observed.

The adsorption of K on Al (111) produces exactly the same sequence of diffraction pattern changes as has been observed for the adsorption of Na on Al (111) where it was inferred that $(\sqrt{3} \times \sqrt{3})R30°$ structures are formed by coverages of 1/3 monolayer and domains of p(2x1) are formed by coverages of 1/2 monolayer. These structures appear to grow in 2-dimensional islands and the work function variation with coverage for both K and Na adsorption does not pass through the characteristic minimum that is observed during alkali metal adsorption on other metal substrates.

Electron energy loss spectroscopy was used to study the Potassium 3p core level excitation threshold, and it is deduced that the potassium atoms are essentially neutral at all coverages, which is consistent with the observed 2-dimensional island growth.

However, the LEED pattern changes that occurred after the formation of the K $(\sqrt{3} \times \sqrt{3})R30°$ structure were not accompanied by an expected increase in the potassium coverage, and the explanation of the final diffraction pattern in terms of domains of p(2x1) is incompatible with a hard sphere model based on metallic radii - even for Na on Al(111). It is possible that residual contamination in the alkali metal fluxes may be responsible for the final structure, although no direct evidence for this has been obtained. The formation of

an unexpected surface alloy or reconstruction, however, could also explain the behaviour.

The adsorption of Cs on Al(111) displays behaviour that is more typical of alkali metal adsorption and the results imply a coverage dependent charge transfer.

CONTENTS

Page

INTRODUCTION

This thesis concerns the adsorption of alkali metals on metals. In particular, potassium and caesium have been adsorbed on Al(111) and the results are compared with the existing data for the adsorption of sodium on Al(111) and Al(100). Many studies have been made of the adsorption of alkali metals on transition metals, where the trends are qualitatively well understood; however, very little experimental work has been done on the adsorption of alkali metal on aluminium. This seems to be because there is little commercial interest in such a system: aluminium is too soft to be used as a base for thermionic emitters, and it has low catalytic activity. Much theoretical work, however, has been done on the alkali metal - aluminium system, either implicitly, by the use of 'jellium models', which are more applicable to 'free electron metals' or explicitly, where simple s or p states or band structure has been taken into account.

The sparse amount of existing experimental data is on the adsorption of sodium on Al(111) and Al(100), where anomalous behaviour has been observed, i.e. contrary to what is expected from the adsorption of alkali metals on transition metals and from the simple theories of alkali metal chemisorption. The aim of this project is to see if the anomalous behaviour extends to the adsorption of K and Cs on Al(111) and to attempt to offer some explanation for the observed trends. The (111) orientation of the substrate was chosen since it is the most densely packed plane of a face centered cubic material and should therefore provide the best approximation to an idealized perfectly smooth surface.

The lay-out of this thesis is as follows:-

In Chapter 1 some of the theoretical aspects of alkali metal chemisorption are outlined.

The first part of Chapter 2 is a short review of the experimental data for alkali metal adsorption on transition metals and highlights some of the trends that are to be expected. The results of the existing Na/Al(111) & Al(100) study are also summarised, and in the second part of Chapter 2 is a short review on the possible effects of contamination.

The experimental set-up and the techniques used in this study are described in Chapter 3, and the experimental data is presented and discussed in Chapters 4 and 5.

Chapter 6 summarises the previous chapters and two possible explanations are offered for the observed behaviour. A recommendation for the 'next experiment' is made.

References will be found at the end of <u>each</u> chapter.

CHAPTER 1

BASIC THEORETICAL CONCEPTS

Part 1 : The theory of the work function of metals

Part 2 : The quantum mechanical picture of alkali metal adsorption

Introduction

Interest in alkali metal chemisorption is often said to originate from TAYLOR and LANGMUIR's (ref:- 1) comprehensive study of the adsorption of caesium on tungsten. They found that as caesium was adsorbed the work function of the substrate fell rapidly, reached a shallow minimum and then increased to a value close to that of bulk caesium at a coverage of about one close packed monolayer. Their "work function/coverage curve" is shown schematically in figure 1.1. The main feature of this curve is the work function minimum that occurs at sub-monolayer coverages. Prior to this work it was known that the adsorption of very small quantities of alkali metal could result in a substantial work function reduction (see references in refs:- 1,2). However, it seems that it was TAYLOR and LANGMUIR who performed the first detailed study.

Subsequently, behaviour as illustrated in figure 1.1 has been seen for other alkali metals on other transition metals (see Chapter 2) and so it would appear that the shape of the work function/coverage curve is an important characteristic of alkali metal adsorption.

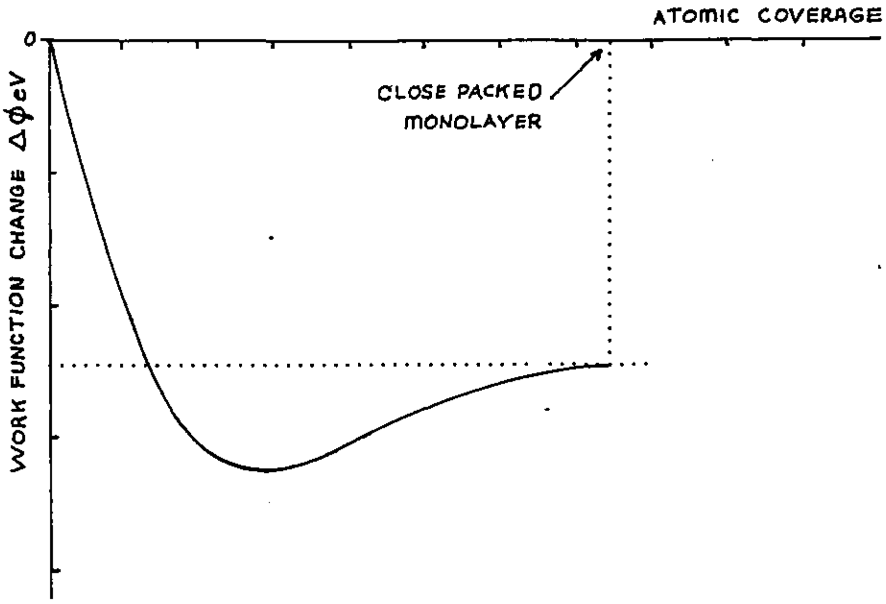

As a matter of definition the coverage, which is the number of adsorbed atoms per unit area (N_a), will often be defined relative to the number of substrate atoms per unit area of the surface plane (N_s), i.e. by $\theta = {}^{N_a}/_{N_s}$. Because the size of the adsorbed atoms will in general be larger than the size of the substrate atoms, the coverage at which the first atomic layer is completely full will often be such that $\theta_{MAX} < 1$. θ_{MAX} will be referred to as a monolayer or sometimes explicitly (and more accurately) as a saturated or close packed monolayer.

Figure 1.1: Schematic representation of the work function change on alkali metal adsorption on a transition metal.

To explain the form of the work function/coverage curve the classical model due to LANGMUIR (ref:- 3) is frequently used. In this model the metal is assumed to have a perfectly smooth conducting surface. When an alkali metal atom approaches this surface it loses its valence electron. (This loss is ascribed to the fact that the alkali metal atom has an ionization potential that is less than the substrate work function). The resulting positively charged ion is then attracted to the surface by a self induced electrostatic image potential. The ion and its image form a dipole p and a coverage of N_a alkali atoms per unit area will produce a dipole layer, which, by elementary electrostatics (ref:- 4), will change the work function by

$$\Delta\phi = -2\pi N_a p \qquad \text{(c.g.s. units.)} \qquad 1$$

Each dipole, however, is depolarised by the dipole fields due to its neighbours and this becomes progressively more important as the coverage is increased. The minimum in the work function/coverage curve is said to occur when these two opposing trends balance. Beyond the coverage at which this occurs the depolarising effects are dominant and the work function increases. Often TOPPINGS point dipole depolarisation formula (ref:- 5) is fitted to the work function/coverage curve at low coverages:

$$\Delta\phi = \frac{-2\pi N_a p_0}{1 + 9\alpha N_a^{3/2}} \qquad (\text{''} \quad \text{''}) \qquad 2$$

p_0 is the initial dipole moment and α is a polarisation parameter: both of these quantities are yielded by the fitting procedure.

While conceptually useful, LANGMUIR's picture is not satisfactory in a detailed way. The alkali metal ion is not completely ionised, even at zero coverage, and so its distance **d** from the image plane (see figure 1.2) cannot be deduced from its dipole moment alone. Further, the atomic origin of the depolarisation parameter α is not explained in the LANGMUIR model.

Figure 1.2 shows a charge **q**, a distance **d** from the image plane. This image plane is defined as the "centre of gravity" of the screening charge and in a quantitative study its location relative to the centres of the substrate ions must be known. Using the symbols of figure 1.2 LANGMUIR's dipole moment is defined by

$$p = 2dq \tag{3}$$

where 2**d** is the separation between the charge **q** and its image, -**q**.

(In fact, another definition of the dipole moment is often used where

$$p' = dq \tag{4}$$

so that equation 1 becomes

$$\Delta\phi = -4\pi N_a p' \tag{5}$$

This definition, which we will refer to as DEFINITION 2, tends to be used in more sophisticated theories as **d** is the

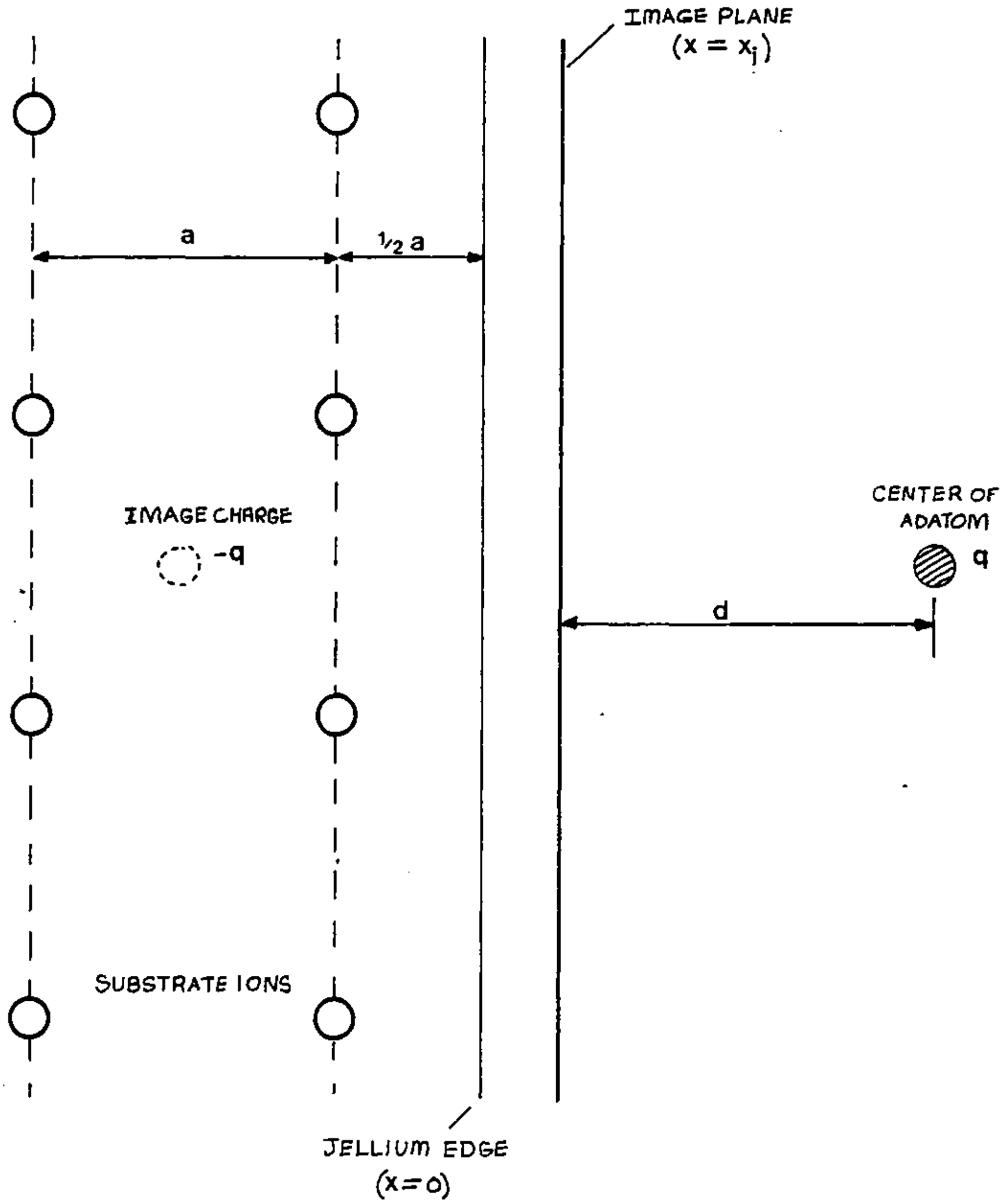

Figure 1.2: Schematic diagram defining the distances used in the text and position of the image plane w.r.t. the substrate ions and jellium edge (see later).

separation of the centre of gravities of real charge distributions. To avoid ambiguity the first definition of p will be used throughout this thesis and care will be taken to ensure that quoted values of p are consistent with this.)

Many experimental and theoretical studies have been made of alkali metal chemisorption since TAYLOR and LANGMUIR's work. The theoretical studies attempt to deal with the process in a much more rigorous way than that achieved by LANGMUIR and a quantum mechanical picture due to GURNEY (ref:- 6) is often used (see later). The experimental studies are motivated by the commercial and military advantages of low work function surfaces (such as in thermionic emitters and photocathodes) and more recently also by the effect that alkali metals have on promoting certain catalytic reactions.

Because the work function is one of the most fundamental and 'easy' to measure property of a metal surface in the first part of what follows is a discussion on the theoretical aspects of the work functions of clean metal surfaces. In the second part the quantum mechanical picture of alkali metal chemisorption will be presented, along with some theories of dealing with the work function change.

Since much work has been done on the theory of work function and chemisorption, this chapter is by no means intended to be a comprehensive review - instead it is hoped that the salient points will be found here. For more information the reader is referred to refs:- 7, 8, 9, 10, 11.

PART I

1.1 The theory of the work function of metals

As spontaneous emission of electrons from a metal has not been observed at room temperature, there must be a potential barrier at the surface of the metal that prevents the escape of electrons. This barrier is evidently of finite height since electron emission may be observed at much higher temperatures (i.e. THERMIONIC EMISSION ref:- 12) or on irradiating the metal with high energy photons (i.e. PHOTO-ELECTRIC EMISSION ref:- 13). The minimum energy required to overcome this barrier and hence place an electron at rest at "infinity" (see later) is called the work function. In general, different metals have different work functions (e.g. ref:- 8).

At absolute zero of temperature we may formally define the work function as the energy difference between two states of the whole metal crystal. In the initial state, the crystal is assumed to be in its ground state (Energy = E_N) with the N positive lattice charges exactly neutralised by N electrons. In the final state one electron has been removed and placed at rest at "infinity", leaving behind a system of (N-1) electrons which is again assumed to be in its ground state (energy = E_{N-1}). Therefore the work function is :-

$$\phi = \{E_{N-1} + \varphi(\infty)\} - E_N \qquad 6$$

where $\varphi(\infty)$ is the potential energy of the electron that has been removed to "infinity".

At finite temperatures a more general expression may be obtained by noting that (ref:- 7)

$$E_N - E_{N-1} \longrightarrow \mu \qquad N \rightarrow \infty \tag{7}$$

where μ is the chemical potential of the system. Therefore:-

$$\phi = \varphi(\infty) - \mu \tag{8}$$

It is useful to express the chemical potential relative to some electrostatic potential, $\bar{\varphi}$, that is a characteristic of the bulk crystal:-

$$\mu = \bar{\mu} + \bar{\varphi} \tag{9}$$

so that the work function expression becomes

$$\phi = \{\varphi(\infty) - \bar{\varphi}\} - \bar{\mu} \tag{10}$$

We can illustrate the usefulness of this form of writing the work function by using a semi infinite uniform background or jellium model for the metal (e.g. ref:- 7). In this model the real periodic lattice of positive ion cores is replaced by a featureless uniform background (of the same average charge density) defined by

$$n^+(\vec{r}) = n^+(x) = \begin{cases} n^+: & x \leq 0 \\ 0: & x > 0 \end{cases} \tag{11}$$

so that the jellium surface lies in the (y-z) plane, see figure 1.3. This choice of background allows us to restrict the following equations to just one dimension: x.

In the jellium model the average electrostatic potential of the bulk, $\langle\varphi(\vec{r})\rangle_{\mathrm{BULK}}$ is taken as the reference level $\bar{\varphi}$ i.e.

$$\bar{\varphi} = \langle\varphi(\vec{r})\rangle_{\mathrm{BULK}} = \varphi(-\infty) \qquad 12$$

and so the work function expression becomes:

$$\phi = \{\varphi(\infty) - \varphi(-\infty)\} - \bar{\mu} \equiv \Delta\varphi - \bar{\mu} \qquad 13$$

which is in accordance with our physical intuition, see figure 1.4.

If the neutralising electron density is $n(x)$ then the change in the electrostatic potential, $\Delta\varphi$ on passing through the surface region of the metal may be calculated using Poissons equation:

$$\frac{d^2\varphi(x)}{dx^2} = -4\pi\left(n(x) - n^+(x)\right) \qquad \text{(atomic units)} \qquad 14$$

(atomic units, i.e. proton charge e = mass of an electron m_e = Plancks constant $\hbar$ = 1, will be used to simplify some of the following equations).

Charge neutrality,

$$\int_{-\infty}^{+\infty}\left(n^+(x) - n(x)\right)dx = 0 \qquad 15$$

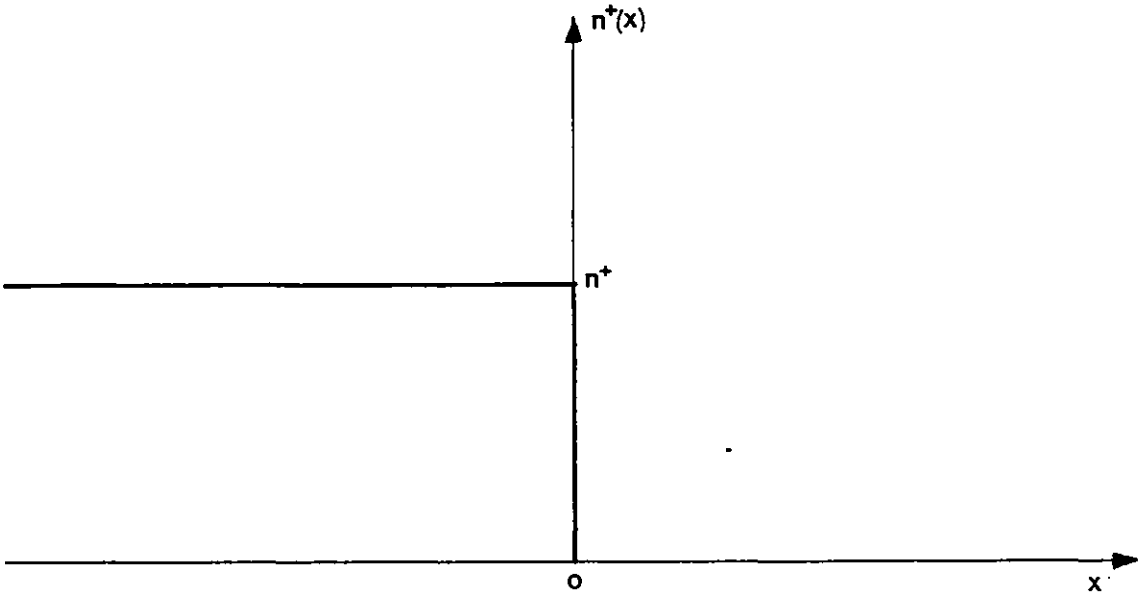

Figure 1.3: Positive charge background ($n^+(x)$) in the semi-infinite uniform background model.

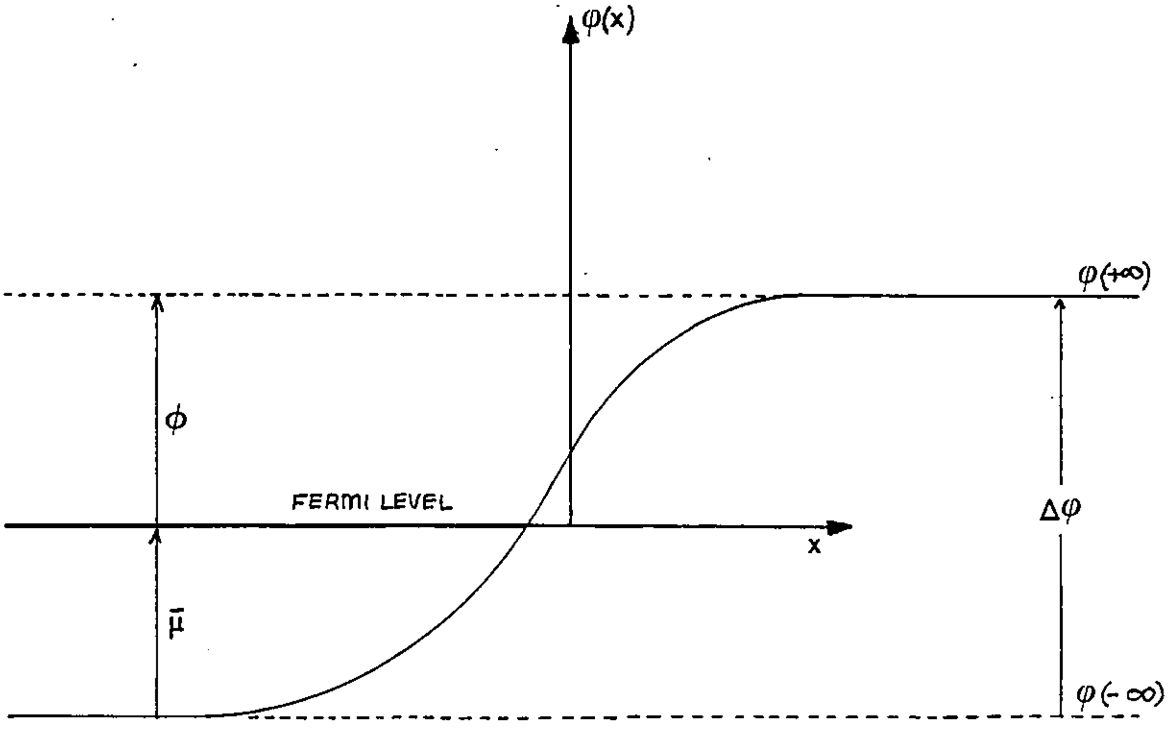

Figure 1.4: The relation between the electron work function the chemical potential $\bar{\mu}$ and the change in the electrostatic potential energy

imposes the following boundary condition on equation 14:

$$\left.\begin{matrix}\text{Limit}\\ x\rightarrow\pm\infty\end{matrix}\right\} \quad \frac{d^2\varphi(x)}{dx^2} = 0 \qquad 16$$

giving

$$\Delta\varphi = \varphi(\infty) - \varphi(-\infty) = 4\pi\int_{-\infty}^{\infty} x\left(n(x) - n^+(x)\right)dx \qquad 17$$

The integrand of equation 17 is only large in the vicinity of the surface of the metal because far inside the metal the charge densities, $n^+(x)$ and $n(x)$ must be equal, and far outside the probability of finding an electron is small. We see, therefore, that the rise in electrostatic potential on going out of the crystal is due to a <u>dipole layer located</u> at the <u>surface</u>. The physical origin of this dipole layer is the spilling out of electrons beyond the WIGNER-SEITZ cells of the surface atoms due to the non continuation of the bulk (e.g. ref:- 7).

It was WIGNER and BARDEEN (ref:- 14) who, in 1935, first made use of the fact that the work function could be split into a surface electrostatic dipole part, $\Delta\varphi$ and a bulk part $\bar{\mu}$ (equation 13) and their pioneering work on sodium has become the basis of practically all modern work function calculations for clean metal surfaces. The experimental justification for the partitioning of the work function in this way divides into two related categories:

(a) The adsorption of foreign atoms onto clean metal surfaces is known to affect the work functions. For example, we have already noted the changes that occur when alkali metals are adsorbed on transition metals.

(b) It has been observed that different crystallographic planes of the same monocrystal have different work functions (e.g. refs:- 8,15). Generally the least densely packed planes of a particular crystal possess the lowest work functions.

Since neither adsorption nor the choice of crystallographic plane can change the bulk properties of the substrate then the evidence clearly indicates that the work function must be sensitive to the surface conditions. In fact, (b), implies that there must be a macroscopic electric field outside a crystal whose surfaces have different work functions because of the contact potential difference that exists between them. Therefore one has to define the final position of the removed electron with a little more care. This position is usually taken to be at a distance from the surface that is large compared with the lattice parameters of the crystal, but small compared with the distance from adjacent crystal planes. For a planar semi infinite crystal or jellium model the distinction is of course superfluous.

From equations 13 and 17 we see that in order to calculate the work function the electron density profile at the surface and the bulk chemical potential is required. In principle calculations of the bulk chemical potential require a knowledge of the bandstructure of the metal but for the uniform background model it is given simply by

$$\bar{\mu} = \tfrac{1}{2}K_F^2 + \bar{\mu}_{xc}(n) \qquad 18$$

where K_F is the Fermi momentum and $\bar{\mu}_{xc}(n)$ is the exchange and correlation part of the chemical potential of a uniform gas of density n . $\mu_{xc}(n)$ is defined in terms of the exchange and correlation energy, $E_{xc}(n)$ by

$$\bar{\mu}_{xc}(n) = \frac{\delta}{\delta n} E_{xc}(n) \equiv \frac{\delta}{\delta n}\left(n\epsilon_x(n) + n\epsilon_c(n)\right) \qquad 19$$

where the exchange energy per electron, $\epsilon_x(n)$, for a homogeneous electron gas is given by (ref:- 16)

$$\epsilon_x(n) = -\frac{3}{4}\left(3n/\pi\right)^{1/3} \qquad 20$$

and the correlation energy per electron $\epsilon_c(n)$ for a homogeneous electron gas is usually obtained from WIGNER's interpolation formula (ref:- 16)

$$\epsilon_c(n) = \frac{-0{\cdot}056n^{1/3}}{0{\cdot}079+n^{1/2}} \qquad 21$$

For reference, the average kinetic energy per electron for a homogeneous electron gas is given by (ref:- 16)

$$T(n) = \frac{3}{10}\left(3\pi^2 n\right)^{2/3} \qquad 22$$

All of these quantities can be found once the bulk electron density of the metal is known.

The calculation of the electron density profile at the surface of a metal is, however, very much harder to perform - even for an idealised uniform background model. At the surface of the metal the electron density changes rapidly and in order to calculate it we need to know the potential that an electron sees there. Unfortunately, this potential depends not only on the positively charged ionic lattice (or background) but also on the electron density itself - because electrons lower their energy by pushing other electrons away due to exchange and correlation effects (ref:- 16). Therefore the electron density and the potential at the surface have to be calculated self-consistently and until very recently (1964) there was no satisfactory way of doing this for such an inhomogeneous electron gas.

Because of this, in WIGNER and BARDEEN's original work (ref:- 4) the surface dipole barrier was ignored incompletely, i.e. set to zero. The subsequent reasonable agreement between theory and experiment for the work function of sodium was taken as evidence that for alkali metals at least most of the work function was due to exchange and correlation effects. Because of exchange and correlation effects, in the bulk each electron is surrounded by a spherically symmetric region of "electron density depletion": a positive 'hole'. As an electron approaches the surface its 'hole' will distort and expand in directions parallel to the surface. Once the electron has left the metal, the extended 'hole' it leaves behind is just the charge distribution that gives rise to the attractive classical image potential $-e^2/4d$ where d is the distance from the image plane.

BARDEEN (ref:- 2) subsequently tried to evaluate the dipole barrier contribution to the work function of metals since for high density metals its contribution was inferred to be large. He was unable to achieve full self-consistency in his calculations but the earlier calculations of the work function of sodium were improved.

In the years that followed WIGNER and BARDEEN's work, little improvement was made to the theory and surface dipole barriers tended to be inferred by comparing computed values for the bulk chemical potential, $\bar{\mu}$, with work function measurements (see references in ref:- 8). In 1964 a new theory emerged due to HOHENBERG and KOHN (ref:- 17) called the density functional theory, whose prime objective was the treatment of strongly inhomogeneous electron gases. The theory and its application to work function calculations is described in the next section.

1.2 The density functional theory

HOHENBERG and KOHN (ref:- 17) demonstrated that the ground state energy E_v of a confined interacting electron gas can be written as a functional of the electron density $n(r)$:-

$$E_v[n] = \int v(r)n(r)\,dr + \tfrac{1}{2}\int \frac{n(r)n(r')}{|r - r'|}dr\,dr' + G[n] \qquad 23$$

In the first term on the right of this equation, $v(r)$ is a static "external" potential due, for example, to the positively charged ionic lattice of a metal crystal. The second term is the usual Hartree coulomb energy and $G[n]$

is the sum of the kinetic $\left(T[n] \right)$ exchange and correlation $\left(E_{xc}[n] \right)$ energies of the electronic system.

HOHENBERG and KOHN proved that $E_v[n]$ assumes a minimum value for the correct $n(r)$ if admissible density functions conserve the total number of electrons. Hence the ground state electron distribution can be obtained from:-

$$\frac{\delta}{\delta n}\left(E_v[n]-\mu\int n(r)dr\right) = 0 \qquad 24$$

Equations 23 and 24 are exact: self consistency is introduced through the total electrostatic potential

$$\varphi(r) = v(r) + \int \frac{n(r')dr'}{|r-r'|} \qquad 25$$

and the functional

$$G[n] = T[n] + E_{xc}[n] \qquad 26$$

In practice, however, the exchange and correlation part of $G[n]$ is not known exactly, even for a homogeneous electron gas, and so approximations have to be used. Normally a local density approximation is used (e.g. ref:- 7) where the exchange and correlation energy per electron at each point r is calculated by inserting $n(r)$ into the expressions for a uniform electron gas, equations 20, 21.

For the case of a slowly varying electron density, HOHENBERG and KOHN write

$$G[n] \simeq \frac{3}{10}(3\pi^2)^{2/3}\int n^{5/3}dr - \frac{3}{4}\left(3/\pi\right)^{1/2}\int n^{4/3}dr$$

$$-0{\cdot}056\int \frac{n^{4/3}}{0{\cdot}079+n^{1/3}}\,dr + \frac{1}{72}\int \frac{|\nabla n|^2}{n}\,dr \qquad 27$$

where the integrands of the first three terms on the r.h.s. are respectively the kinetic, exchange and correlation energies of a uniform electron gas of density n (see equations 20, 21,22), i.e. a local density approximation. The fourth term is the first term in a gradient expansion of the kinetic energy and so introduces some degree of inhomogeneity into the functional

In 1968 SMITH (ref:-18) used this form of the density functional theory to evaluate the work function of 26 metals. A semi infinite uniform background model was used for the crystal lattice (see figure 1.3).

The bulk part of the work function $\bar{\mu}$ is given by

$$\bar{\mu} = \left\langle \frac{\delta}{\delta n} G[n] \right\rangle_{BULK} \qquad 28$$

where $G[\bar{n}]$ is given by equation 27 and is therefore immediately calculable. Equivalently, equation 18 could be used.

To simplify the calculations of the electrostatic dipole barrier contribution to the work function, SMITH assumed that the electron density profile is of the form

$$n(x) = \begin{cases} n^{+} - \tfrac{1}{2} n^{+} e^{\beta x} : x < 0 \\ \tfrac{1}{2} n^{+} e^{-\beta x} \quad : x \geq 0 \end{cases} \qquad 29$$

(See figure 1.5) and so the variational procedure implied by equation 24 may be performed with respect to β . With the lowest energy electron density profile the work function is found from equations 13, 17, 28 (or 18).

SMITH was able to obtain rough agreement between theory and experiment over a wide range of metallic densities. In accordance with WIGNER and BARDEEN, he found that for low density metals (i.e. the alkali metals) most of the work function is due to exchange and correlation effects. For denser metals (e.g. aluminium) the surface dipole barrier contribution to the work function was found to be large.

In 1971 LANG and KOHN (ref:- 19) improved these jellium calculations by treating the kinetic energy quantum mechanically instead of the THOMAS-FERMI density approach used by SMITH (e.g. ref:- 7). Their form of the functional $G[n]$ is :-

$$G[n] = T[n] - \frac{3}{4}\, {}^{3}\!/_{\pi}{}^{\frac{1}{2}} \int n^{4/3}\, dr - 0{\cdot}056 \int \frac{n^{4/3}}{0\,079 + n^{1/3}}\, dr \qquad 30$$

i.e. again a local density approximation was made for the exchange and correlation contributions.

In this approach the trial density functions (for a uniform background model) are given by

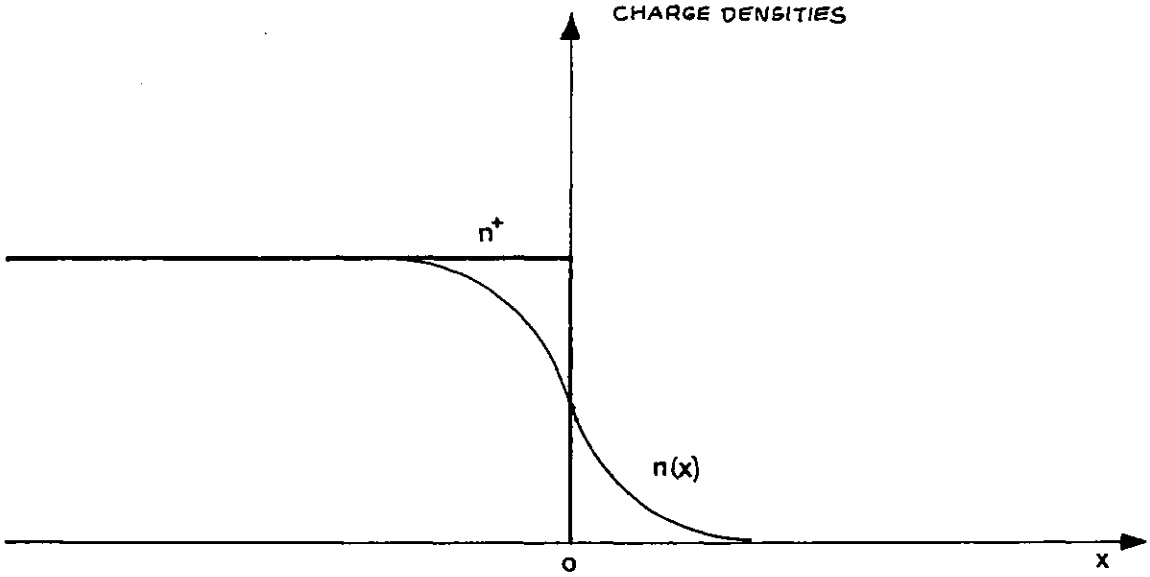

Figure 1.5: Electron charge density n(x) for the uniform background model due to SMITH (ref:- 8).

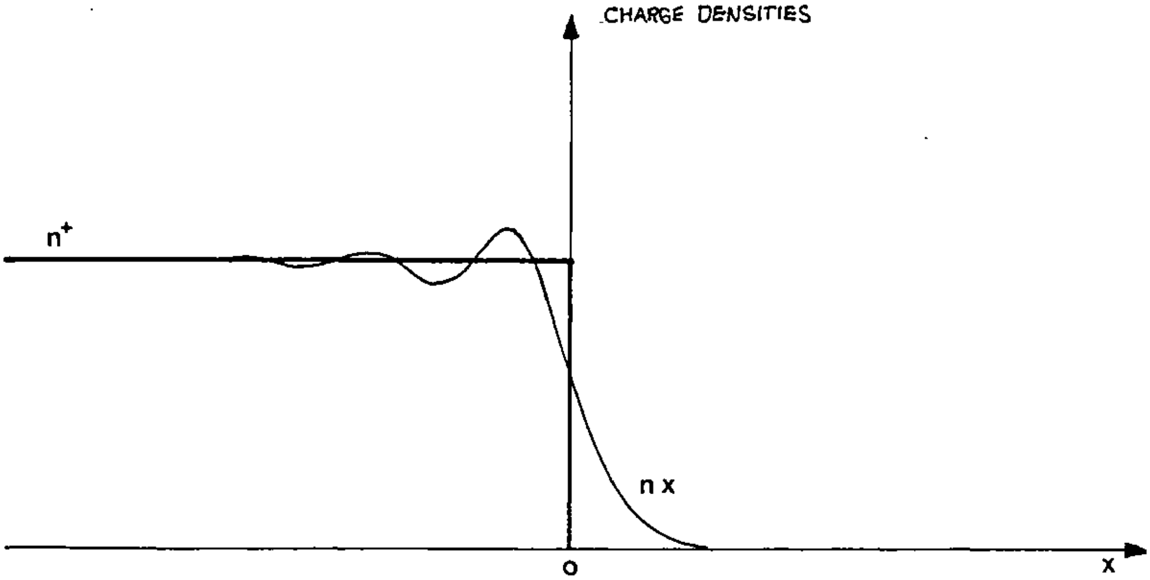

Figure 1.6: Electron charge density n(x) for the uniform background model due to LANG and KOHN (ref:- 19).

$$n(\vec{r}) \rightarrow n(x) = \sum_{i=1}^{N} |\psi_i(x)|^2 \qquad 31$$

where the one particle wave functions $\psi_i(x)$ are solutions of the auxillary equations :-

$$\left\{-\tfrac{1}{2}\frac{d^2}{dx^2} + \varphi(x) + \nu_{xc}[n(x)]\right\}\psi_i(x) = \epsilon_i\psi_i(x) \qquad 32$$

where $\varphi(x)$ is given by equation 14 and the exchange and correlation potential $\nu_{xc}[n(x)]$ is given, using equations 26 and 30, by:

$$\nu_{xc}[n] = \frac{\delta}{\delta n}\left(E_{xc}[n]\right) = \frac{\delta}{\delta n}\left(G[n] - T[n]\right) \qquad 33$$

The correct ground state electron distribution is again found from equation 24 and the work function again follows from equations 13, 17, 18.

The more accurate treatment of the kinetic energy (i.e. via equation 32) leads to FRIEDEL OSCILLATIONS (ref:- 20) in the computed electron density and a better agreement with the available experimental data. See figures 1.6, 1.7.

LANG and KOHN also went beyond the jellium approximation by reintroducing the crystallinity of the substrate into the calculation (ref:- 19). This was done by representing the real crystal by a periodic array of pseudopotentials (e.g. ref:- 21). The difference between the pseudopotentials and the jellium background was treated as

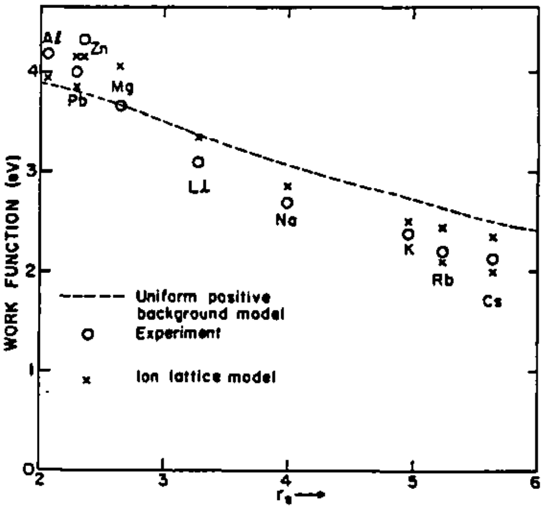

$$r_s = \left(\frac{4\langle n_{BULK}\rangle\pi}{3}\right)^{-1/3}\frac{me^2}{\hbar}$$

Figure 1.7: (from ref:- 19) Comparison of theoretical values of the work function with results of experiments on polycrystalline samples (open circles). The work function LANG and KOHN calculated using the uniform background model is shown as a dashed curve. The 'crosses' represent the work functions that LANG and KOHN calculated by reintroducing the lattice periodicity (via pseudopotentials) using first order perturbation theory. In fact, to give a fairer comparison with experiment, the crosses are the average values of the calculated work functions of the low index planes of the metals. (Two crosses are shown for the cases in which there are two possible pseudo-potential radii). The points for Zn have been shifted slightly to avoid comparison with the data for Pb.

a small periodic perturbation and the first order correction to the jellium work function was calculated. This resulted in a substantial improvement in the agreement between theory and experiment (see figure 1.7). Moreover, these new values displayed the important trend that the least densely packed planes of a particular crystal possess the lowest work functions in accordance with experiment and the semi quantitative arguments of SMOLUCHOWSKI (ref:- 22).

MONNIER and PERDEW (ref:- 23) however criticised LANG and KOHN's way of reintroducing substrate crystallinity because, for high density metals such as aluminium, the difference between an array of pseudopotentials and the jellium background is too large to be considered as a small perturbation. Instead, MONNIER and PERDEW formulate the problem by introducing the array of pseudopotentials directly into the total energy functional $E_v[n]$ (equation 23) so that now $v(r)$ has the periodicity of the bulk crystal.

The single electron wave function from which the electron density is constructed (equation 32) were generated variationally by adding to the potential in equation 32 a fictitious step potential of variable height. This adjustable potential merely served to indirectly define a class of electron density profile which were then used in the exact energy functional, $E_v[n]$, to obtain the best estimate of the ground state energy, and hence of the electron density profile itself. (In fact, in equation 32, the positive charge background was simulated using the jellium model and not the periodic pseudopotential array used in the total energy functional $E_v[n]$. This circumvents the problems involved in trying to solve equations for ψ_i which are truly three dimensional).

MONNIER and PERDEW consider their approach to be superior to that used by LANG and KOHN, especially for the higher density metal. They concede, however, that the work functions so calculated are very sensitive to their "variational electron density profiles". In a later paper this problem is avoided by using an expression for the work function that is less sensitive to the precise form of the electron density at the surface. Since the charge deficit created by the removal of an electron is located at the surface of the metal, MONNIER and PERDEW et al (ref:- 24) deduce that it should be possible to compute the work function from surface related properties alone. The expression they use is

$$\phi = \operatorname*{Limit}_{\Sigma\rightarrow 0} \frac{1}{\Sigma A}\left\{E_v[n_\Sigma] - E_v[n_{\Sigma=0}]\right\} = \left.\frac{d\sigma}{d\Sigma}\right|_{\Sigma=0} \qquad 34$$

where $n_\Sigma(r)$ is the electron density for a state in which Σ electrons per unit area, A , have been carried off to rest at $x = \infty$ leaving a surface charge density Σ behind. σ is the surface energy per unit area, A , and is that part of the total energy functional $E_v[n]$ that depends on the surface area.

Using this expression, they obtain values for the work function of simple metals that are generally even closer to the experimental values than those due to LANG and KOHN.

Recently BOHNEN and YING (ref:- 25) and ROSE and DOBSON (ref:- 26) have produced even more sophisticated analyses in which the electron density is truly 3 dimensional.

These calculations are also apparently applicable to transition metals and not just the simple metals. The treatment of the work function of clean metal surfaces has therefore become a viable theoretical proposition and it may now be argued that it is the spread in the experimental data that spoils the agreement.

PART 2

1.3 The quantum mechanical picture of alkali metal adsorption

The quantum mechanical picture of alkali metal adsorption is based on the work of GURNEY (ref:- 6). When the separation between the alkali metal atom and the metal substrate is large the interactions between them are small and so the valence state of the atom is a good eigenstate with a well defined energy E_a . At smaller separations and in particular when the alkali atom has been adsorbed, its valence wavefunction will overlap with the metallic wavefunctions and so its valence electron can tunnel into the metal. This tunnelling leads to a lifetime broadening of the atomic valence level, giving it an energy width of 2Γ . Because the alkali atom valence state is no longer well defined, any net electron density in the vicinity of the adsorbed atom is made up from electron states that are extended throughout the metal and the adatom - each contributing a small amount. Not only is the valence level broadened, but it also shifts to lower binding energies as the adatom-metal separation decreases. Both of these trends are shown schematically in figure 1.8.

In order to understand the physical origin of the

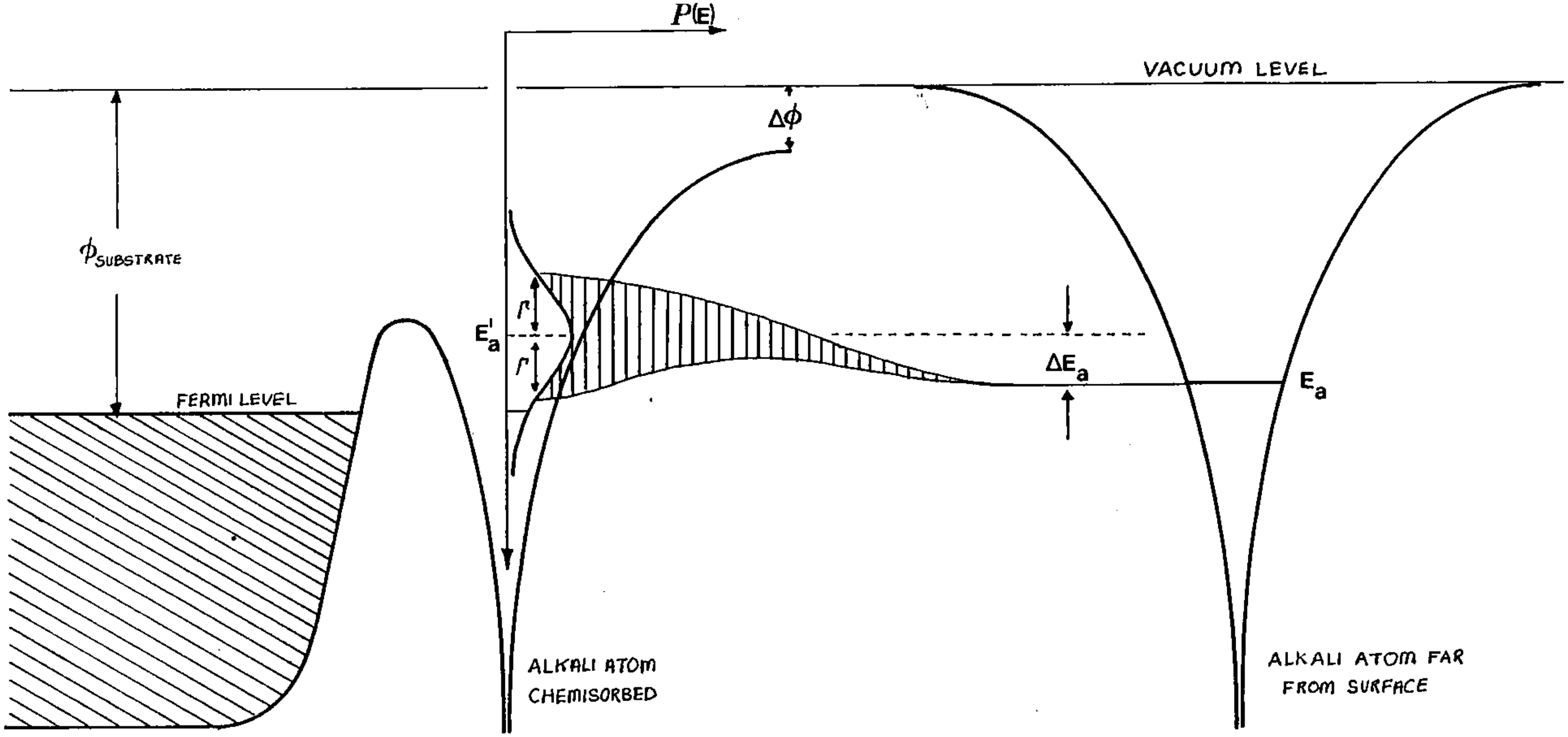

Figure 1.8: Schematic representation of energy level changes that occur when an alkali atom is chemisorbed (from ref:- 8).

atomic valence level shift, it is helpful to consider first what would happen if a core electron is removed from an isolated atom. In the initial state the core electron is in a Hartree-FOCK orbital of energy E_{HF}. When the core electron is removed the remaining electrons readjust to the presence of the positively charged hole that has been left behind. Since the resulting positive charged atom is left in a lower energy state due to the attractive hole potential, the electron which has been removed, say by photoemission with photons of energy $\hbar\omega$, emerges with an energy greater than $\hbar\omega$ above HARTREE-FOCK orbital energy. The difference in energy is called the <u>relaxation energy</u> ΔE_r so that the true binding energy is

$$E_{core} = E_{HF} + \Delta E_r \qquad 35$$

This is similar to what occurs when the alkali metal atom is adsorbed - except here the electron is not lost completely but is transferred to the metal, where it screens its own hole. The relaxation energy is again the difference between the two states. In the initial state the valence orbital is occupied prior to charge transfer, and in the final state the atom has been chemisorbed and the valence orbital is unoccupied. An estimate of the relaxation energy within the classical image approximation can be obtained, as described, for example, by GADZUK (ref:- 27).

When the valence orbital is occupied the potential energy at the point P (see figure 1.9) seen by an electron there is

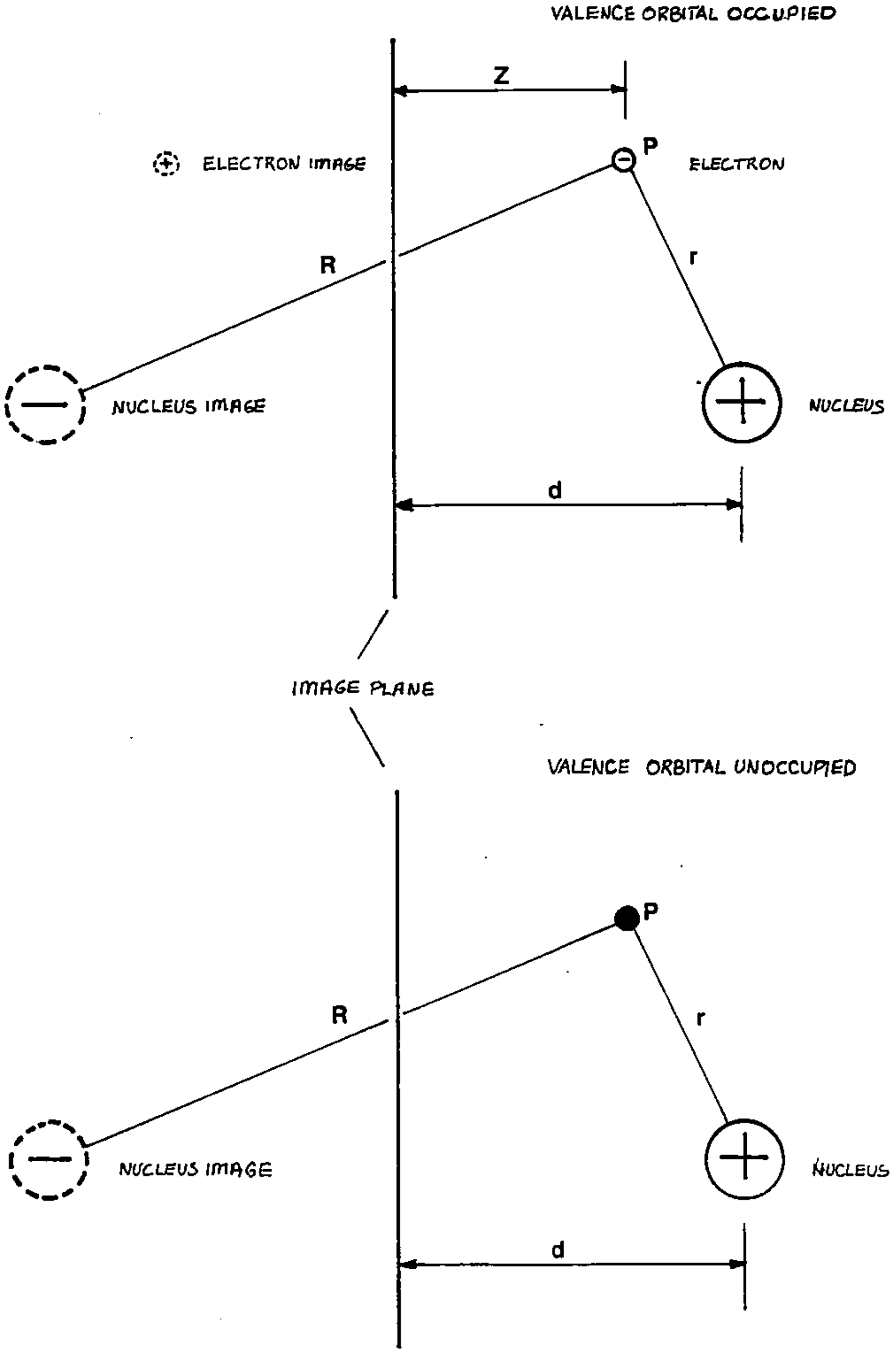

Figure 1.9: For explanation see text.

$$V_i = -\frac{e^2}{r} + \frac{e^2}{R} - \frac{e^2}{4Z} \qquad (\text{c.g.s. units}) \qquad 36$$

The first term on the right hand side of this equation is the attraction between the valence electron and the (partially screened) nucleus. The second term is the repulsion between the valence electron and the electrostatic image of the nuclear charge and the third term is the electron's attraction to its self induced electrostatic image.

When the orbital is unoccupied the image term disappears and so the potential energy at the same point is

$$V_f = -\frac{e^2}{r} + \frac{e^2}{R} \qquad (\text{"} \qquad \text{"}) \qquad 37$$

Therefore the first order energy shift of the valence level is given by

$$\Delta E_a = \langle a | V_f - V_i | a \rangle \qquad 38$$

where $| a \rangle$ is the wave function in Dirac notation of the valence state. On transforming to coordinates relative to the centre of the adatom, $z \rightarrow d + z$

$$\Delta E_a = \langle a | \frac{e^2}{4Z} | a \rangle = \langle a | \frac{e^2}{4(d+z)} | a \rangle \qquad 39$$

$$= \frac{e^2}{4d} + \frac{e^2}{4} \langle a | \sum_{j=0}^{\infty} (-1)^j \left(\frac{z}{d}\right)^j | a \rangle \qquad 40$$

The first term, which is called the "image-shift", is positive and so the atomic valence level moves upwards (see figure 1.8). The second term is much smaller and for a valence state of S-wave symmetry - as in the case of an alkali metal - it amounts to $\approx \frac{1}{10}\left(\frac{e^2}{4d}\right)$. Typically image potential shifts are of the order of 1-3 eV (e.g. ref:- 27).

From figure 1.8 we can see that the charge transfer on alkali metal adsorption will not be complete because a small portion of the broadened resonance will be below the Fermi level, in spite of the image shift, and so will be occupied. The extent of charge transfer can easily be calculated once the shape and position of the valence resonance i.e. the local density of states $P(E)$ is known. This is because the electron occupancy of the valence resonance is given by:

$$\eta = \int_{-\infty}^{+\infty} \frac{P(E)\,dE}{1+\exp\left[\frac{E-E_F}{KT}\right]} \xrightarrow{\text{Limit } T\to 0} \int_{-\infty}^{E_F} P(E)\,dE \qquad 41$$

(where E_F = Fermi energy and K and T are the Boltzmann constant and temperature respectively)
and so the effective charge on the adatom is:

$$q = e(1-\eta) \qquad 42$$

Hence if we know the local density of states at each adsorbate as a function of alkali metal coverage, then the work function change on adsorption can be calculated using equations 41, 42, 1. Within this quantum mechanical representation, LANGMUIR's depolarisation can be visualised as a downwards shift of the valence resonance caused by the mutual Coulomb repulsions between the adatoms. This shift results in a larger part of the local density of states being occupied, and so reduces charge transfer. Since the local density of states can be written as

$$P(E) = \sum_{m} |\langle a|m\rangle|^2 \delta(E-E_m) \qquad 43$$

(where $|a\rangle$ is the unperturbed atomic valence state and E_m and $|m\rangle$ are the eigenvalues and eigenfunctions of the whole interacting system) one way to calculate it is to attempt to solve the full Hamiltonian exactly for $\{E_m : |m\rangle\}$.

This was the approach used by BENNETT and FALICOV in order to try to calculate the effective charge on a single alkali atom, adsorbed on tungsten, in the presence of an externally applied electric field (ref:- 28). The immense numerical complexity that would be involved in solving the exact problem was circumvented by assuming that the substrate is a free electron metal and that the valence energy of the adsorbate could be approximated by SLATER's empirical formula (ref:- 29). In order to obtain numerical results, BENNETT and FALICOV had to make other approximations, such as the neglect of the image shift, and estimates for the adsorbate-metal separation. Unfortunately, because the parameters on which charge transfer depends:- the position and width of the valence resonance and the separation from the substrate, are all inter-related, BENNETT and FALICOV were unable to determine the charge transfer independently.

Later, BENNETT (ref:- 30) attempted to extend their formulism to the case of low but finite alkali metal coverages. Similar approximations were tried and it was found that the level of the theory still did not permit a realistic quantitative comparison with experiment.

More recently, NEWNS (ref:- 31) uses a GREENS FUNCTION method of finding the local density of states. (An excellent and straightforward account of GREENS FUNCTIONS and their use in solid state physics is given in ref:- 32). The GREENS operator for a problem, defined by the Hamiltonian, H, can be written as

$$\tilde{G}(E) = \frac{1}{(E + is - H)} \qquad : s \overset{+}{=} 0 \qquad 44$$

where E is the energy and s is a small positive quantity. The attractiveness of this approach is that once the GREENS FUNCTION is known or calculated, the local density of states is given directly as

$$P(E) = -\frac{1}{\pi} Im \langle a|\tilde{G}|a\rangle \qquad 45$$

where $|a\rangle$ is again the unperturbed adatom valence wavefunction.

MUSCAT and NEWNS (ref:- 33) use this formulism to study the alkali metal adsorption as a function of coverage. The model Hamiltonian they use is

$$H = H_0 + H_1 \qquad 46$$

In principle H_0 contains all the information concerning the interaction of a single adsorbed atom with the substrate and H_1 is the perturbation order introduced due to the presence of other adsorbed atoms. Treating this perturbation as small, so that the adsorbate retains its atomic character, the local density of states is found to be approximated by,

$$P(E) = \frac{1}{\pi} \frac{\Gamma(E)}{(E-E_a') + \Gamma^2(E)} \qquad 47$$

where E_A is the energy position of the broadened and shifted valence level and is given by:

$$E_a' = E_a + \frac{e^2}{4d} + \Lambda + W(N_a) \qquad 48$$

and

$$\Lambda + i\Gamma = \sum_m \frac{|Vam|^2}{(E-E_m+is)} \quad . \qquad 49$$

$\Gamma(E)$ is the lifetime broadening of the valence level and is related to the interaction between the metal states $|m\rangle$ and the atomic state $|a\rangle$ by Vam . Its energy dependence is expected because the tunnelling probability will depend on energy. E_a is the unperturbed, isolated alkali atom valence energy and $\frac{e^2}{4d}$ is the aforementioned image shift. Λ is a correction term to this, and $W(N_a)$ is due to the repulsive Coulomb field acting on the adsorbate due to the finite coverage (N_a atoms per unit area) of the other adsorbed alkali metal atoms.

Instead of attempting to solve equations 44 or 45 or 47 exactly, and in so doing running into the same difficulties that BENNETT and FALICOV experienced (the different formulism conceals the equivalence of their approach), MUSCAT and NEWNS determine the parameters E'_a Γ and d by a direct comparison with experiment. Thus E'_a, Γ and d are adjusted until good agreement is obtained between the theoretical result and (in the example that they used) the work function curve for caesium on tungsten. MUSCAT and NEWNS do not, in fact, attempt to predict the form of the work function/coverage curve, but try to find the various single particle properties on which it depends.

In a subsequent paper (ref:- 34) they note that for caesium the energy difference between the atomic Cs 6s and Cs 6p levels is small (≈ 1.4eV). Because the empty p_z orbital will also be broadened and shifted by the interaction with the substrate, some of it may overlap with the s resonance. (The p_{xy} orbitals are taken to lie parallel to the surface of the metal). If this occurs, then the orbitals will hybridise and so the occupancy of the p level may not be zero. Since the symmetry of the s and p states is different, then this will lead to an intra-atomic dipole moment p_{ia}, which will also tend to depolarise the surface dipole layer. The change in the work function is now given by

$$\Delta\phi = -4\pi N_a \left(q(N_a) d - p_{ia} \right) \quad \text{(DEFINITION 2)} \quad 50$$

The inclusion of the atomic p states complicates some of the previous equations, but the procedure is the same. A new parameter, λ , is introduced, which describes the degree of coupling between the s and p states. λ is also chosen by comparison with the experimental data. MUSCAT and NEWNS find that the broadening of the caesium 6s and 6p states is comparable to their energy difference and so the degree of hybridisation can be expected to be high.

The main problem with the theories just outlined is that the quantities upon which charge transfer depends cannot be calculated with sufficient accuracy to allow a <u>full</u> theoretical prediction of the experimental results. It is inevitable, therefore, that these theories end up "semi empirical". Nevertheless, the nature of the chemisorption process is emphasised in contrast to the method to be described next.

In parallel to the MUSCAT and NEWNS work, LANG (ref:- 35) considered the problem of alkali metal adsorption using the powerful density functional formulism that he and KOHN had already applied to the work function of clean metals. LANG represented the layer of adsorbed alkali by a slab of uniform positive charge density so that the single step-like background profile used earlier (equation 11) is now changed to a two step profile defined by :-

$$n^+(x) = \begin{cases} n^+ : x \leq 0 \\ n_a : 0 < x \leq D_a \\ 0 : x > D_a \end{cases} \qquad 51$$

(see figure 1.10)

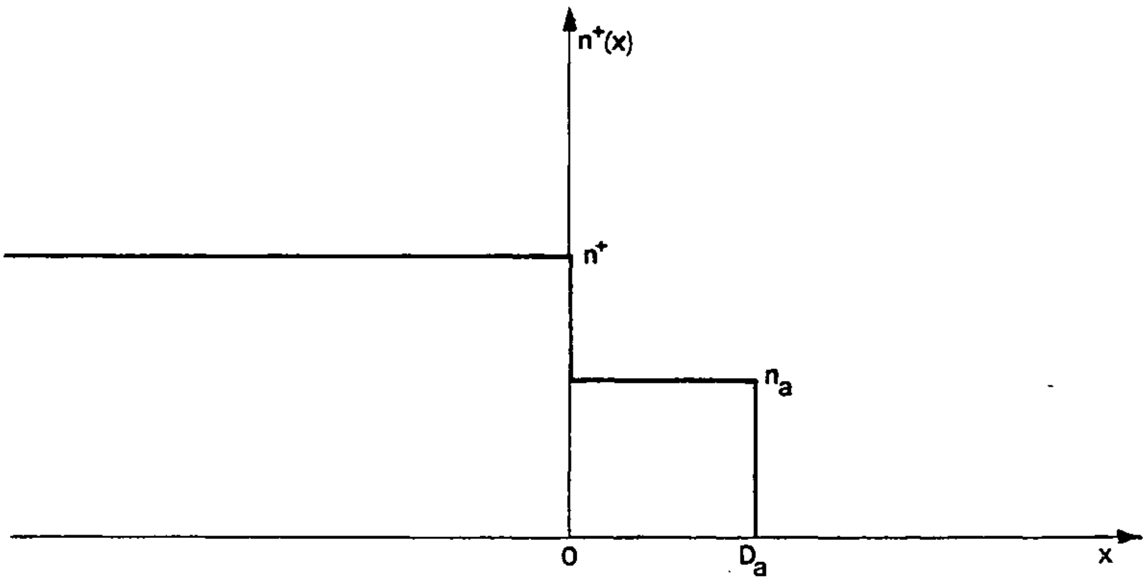

Figure 1.10: Two step background model used by LANG (ref:- 35) to generate the work function coverage curves shown in figure 1.11.

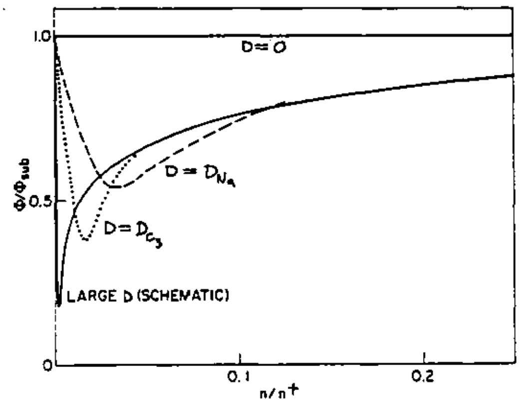

Figure 1.11: Work function/coverage curves calculated by LANG (ref:- 35). Each alkali metal is characterised by slabs of different thickness. Note axes have been normalised to substrate values.

The distance D_a is chosen to be equal to the separation between the most densely packed planes in the bulk alkali metal, i.e. each alkali metal is represented by a slab of different thickness. By varying the positive charge density n_a within the slab LANG could simulate different coverages, $N_a : N_a = n_a D_a$

The numerical procedure is just the same as before, except now there is a new positive charge profile: enough electrons are introduced to ensure overall charge neutrality and equations 23, 24, 31 and 32 are solved to obtain the lowest energy electron profile. In fact, because adsorption leaves the bulk part of the work function unaltered, once the electron density profile has been found the work function change follows from equation 17. In this way LANG could generate work function/coverage curves for each alkali on substrates of metallic densities over the entire coverage regime zero to one monolayer (see figure 1.11). The only input parameter is the thickness D_a (a = Na, K, Rb, Cs) of the jellium slab.

Not only do LANG curves display work function minima but they also show that the minimum deepens and shifts to lower coverages in the sequence Na $\longrightarrow$ Cs in qualitative agreement with the experimental data (see Chapter 2). In addition to this, LANG found that the calculated work function at one complete monolayer was to within 0.05eV of the calculated jellium work function of the bulk alkali. This is also indicated by experiment. The fact that LANG's results predict the experimental trends so well is surprising. The jellium-slab approximation for the layer of alkali metal atoms becomes poorer as the array of atoms becomes more sparse. Also, the jellium approximation for the substrate is known to be poor for transition metals (e.g. ref:- 7) and a quantitative agreement is not expected.

The main disadvantage of this approach is that most of the atomic picture of adsorption is lost. Some contact can still be made with the atomic picture, however, since the location of the image plane in relation to the substrate jellium edge (itself ½ a lattice spacing beyond the true position of the positive ion cores of the surface atoms : fig. 1.2) is at the centre of mass (x_i) of the change in the electron density ($\delta n(x)$) that occurs on alkali metal adsorption. Within the density functional theory this is given most directly by (ref:- 36):

$$x_i = \frac{\int_{-\infty}^{+\infty} x\,\delta n(x)\,dx}{\int_{-\infty}^{+\infty} \delta n(x)\,dx} \qquad 52$$

Since LANG's work little effort has apparently been made to increase the accuracy of theoretically predicted work function/coverage curves. Instead, workers tend to concentrate on single atom adsorption and calculate properties such as initial dipole moment adsorption geometries and binding energies. KAHN and YING (ref:- 37) use a variation of the density functional theorem to calculate the initial dipole moments for atoms of Na, K and Cs adsorbed on a jellium of aluminium density (see table 1.1). In fact, they also calculated the dipole moment per atom as a function of potassium and caesium coverage (see table 1.2), and by reintroducing crystallinity into their jellium background using the pseudo-potential-perturbation approach, KAHN and YING find values for the surface migration barriers for Na, K, Cs on the low index planes of aluminium (see table 1.3). These surface migration barriers are very low - certainly less than thermal energies at room temperature, and so the alkali metal atoms may be expected to be very mobile.

Table 1.1 also shows the initial dipole moments for Li and Na adsorbed on jellium of aluminium density, as calculated by LANG and WILLIAMS (ref:- 38, 39). For sodium the agreement is very good: LANG and WILLIAMS use a more sophisticated application of the density functional approach and details of this and the approach used by KAHN and YING may be found in the references given. Since both groups of workers define the dipole moment in terms of true charge distributions (i.e. DEFINITION 2; see introduction), then the values quoted in tables 1.1 and 1.2 are the "corrected" values, i.e. twice those given in the original papers.

LANG and WILLIAMS have also considered how the binding energy of an atomic core electron changes when the atom is allowed to chemisorb (ref:- 40). They point out that there are two contributions to the change in the atomic core level binding energy: a chemical shift and a

ALKALI METAL:	Li	Na	K	Cs
DIPOLE MOMENT: (DEBYE)	5.2	6.65 6.2*	10.46	16.55
REFERENCES:	38	37. 39*	37	37

Table 1.1: Calculated initial dipole moments for LiNa, K and Cs adsorbed on jellium of the same density as Al.

COVERAGE (θ) / ALKALI METAL	0	0.08	0.18	0.32	0.6
K	10.66	10.66	9.65	7.60	4.57
Cs	16.81	14.93	12.22		

Table 1.2: Dipole moments (Debye) as a function of coverage for K and Cs adsorbed on jellium of the same density as Al. From ref:- 37.

SUBSTRATE PLANE / ALKALI METAL	(111)	(100)	(110)
Na	0.13×10^{-3}	0.6×10^{-2}	0.76×10^{-2}
K	0.2×10^{-5}	0.2×10^{-2}	0.3×10^{-3}
Cs	0.5×10^{-8}	0.1×10^{-5}	0.2×10^{-5}

Table 1.3: Calculated surface migration barriers (in eV) for Na, K and Cs adsorbed on the (111), (100) and (110) planes of Al. From ref:- 37.

relaxation shift.

The charge transfer that accompanies the chemisorption of an alkali metal atom leaves the atom positively charged. The core electrons are attracted to this charge, which results in a chemical shift of the core levels to lower energies, i.e. a binding energy increase. This is the initial state and reflects the degree of charge transfer that has occurred.

When a core electron has been removed the attractive 'hole' potential lowers the atomic valence resonance through the Fermi level and so the principal final state effect is the reoccupation of the valence resonance (at least for a time given by the lifetime of the core hole). Because the remaining electrons have lowered their energy in response to the attractive 'hole' potential, this leads to a relaxation shift of the core level, as has been previously described, i.e. a decrease in the core level binding energy. For the particular case of sodium on a jellium substrate of aluminium density, the chemical shift of the 2s core level was calculated to be -1.0eV and the relaxation shift was found to be +4.5eV. The net effect is a reduction in binding energy. LANG and WILLIAMS point out, however, that it is difficult to compare these values with experimental data since measurements yield only the total shift. Nevertheless, LANG and WILLIAMS' results demonstrate the effects that final state effects could have on the core level binding energies and this will be of significance in Chapter 5.

More recently other methods have been used to study sodium on aluminium (- an apparently convenient combination of free electron metals -). For example, BENESH et al (ref:- 41) use a linearised augmented plane wave (LAPW) method to look at the properties of the c(2x2) structure that sodium forms on aluminium (100) (see Chapter 2). Their analysis yields a value for the work function change at this sodium coverage of 2.46eV which is in good agreement with the available experimental data. Unfortunately, they did not (or could not) perform their calculations at other coverages.

COX and BAUSCHLICHER (ref:- 42), using a "cluster model", study the adsorption of single atoms of sodium and lithium on aluminium (111). Both sodium and lithium are predicted to have high activation energies (>10eV) for diffusion into the substrate, but surface migration barriers, in agreement with KAHN and YING, are found to be low. Their value for the initial dipole moment of sodium is 9.5 Debye, which is in only moderate agreement with the values in table 1.1 and with the experimental value of 6.8 ± 0.1 Debye (see later).

Finally, it is worth mentioning something about the dependence of the work function on order-disorder transitions in the chemisorbed layer. So far it has been tacitly assumed that the alkali metal adatoms spread out uniformly on the surface, i.e. they do not cluster or form islands. This assumption is reasonable because the adsorbed atoms are positively charged (to some extent) and so will repel each other. Experimental results are consistent with this and show that the adsorbed atoms generally form ordered structures (see Chapter 2). MORAN-LOPEZ and TEN BOSCH (ref:- 43) have demonstrated that these ordered structures reduce the repulsive electrostatic interactions between the adsorbed ions by increasing their separation. This leads to the maximum permissible degree of charge transfer per adatom at each coverage. They show that this decreases the work function with respect to a disordered arrangement of adatoms at a given coverage, leading to a minimum in the work function/coverage curve which is not observed for totally random distribution (ref:- 44).

REFERENCES

1. G.B. TAYLOR and I. LANGMUIR, Phys. Rev. Vol. 44 p. 423 (1933)
2. J. BARDEEN, Phys. Rev. Vol. 49 p. 653 (1936)
3. I. LANGMUIR, J. Am. Chem. Soc. Vol. 54 p. 2798 (1932)
4. See for example: "Double layer" in Fundamentals of Electromagnetic Field Theory, by ZAKY and HAWLEY (HARRAP LONDON 1974)
5. J. TOPPING, Proc. Roy. Soc. (LONDON) A114 p. 67 (1927)
6. R.W. GURNEY, Phys. Rev. Vol. 47 p. 479 (1935)
7. N.D. LANG: "The Density-Functional Formulism and the Electronic Structure of Metal Surfaces" in Solid State Physics Vol. 28 ed. by H. EHRENREICH, F. SEITZ and D. TURNBULL (ACADEMIC PRESS LONDON 1973)
8. J. HÖLZL and F.K. SCHULTE: "Work Function of Metals" in Springer Tracts in Modern Physics Vol. 85 ed. by G. HÖHLER (SPRINGER-VERLAG BERLIN 1979)
9. "Interactions on Metal Surfaces", Topics in Applied Physics Vol. 4 ed. by R. GOMER (SPRINGER-VERLAG BERLIN 1975)
10. "Theory of Chemisorption", Topics in Current Physics Vol. 19 ed. by J.R. SMITH (SPRINGER-VERLAG BERLIN 1980)
11. J.P. MUSCAT and D.M. NEWNS: "Chemisorption on Metal Surfaces" in Progress in Surface Science Vol. 9 p.1 (1978)
12. See for example: "Elementary Solid State Physics" by M. ALI OMAR (ADDISON-WESLEY READING MASSACHUSETTS 1975)

13. See for example: "Introduction to Atomic Physics" by H.A. ENGE, M.R. WEHR and J.A. RICHARDS (ADDISON-WESLEY READING MASSACHUSETTS 1978)

14. E. WIGNER and J. BARDEEN Phys. Vol. 48 p. 84 (1935)

15. B.A. ROSE, Phys. Rev. Vol. 44 p. 585 (1933)

16. "Elementary Excitation in Solids" by D. PINES (W.A. BENJAMIN NEW YORK 1964)

17. P. HOHENBERG and W. KOHN, Phys. Rev. Vol. 136 No. 3B p.864 (1964)

18. J.R. SMITH, Phys. Rev. Vol. 181 No. 2 p.522 (1969)

19. N.D. LANG and W. KOHN, Phys. Rev. B. Vol. 3 No. 4 p.1215 (1971)

20. J. FRIEDEL, Supplemento Al Volume VII Serie X Del Nuovo Cimento No. 2 p. 287 (1958) 1° Trimestre

21. See for example "Principles of the Theory of Solids" by J.M. ZIMAN (CAMBRIDGE UNIVERSITY PRESS 1972)

22. R. SMOLUCHOWSKI, Phys. Rev. Vol. 60 p.661 (1941)

23. R. MONNIER and J.P. PERDEW, Phys. Rev. B. Vol. 17 p.2595 (1978)

24. R. MONNIER, J.P. PERDEW, D.C. LANGRETH and J.W. WILKINS, Phys. Rev. B. Vol. 18 No. 2 p.656 (1978)

25. K-P. BOHNEN and S.C. YING, Phys. Rev. B. Vol. 22, No. 4, p.1806 (1980)

26. J.H. ROSE and J.F. DOBSON, Solid State Commun. Vol. 37 p.91 (1981)

27. J.W. GADZUK, J. Vac. Sci. Technol. Vol. 12 No. 1 p.289 (1975)

28. A.J. BENNETT and L.M. FALICOV, Phys. Rev. Vol. 151 No. 2 p.512 (1966)

29. J.S. SLATER, Phys. Rev. Vol. 36 p.57 (1930)

30. A.J. BENNETT, J. Chem. Phys. Vol. 49 No. 3 p.1340 (1968)

31. D.M. NEWNS, Phys. Rev. Vol. 178 No. 3 p.1123 (1969)

32. "Green's Functions in Quantum Physics" by E.N. ECONOMOU, Springer Series in Solid State Sciences Vol. 7 ed. by PETER FULDE (SPRINGER-VERLAG BERLIN 1979)

33. J.P. MUSCAT and D.M. NEWNS, Solid State Commun. Vol. 11 p.737 (1972)

34. J.P. MUSCAT and D.M. NEWNS, J. Phys. C. Solid State Physics Vol. 7 p.2630 (1974)

35. N.D. LANG, Phys. Rev. B. Vol. 4 No. 12 p.4234 (1971)

36. N.D. LANG and W. KOHN, Phys. Rev. B. Vol. 7 p.3341 (1973)

37. L.M. KAHN and S.C. YING, Surface Sci. 59 (1976) p.333

38. N.D. LANG and A.R. WILLIAMS, Phys. Rev. Letts. Vol. 34 No. 9 p.531 (1975)

39. N.D. LANG and A.R. WILLIAMS, Phys. Rev. B. Vol. 18 No. 2 p.616 (1978)

40. N.D. LANG and A.R. WILLIAMS, Phys. Rev. B. Vol. 16 No. 6 p. 2408 (1977)

41. G.A. BENESH, H. KRAKAUER, D.E. ELLIS and M. POSTERNAK, Surface Sci. 104 (1981) p.599

42. B.N. COX and C.W. BAUSCHLICHER, Surface Sci. 115 (1982) p.15

43. J.L. MORÁN-LÓPEZ and A. TEN BOSCH, Phys. Rev. B. Vol. 18 No. 6 p.2555 (1978)

44. L.D. SCHMIDT and R. GOMER, J. Chem. Phys. Vol. 45 (1966) p.1605

CHAPTER 2

EXPERIMENTAL REVIEW

Part 1 : Alkali metal adsorption on metals

Part 2 : The effects of coadsorbed gases or contaminants

Introduction

The purpose of this chapter is to provide a background against which the results to be presented later in this thesis may be compared and contrasted. The emphasis will therefore be on Low Energy Electron Diffraction (LEED) and work function studies of submonolayers of alkali metal on single crystal substrates, although some mention will be made of other techniques (e.g. Thermal Desorption), which were not used in this study. The special topic of "core level excitation thresholds" will be discussed in context in Chapter 5. More information on these techniques, e.g. LEED, may be found in the texts listed in the bibliography at the end of the chapter.

The first part of this chapter is concerned with the typical trends that are observed for alkali metal adsorption on transition metals. These trends are compared with the small amount of available data on alkali metal adsorption on free electron metals (i.e. Na on Al) - for which the theories just described ought to be more applicable.

The second part of the chapter is really a reference section and helps us to recognise the effects that certain contaminants may have on the properties of the adsorbed alkali metal layers.

PART I

2.1 Alkali metals on transition metals

When submonolayers of alkali metals are adsorbed onto single crystal transition metal substrates LEED studies indicate that there is a distinct tendency to form surface structures that maximise the adatom-adatom separation, i.e. there is little evidence for island growth or nucleation. LEED observations at room temperature for low alkali metal coverages on the dense packed substrate planes ($(111)_{FCC}$, $(110)_{BCC}$, $(100)_{F/BCC}$) often show a diffuse ring pattern centred around the (0,0) diffracted beam (refs:- 1,2,3,4) and in some cases also around higher order beams (ref:- 5). Such ring patterns occur as a result of uniformly spread adatoms on the substrate plane, i.e. the standard deviation of the average adatom nearest neighbour distance is small (ref:- 5). Because of this the radius of the ring is proportional to the square root of the coverage and so will increase with increasing coverage (e.g. ref:- 1). Note: a random distribution of adatoms would only cause a uniform increase in the intensity of the background of the LEED pattern.

At temperatures much lower than 300 K these ring patterns can be resolved into a hexagonal array of diffraction spots because there is less thermal disorder (refs:- 3,6). These spot patterns expand in the same way as the ring pattern as the coverage is increased. Since this behaviour occurs even at very small adlayer densities it indicates considerable mutual repulsion between the adatoms, which is consistent with the charge transfer that characterises chemisorption.

As the coverage is increased the effects of thermal disorder (ref:- 3) become less apparent and so even at room temperature the ring patterns eventually evolve into an array of spots. At monolayer, or saturation, coverage the resulting diffraction patterns generally indicate the presence of incommensurate hexagonal close packed structures (refs :- 1,3, 5,7,8,9,10,11). In addition to the features that one would expect from a superposition of the diffraction patterns due to the substrate surface and the overlayer, multiple scattering between the layers has also been observed (refs:- 5,8). Occasionally at saturation coverage it happens that multiples of the periodicity of the substrate surface lattice are equal to multiples of the overlayer lattice constants. When this occurs there is a tendency for the overlayers to adopt certain orientations (e.g. refs:- 3,8) and sometimes domains are formed as well which can give rise to additional diffraction features (refs:- 10,11). In one system (at least) Cs on W(011) at 77K, FEDORUS & NAUMOVETS (ref:- 3) found that even though the Cs atoms formed hexagonal structures at all coverages, the orientation of the surface structure changed abruptly by 30° at a certain coverage, presumably to increase the degree of registry with the substrate. Cooling the crystal allowed them to observe such effects, but even at room temperature it is apparent that the substrate surface potential variations can influence the structure of the overlayer. This becomes even more noticeable if the size of the adsorbate is decreased, i.e. Cs ⟶ Li or atomically rougher substrate planes are chosen.

For example, GERLACH & RHODIN (ref:- 5) showed that Na on Ni(100) forms a c(2x2) structure (WOODS' notation will be used throughout ref:- 12) at saturation monolayer coverage, while ANDERSSON & JOSTELL (refs:- 1,13) found that K, because of its larger size, can only form an incommensurate hexagonal close packed structure. On the other hand, the large variations in the surface potential of the corrugated Ni(110) surface have the effect of reducing the mobility of adsorbed alkali metal atoms in directions perpendicular to the corrugations. At low coverages, even for the large Cs atom, LEED observations indicate that order is established in only one direction and the diffraction patterns show line features which are characteristic of this type of disorder (ref:- 5). At high coverages, close packed one-dimensionally-incommensurate structures are formed: registry is imposed only in the direction perpendicular to the potential (or atomic) troughs (ref:- 5).

Because of the propensity of alkali metals to form hexagonal close packed structures on the smoothest planes of many substrates, the estimated minimum separation between the adatoms is often quoted (refs:- 3,5,9,10). It turns out that in most cases there is an unexpected increase in the density of the adsorbed layers beyond that indicated by the known values of the density of the bulk alkali metals. For K on Fe(110) and Pt(100) the reverse seems to be true (ref:- 8, and reference 24 therein). It is not known why this is so.

In nearly all alkali metal adsorption studies on transition metals alloying or diffusion into the substrate has not been suspected and so alkali metal absorption seems to be vapour pressure limited (see for example ref:- 14). On vapour pressure considerations alone and under conditions of ultra high vacuum ($\approx 1 \times 10^{-10}$ Torr) only bulk lithium and bulk sodium would be stable at room temperature since their vapour pressures are below 1×10^{-11} Torr at this temperature (ref:- 15). In practice, however, it appears that up to one monolayer of K, Rb and Cs is thermally stable under normal experimental conditions: evidently this layer is stabilised by the presence of the substrate. In fact, multilayer growth of K at room temperature and 1×10^{-10} Torr was observed by THOMAS & HAAS (ref:- 2) using a potassium ion source. At room temperature the vapour pressure of K is 6 x 10^{-9}Torr. Indeed, second layer growth of even Cs (v.p. = ≈ 10^{-6}Torr at R.T.) has been observed at room temperature when a Cs ion source was used - but this second layer rapidly evaporated when the Cs-ion flux to the surface was removed (ref:- 16).

On silver substrates, however, LAMBERT et al (refs:- 17, 18,19) observed (oxygen enhanced) diffusion of Na, K, Rb into the surface. GODDARD & LAMBERT (ref:- 19) also observed the room temperature growth of a "metastable FCC rubidium crystal exposing its (111) face" on the (111) plane of silver. Considering the high vapour pressure of rubidium, 3 x 10^{-7}Torr at R.T., this structure is almost certainly impurity stabilised.

2.2 Work functions change on alkali metal adsorption

In Chapter 1 we have already noted that when alkali metals are adsorbed on transition metals the work function/coverage curve has a characteristic shape. Initial adsorption of alkali metal causes a very rapid decrease in the work function due to the dipole layer formed at the surface. Mutual depolarisation effects leads to a flattening off of the curve and then to a gentle rise to a work function value close to that of the particular alkali metal at saturated monolayer coverage. Generally speaking, the resulting minimum in the curves is most pronounced for the atomically smooth substrate planes and deepens in the sequence Na ⟶ Cs: the alkali metal coverage at which it occurs decreases in the same sequence, although it normally occurs within the range 1/2 - 3/4 closepacked monolayer. See figure 2.1 and for example references:- 1,7.

Because for very small alkali metal coverages the work function/coverage curves are linear, we may use the classical

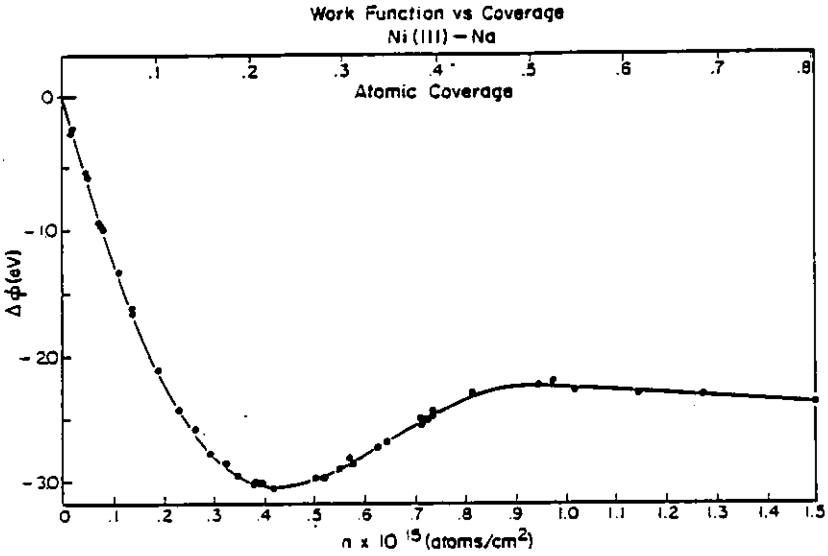

Work function versus coverage for Na on Ni (111). The work function was measured by the capacitance method.

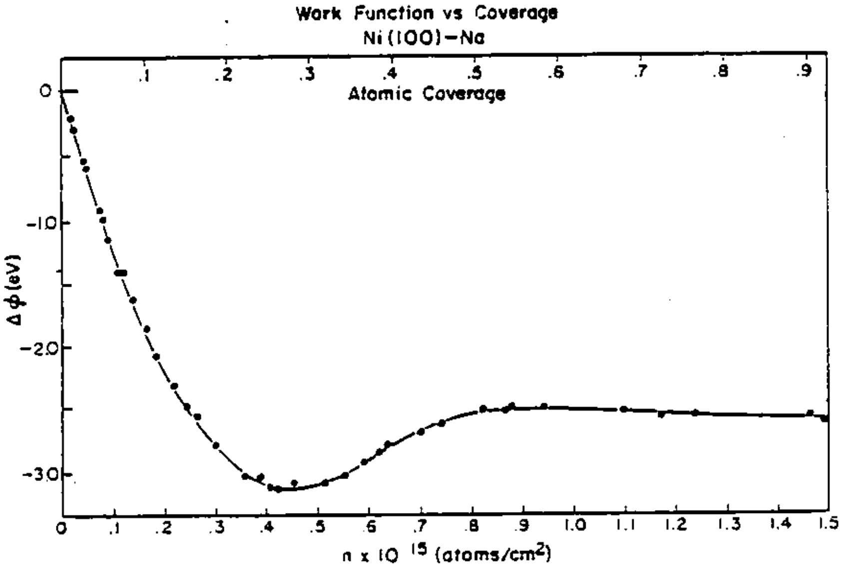

Work function versus coverage for Na on Ni (100).

Figure 2.1: The work function/coverages curves for alkali metals adsorbed on Nickel (from ref:- 14).

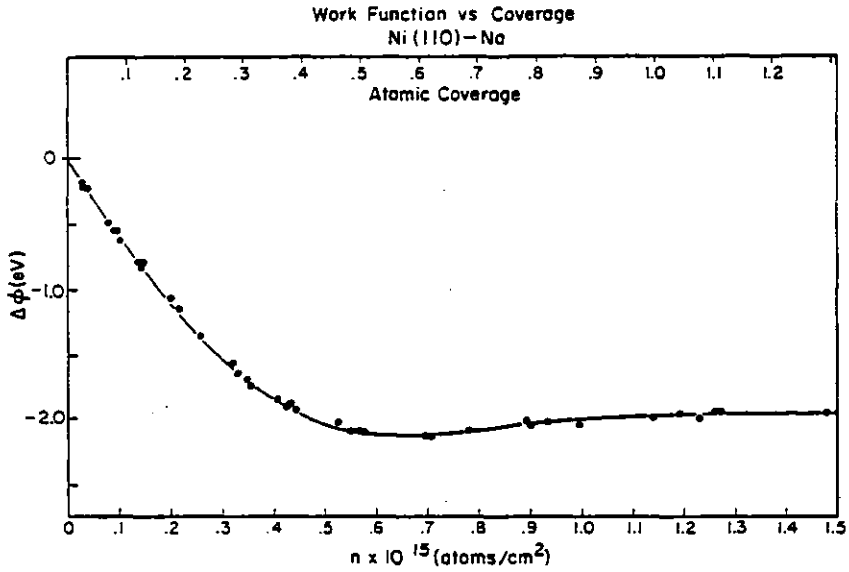

Work function versus coverage for Na on Ni (110).

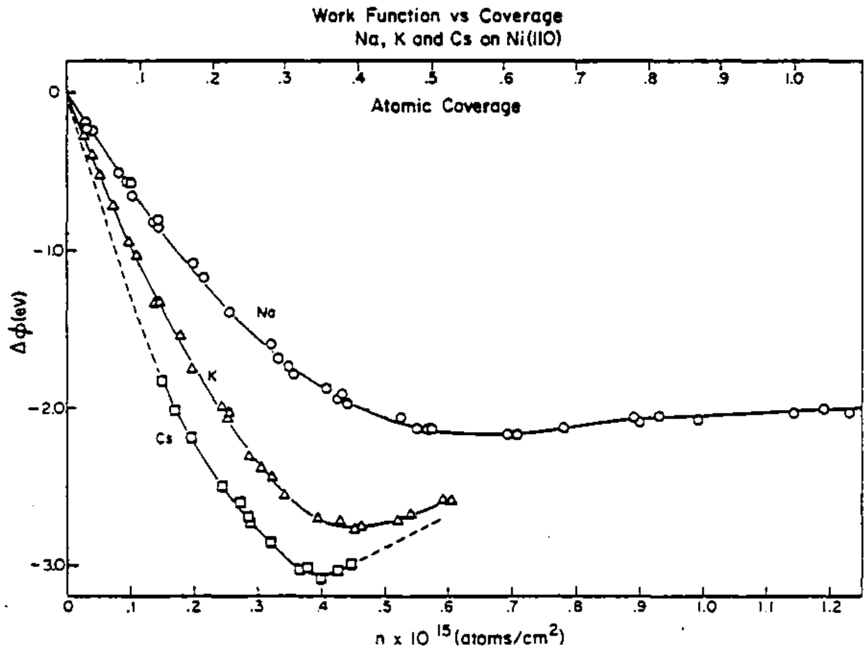

Work function versus coverage for Na, K and Cs on Ni (110).

Figure 2.1 (continued)

dipole-layer formula (ref: - 20), $\Delta\phi = -2\pi N_a p$ to obtain values for the initial dipole moments. Alternatively, by fitting TOPPINGS' (ref:- 21) point depolarisation formula :-

$$\Delta\phi = -\frac{2\pi N_a p_0}{1 + 9\alpha N_a^{3/2}}$$

to the data at low coverages, a second estimate of the initial dipole moment, p_0, may also be obtained.

Values for the initial dipole moments so obtained reflect the increase in the initial charge transfer in the sequence Na ⟶ Cs (see for example table 2.1), although they could equally imply an increase in the separation between the adatom and the screening charge (or image plane). On comparing p_0 values for the same alkali metal on different surface planes of the same substrate we see that there is a reduction in charge transfer as we increase the roughness of the surface (see table 2.1).

This indicates that the details of the classical dipole model are not quite adhered to at the distances involved. Evidently the substrate plane does not behave as a perfectly smooth electrical conductor.

2.3 The effects of temperature

Work has also been done to try and assess the temperature dependence of the work function/coverage curve (refs:- 3,6,22). In Chapter 1 it was noted that the work function minimum depends on the degree of order in the alkali metal overlayer, and this may be expected to change as the temperature of the overlayer is increased (from some arbitrary, low temperature, say). For example, order/disorder transitions may occur if sufficient

SYSTEM	P_O (EXPERIMENTAL) (DEBYE)	STRUCTURE OF SUBSTRATE	REFERENCE
Ni(111)-Na	7.4 ± 0.5	FCC	14
Ni(100)-Na	7.2 ± 0.5	FCC	14
Ni(110)-Na	3.2 ± 0.3	FCC	14
Ni(110)-K	5.3 ± 0.5	FCC	14
Ni(110)-Cs	7.0 ± 0.7	FCC	14
Fe(110)-K	13	BCC	7
Fe(100)-K	9.2	BCC	7
Fe(111)-K	8.6	BCC	7

<u>TABLE 2.1</u>

Table showing how initial dipole moments vary with substrate plane and adsorbate.

thermal agitation is present so as to destroy the long range order as evidenced by the disappearance of the adsorbate induced LEED features (refs:- 3,6,22). On cooling the diffraction patterns return: the process is reversible. If, however, the adlayer is initially disordered and heating results in the appearance of overlayer diffraction patterns, then such a process is irreversible. These annealed overlayers may now undergo order/disorder transitions, although of course at a higher temperature. Generally, for alkali metal adsorption at least, annealing is not required, even with sputter deposited monolayers or liquid nitrogen cooled substrates (ref:- 22). In fact, if anything, cooling is usually desirable (see, for example, ref:- 3) and sometimes necessary as it is for sodium on W(011) (ref:- 6).

It was found that, even though order/disorder transitions occur in relatively well defined temperature ranges, the work function remains unaltered to within experimental accuracy (refs:- 3,6,22). The short range order which governs the behaviour of the work function/coverage curve apparently persists under these conditions. The temperature required to initiate the transitions, however, increases with increasing coverage, which is consistent with statements made earlier in this chapter.

Heating the overlayers to such an extent that evaporation (i.e. desorption) occurs enables us to study the energetics of alkali metal adsorption. It appears that alkali metal thermal desorption obeys 1st order kinetics, and so the rate of desorption will be given by

$$-\frac{dn}{dt} = R(n,T) = n\nu(n)\exp\left[\frac{-\Delta H(n)}{KT}\right]$$

(see reference 14 and references 6,33 therein).

If the process of adsorption requires little or no activation energy, then ΔH appearing in the above equation will be the heat of adsorption, possibly a function of the adsorbate density, n. In principle the frequency factor ν has to be determined from Arrhenius plots. An example of this and an application of the above equation is given in ref:- 14. (In fact, there is another method of finding $\Delta H(n)$, still based on the above equation, in which the rate of desorption is not measured. Instead, use is made of the fact that the work function/coverage curve is insensitive to temperature. The heats of adsorption are then deduced from the dependence of the equilibrium work function (and hence alkali metal coverage) on temperature in the presence of a constant alkali flux to the surface. For details and an example, see ref:- 23).

Irrespective of the details of the method used, it is found or inferred that the heats of adsorption are initially quite high and decrease continuously with increasing coverage to approach the heats of both sublimations of the particular alkali metal, at one monolayer (refs:- 3,6,7,9,14,24,25,26,27). For example, GARFUNKEL & SOMORJAI (ref:- 9) found that the heat of adsorption of potassium on Pt(111) decreased from an initial (zero coverage limit) value of ≈ 60 Kcal/mole to a value of ≈ 25 Kcal/mole at one monolayer close to the heat of bulk sublimation of potassium, which is ≈ 20 Kcal/mole.

This behaviour is again consistent with the charge transfer that occurs on alkali metal adsorption: initially the heats of adsorption are high due to the strong attraction between the isolated adsorbed ions and the screening, or image charge. Mutual depolarisation increases with increasing coverages and causes a reduction in charge transfer and so also in binding energy. In addition to this, GERLACH & RHODIN (ref:- 14) demonstrated that the initial heats of adsorption (ΔH_o) reflect the increase in the initial charge transfer in the sequence Na $\longrightarrow$ K $\longrightarrow$ Cs : $\Delta H_o^{Na} < \Delta H_o^{K} < \Delta H_o^{Cs}$. They also showed that the initial heats of adsorption tend to be higher on the smoother substrate planes - a trend also displayed by the initial dipole moment - and that structure in the desorption spectra could be correlated with crystallographic changes.

Generally, then, we see that the experimental trends are predicted very well by the theories outlined in Chapter 1. Exact, quantitative agreement is not expected because of the simplifying assumptions made by the theories, i.e. - a jellium approximation for the substrate and sometimes for the adsorbate. It is not surprising, therefore, that discrepancies exist. Lithium, for example, appears to behave anomalously on the low index planes of tungsten (refs:- 23,26). This is probably because of its very small size. In fact, what is really required is a direct comparison between the theories presented in Chapter 1 and the system for which they should be most suited:- alkali metals on aluminium. So far, however, there have been only two reported studies of this system. In 1975 PORTEUS (ref:- 28) studied the adsorption of sodium on Al(111) and (100), and soon after some of his results were reproduced by HUTCHINS, RHODIN & DEMUTH (ref:- 2). The results and consequences of these studies are very important and will be discussed next.

2.4 Sodium on aluminium

When sodium was adsorbed on the Al(111) surface PORTEUS observed the sequential appearance of first a ($\sqrt{3} \times \sqrt{3}$) R30°

structure ($\theta = 1/3$) and then a LEED pattern of p(2x2) symmetry which he ascribed to 3 domains of (2x1) structure ($\theta = \frac{1}{2}$). This completed the first close packed monolayer and subsequent sodium deposition merely resulted in an apparently unstable second layer. No ring or expanding-spot patterns were seen. Instead the ($\sqrt{3}$ x $\sqrt{3}$) R30° diffraction spots appeared out of a uniform background and were visible from a coverage of $\approx \theta = 0.19$ onwards. The positions of the diffraction spots did not change, only their intensity increased with increasing coverage. By $\theta \approx 1/3$ the ($\sqrt{3}$ x $\sqrt{3}$) R30° features had reached their maximum intensity and <u>new</u> spots appeared, which, by a coverage of $\theta = 1/2$, produced the well defined (2x1) structures. During this process the diffracted beams from the ($\sqrt{3}$ x $\sqrt{3}$) R30° structure gradually disappeared and showed no sign of any movement that could be associated with a gradual evolution into the final diffraction pattern.

Just as it would appear that the ($\sqrt{3}$ x $\sqrt{3}$) R30° structure grows by some kind of island growth mechànism (ref:- 30), at least from the coverages at which it is first observable, so it seems do the (2x1) structures. Behaviour indicative of a <u>gradual</u> reduction in the Na-Na spacing is not observed - instead a 2 step process is seen.

The work function data is also anomalous and shows a <u>monotonic</u> fall from the work function of clean aluminium to a value close to that of bulk sodium by $\theta \approx 1/2$. See figure 2.2 .

The adsorption of Na on the Al(100) surface yields similar trends. In this case, <u>diffuse</u> half order diffraction beams appear at $\theta \approx 0.35$. They become fully developed by $\theta \approx 0.5$, indicating the presence of a well defined c(2x2) surface structure. Further sodium deposition causes these $\frac{1}{2}$ order beams to fade, and at $\theta \approx 0.9$ this is accompanied by the appearance of weak split

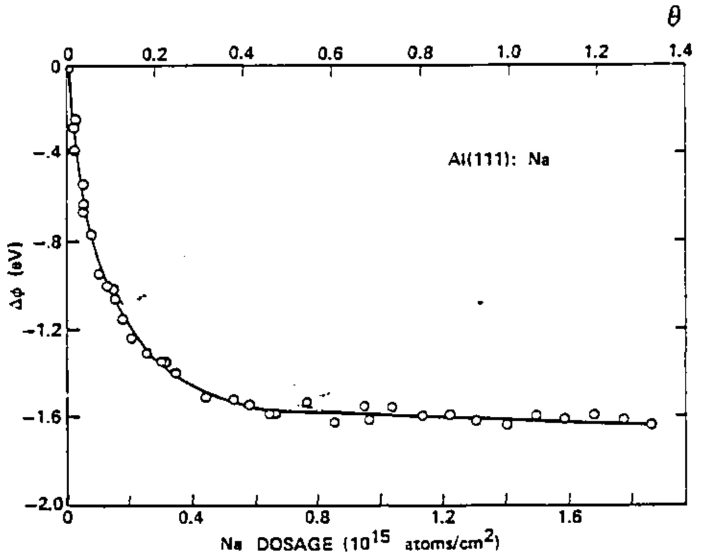

Change in work function versus Na dosage inferred from contact potential measurements on the Al(111) surface.

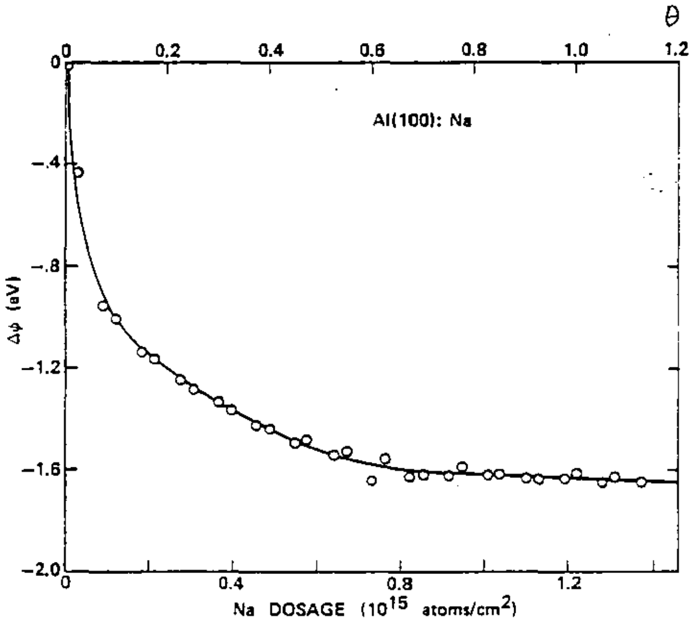

Change in work function versus Na dosage inferred from contact potential measurements on the Al(100) surface.

<u>Figure 2.2</u>
Due to PORTEUS (ref:- 28)

beams in a hexagonal pattern. Again, no ring patterns or spot movement was seen, and again the work function/coverage curve did not possess a minimum. See figure 2.2.

PORTEUS accounts for this "non characteristic" behaviour in a phenomenological manner:- evidently the depolarisation of the adlayer has occurred at a much lower coverage than is normally expected, indicating the more metallic nature of the Na-Al bond. He points out that since the depth of the minimum on the work function/coverage curve is one of the principal features used in comparing theory with experiment, then perhaps the theory needs some refinement.

However, in his study PORTEUS observes an estimated 13% oxygen contamination - could this be responsible for the observed trends or are they really indicative of more metallic bonding?

Some of the results for the (100) face were reproduced by HUTCHINS et al (ref:- 29) in their LEED intensity analysis of the c(2x2) structure. Using a different, higher purity sodium source, they observed a value for the work function at $\theta = 1/2$ to within 5% of that found by PORTEUS. Intriguingly, although they performed their experiments at -23°C (i.e. 250 K), they found that annealing to 97°C (i.e. 360 K) was required in order to obtain well defined c(2x2) structures. It has already been pointed out that annealing is not required for other substrates, even at ≈ 77 K. This in itself must say something about the relative strength of the Al-Na : Na-Na interactions.

The results of their LEED analysis places the adsorbed sodium atoms in the high coordination 4 fold hollow sites, 2.05 ± 0.1 A above the plane defined by the nuclei of the aluminium atoms in the surface. This means that the aluminium-sodium bond length is 2.86 ± 0.07 A, and this is almost equal to the Al-Al metallic bond length of 2.850 A used in their analysis. They justify the short Al-Na bond length by combining appropriate values of the known covalent bond radii of these metals. It is interesting to note, however, that if a hard-ball model is used, then the Al-Na bond length would imply that the adsorbed sodium atoms have the <u>same size</u> as the substrate aluminium atoms. HUTCHINS et al make no mention of this, and their diagram of the proposed structure is grossly out of scale.

In fact, the LEED calculations were repeated soon after by VAN HOVE et al (ref:- 31) using the same data but a different theoretical approach. Their results agreed to within 1.5% of those obtained by HUTCHINS et al.

It was the unexpected behaviour of sodium on aluminium that provided the motivation for this present study. It was expected that the larger atomic size and electropositivities of potassium and caesium would result in different surface structures and work function/coverage curves. The results of these studies will be discussed in Chapters 4, 5 and 6.

PART 2

2.5 The effects of coadsorbed gases or "contaminants"

In later chapters it will be seen that it is necessary to have some idea about how the properties of adsorbed monolayers of alkali metal could be influenced by the presence of various contaminants. The limited sensitivity of the Auger spectrometer used in this study (see Chapter 3) means that there is always the possibility of there being undetected, submonolayer amounts of, say, O, CO, N and H present in the surface region of the crystal. In an ultra high vacuum experiment there are 3 or 4 possible sources of such contaminants:

- Residual gases in the experimental chamber;
- Electron beam induced contamination, caused by cracking of residual adsorbed gas;
- Contaminants already present in the surface region of the sample due to non thorough cleaning and/or a continuous diffusion from the bulk;
- Contaminants that are present in the source of the alkali metal vapour which are subsequently co-deposited.

Fortunately, deliberate controlled coadsorption studies of alkali metals with the above gases show that the final properties of the multicomponent system are relatively insensitive to the order in which the adsorbates are introduced, providing the quantities are small, i.e. less than one monolayer. Hence, a discussion of the above sources of contamination can be limited to those which are thought to be the possible sources of alien material in this study (see Chapters 3 and 4).

Unfortunately, there is no available data dealing with the effects that O , H, N and CO could have on monolayers of alkali metals on aluminium. At best we can only draw upon existing studies of the coadsorption of O_2, H_2, N_2 and CO on transition metals - studies motivated by catalyst and thermionic emitter design - and then discuss the behaviour of "clean aluminium" surfaces to such gases. In the review that follows we will therefore regard the coadsorbed gas as a contaminant, reversing the emphasis placed on it in the original studies.

2.6 Alkali metal coadsorption with oxygen

When oxygen is adsorbed on to transition metal surfaces it is found that the presence of submonolayer or monolayer amounts of alkali metal noticeably increases the sticking coefficient (refs:- 9,32,33,34,35). On the other hand, the presence of oxygen on the substrate surface has been shown to increase the saturation density of the adsorbed alkali metal monolayer (refs:- 9,27,32,35,36): equivalently it was found that oxygenating close packed alkali metal monolayers allows more alkali metal to be subsequently adsorbed (refs:- 35,36). In addition, oxygen can thermally stabilise the alkali metal layer (see for example refs :- 9 and perhaps 19), and this can happen to such an extent that for Cs on W(110) DESPLAT & PAPAGEORGOPOULOS (ref :- 27) found that not only was a denser packed monolayer formed on oxygenated W(110), but that a second layer of Cs also started to grow at room temperature and 1.5×10^{-10} Torr!

A detailed comparison between the various systems studied is made difficult because the properties and mechanisms by which the various substrates are oxidised appears to be poorly understood and are not the same in all cases. A quite common model for oxidation, i.e. the formation of bulk substrate oxide, proceeds thus:- initial oxygen adsorption leads to a chemisorbed precursor state thought to be comprised of at most one monolayer of possibly slightly ionised oxygen atoms on the surface. With increasing oxygen exposure and perhaps temperature, there is a penetration of the oxygen into the substrate lattice, probably proceeding at least initially by a place-exchange mechanism (see, for example, ref:- 10,34) with the concomitant production of metal oxide. (This contrasts with alkali metal adsorption which is not a "chemical" process and is usually vapour pressure limited to a coverage of about a monolayer). This model seems to explain the main features of the oxidation of Fe and W, say (refs:- 33,37), but in the case of nickel a model has been postulated that requires the coexistence of chemisorbed oxygen and oxide, even at the initial stages of oxygen adsorption (refs:- 10, 34). Further, for copper, an incorporation stage following the initial chemisorption stage, although apparently distinct from oxide formation (which requires larger oxygen exposure), has been suggested (ref:- 38). The relevance of all this here is that in a coadsorption experiment the precise details of the spatial and chemical environment that the oxygen and the alkali metal eventually find themselves in have a major influence on the electronic properties of the surface regions. Since there is little chemical (e.g. spectroscopic) evidence that monolayers of alkali metals themselves form oxides under these conditions (refs;- 32,33 compared with ref:- 9) it appears that it is the substrate-oxygen interaction that dominates. This tendency has led PAPAGEORGOPOULOS et al into suggesting that alkali metal adsorption could be used as a probe to investigate the interaction between the substrate and oxygen. This approach has met with some success and is probably best exemplified in ref:- 10, but its general applicability appears at present doubtful.

Usually evidence for a chemisorbed layer of oxygen comes from work functions and LEED data. A work function increase following oxygen adsorption is interpreted in terms of a layer of oxygen atoms negatively charged to some extent (due to charge transfer from the substrate to the adsorbate) on top of the surface plane. If the adsorbed oxygen displays an ordered LEED pattern which changes with increasing oxygen exposure in such a way that indicates a reduction in the 0-0 spacing, e.g. say, p(2x2) ⟶ c(2x2), then this is usually taken as further evidence of a chemisorbed layer. The latter should be contrasted with the case of known oxide growth: here only the extent and the intensity of the oxygen induced diffraction beams change (if these are observable), which indicates island or crystallite growth (e.g. ref:- 10). When alkali metals are deposited on <u>known</u> oxidised surfaces the oxide LEED beams (if any) are unchanged, but the background intensity of the diffraction pattern increases, implying that the alkali metal forms a disordered overlayer (refs:- 27,34).

Where the presence of oxide is not suspected the chemisorption of (submonolayers) of oxygen and alkali metal often result in new structural phases that were not present in the single component systems (e.g. ref:- 34). Therefore it is not usually possible to assign the new diffraction features unambiguously in terms of those due to oxygen and those due to the alkali metal.

Thus in the case of O and Cs on W(100) (ref:- 35) it was found that for $\theta_{Cs} \lesssim 0.43$ and $\theta_O \lesssim 1$ a unique LEED pattern was produced for each dosage combination of the two adsorbates. At high coverages ($\theta_{Cs} \approx 0.4$ and $\theta_O \approx 1$) the so-called close packing test (ref:- 39) indicates that the atoms are arranged in two layers and the corresponding work function data (see later) indicates that the inner layer consists of oxygen atoms and the outer layer of caesium atoms. For O and K on Pt(111) (ref:- 9) LEED data suggests that the unit cell contains both potassium and oxygen: at high coverages the close packing test may just allow a single planar structure, although a double layer was not ruled out.

For the systems : O/Cs-Ni(100) (refs:- 10,34); O/Cs-W(100) (ref:- 35); O/Cs-Cu(100) (ref:- 36), O/Cs-W(110) (ref:- 27), where PAPAGEORGOPOULOS et al measured the work function as a function of both oxygen and caesium coverage, it was found that the typical transition metal work function/alkali metal coverage curve was considerably altered by the presence of various amounts of oxygen. In fact, the details of the resulting trends are different in each case, as is illustrated in figure 2.3. Hence, even though for each system the work function minimum is deepened as the amount of <u>chemisorbed</u> oxygen is increased, for copper, the caesium coverage at which this occurs is also increased. For nickel and tungsten substrates an opposite shift is observed.

For copper and nickel the work function at saturation caesium coverage is decreased by the presence of oxygen, for tungsten the reverse is true. Additionally, when caesium is deposited on bulk tungsten oxide, the work function is generally higher than for the chemisorbed oxygen system, for nickel oxide the work function is always lower. The comparison is further hindered by the different structures adopted by the oxides (compare refs:- 10 and 37) and the fact that in at least one system, Cs on tungsten oxide, there is evidence for caesium diffusion into the substrate at room temperature (ref:- 27) - and this would affect the work function.

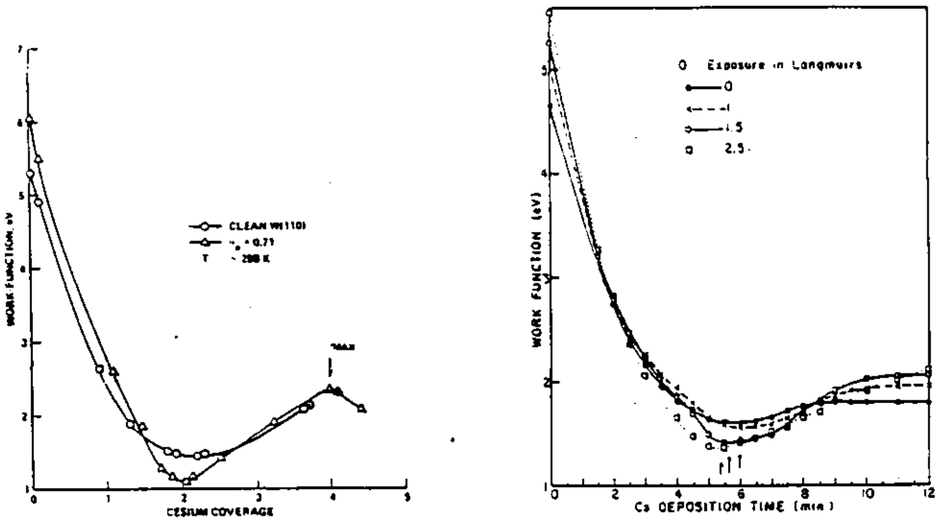

Work function versus θ_{Cs} for clean and oxygenated W(110).

Work function versus deposition time of Cs on O-covered W (100)

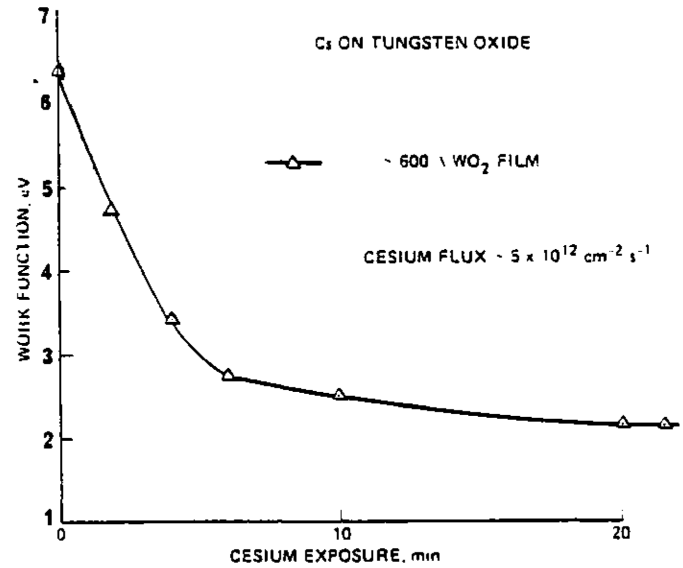

Figure 2.3: (top) The effect that the coadsorption of oxygen and caesium has on the work function of tungsten (100) and (110) planes (refs:- 27,35); (bottom) The change in the work function of tungsten oxide surfaces on Cs exposure (ref:- 27).

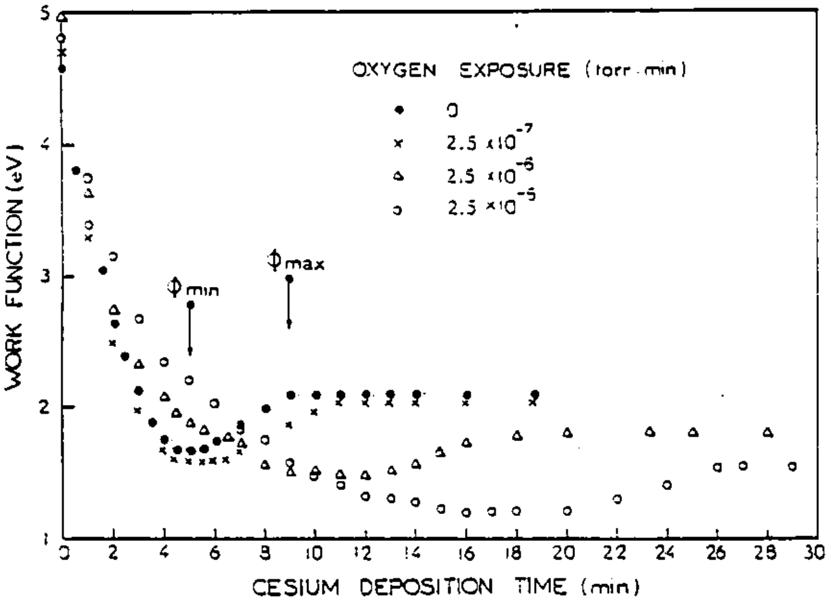

Work function vs Cs deposition time on clean and oxygen–covered Cu(100) surfaces.

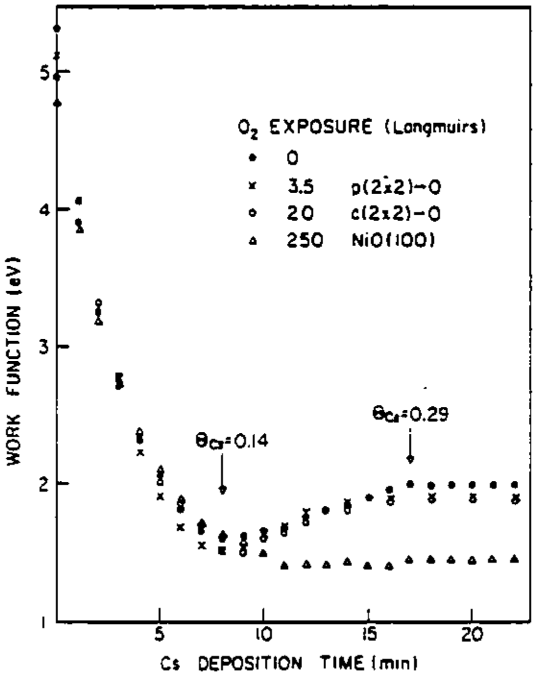

Work function curves of Cs on O-covered Ni(100) surfaces.

Figure 2.3 continued: The effects that the coadsorption of oxygen and Caesium has on the work function of Cu(100) (ref:- 36) (top) and Ni(100) (ref:- 10) (bottom).

Other work function measurements of the coadsorption of oxygen and alkali metals have been made:- O/K-Pt(111) (ref:- 32), O/K-Fe(110) (ref:- 33); O/Cs-Cu(111) (ref:- 4). Unfortunately these workers restricted themselves to exposing usually only the saturated alkali monolayer to oxygen. Precise trends are therefore impossible to extract, but the more detailed work on O/Cs-Cu(111) (ref:- 4) is consistent with that for O/Cs-Cu(100) (ref:- 36).

Several models have been proposed in an attempt to reconcile the LEED, work functions and in some cases spectroscopic data. PARAGEORGOPOULOS et al seem to favour the double layer model. Here, the oxygen resides between the alkali metal layer and the substrate. In this configuration the oxygen would enhance the charge transfer from the alkali metal because it is even less electropositive than the substrate. PIRUG et al (ref:- 33) and GARFUNKEL & SOMORJAI (ref:- 9) prefer a single layer structure for O/K-Fe(110) and O/K-Pt(111) respectively. In this case the layer consists of an array of oxygen and potassium ions, and the work function is the spatial average of an array of opposing dipoles. Neither group, however, rules out the possibility of a double layer. In fact, PIRUG et al also studied the O/K-Pt(111) system (ref:- 32), and concluded that a double layer was formed but, due to the oxygen induced contraction of the outer potassium layer, free platinum surface was then available for further oxygen adsorption - a sort of mixed single-double layer model. Using ultraviolet photoelectron and X-ray photoelectron spectroscopy (UPS and XPS, see bibliography), they found no evidence for K_2O formation, contrary to the inferences made by GARFUNKEL & SOMORJAI, based on their thermal desorption measurement (ref:- 9).

At the present time, therefore, we see that there is insufficient experimental data to lead to an unambiguous understanding of the processes involved. Indeed, it is quite likely that each system will have to be assessed individually anyway. As for the theoretical aspects of the coadsorption problem, this is probably best summed up by DESPLAT & PAPAGEORGOPOULOS in ref. 27:-

..."Thus the prospect for a theoretical approach to the coadsorption of (in their case) Cs and oxygen with existing caesium adsorption formations appears bleak. Obviously new theoretical concepts are needed".

It is thus apparent that only the most general trends can be extracted from the existing data:

* Submonolayers or monolayers of alkali metal increase the rate of oxygen contamination by increasing the oxygen sticking coefficient.

* Oxygen can thermally stabilise the alkali metal, possibly resulting in unexpected second layer growth.

* Small amounts ($\theta_O < 0.1$) of coadsorbed oxygen or pre-existing oxide probably do not affect the work function or LEED patterns much.

* Large amounts ($0.1 < \theta_O < 1$) of chemisorbed oxygen exaggerate the features of the typical work function/alkali metal coverage curve, leading to a more pronounced minimum. Also, the LEED data may imply structures that cannot be explained in terms of the alkali metal alone.

* The existence of large amounts of surface oxide will wash out the minimum in the work function/alkali metal curve and may demonstrate its presence by a characteristic oxide LEED pattern which remains essentially unchanged on alkali metal adsorption.

* Oxygen may induce diffusion into the bulk (LAMBERT et al, refs:- 17,18,19).

2.7 Alkali metal coadsorption with: carbon monoxide; hydrogen; and nitrogen

In spite of the large amount of work currently being done on the coadsorption of carbon monoxide, hydrogen and nitrogen and alkali metals on transition metals due to the interest generated by the commercial need to promote catalytic performance, much of the information is in a form inappropriate for our purposes here. Only until comparatively recently have any studies on single crystal surfaces been performed, and the relevant aspects will now be commented on.

It appears that the presence of alkali metal on the surfaces of Pt, Fe and Ni generally reduces the sticking coefficient of CO (refs:- 40,41,42). For small amounts of alkali metal the initial sticking coefficient of CO is unchanged, but because CO itself does not absorb onto the alkalis at room temperature (ref:- 43) as the amount of alkali metal is increased, the CO sticking coefficient decreases (ref:- 41).

We have already noted that alkali metals tend to form ordered overlayers on metal substrates and there is evidence that this is also true for CO (see references in refs:- 44,45). In contrast no new ordered structures have been observed in coadsorption studies, and it is generally accepted that the CO molecule adsorbs with oxygen uppermost, in between the regions of alkali metal and not on top of them (e.g. ref:- 42). The work function data is similarly sparse: the adsorption of CO on potassium covered Fe(110) (ref:- 4) further reduces the work function, whereas the work function of potassium on Pt(111) (ref:- 40) is increased following CO adsorption. Apparently this behaviour depends on the degree to which CO dissociates (ref:- 40).

The adsorption of nitrogen on Fe(111) & Fe(100) is accelerate by the presence of submonolayer amounts of potassium, although the sticking coefficient still remains very small, $\approx 10^{-3}$ at R.T. (ref:- 46). Again, too much potassium is found to reduce the sticking coefficient by blocking part of the surface available for N_2 adsorption: nitrogen does not seem to adsorb on potassium at room temperature either (ref:- 43). Again it appears that the nitrogen is adsorbed in between the regions of potassium and this is not inconsistent with the structural information obtained from LEED :- on Fe(111) both K and N form a (3x3) structure which is also present on coadsorption; on Fe(100), even though potassium itself does not form an ordered structure, the c(2x2) that CO forms on clean Fe(100) is also present in coadsorption studies.

In contrast to nitrogen, hydrogen has a reduced sticking coefficient in the presence of potassium at all potassium coverages on Fe(100) and Fe(111) (ref:- 47) and on caesium on N(100) (ref:- 48). There is even a cautionary tale associated with the unsuspected coadsorption of hydrogen, in the study of caesium on W(100). Early work on caesium on W(100) (ref:- 49) led to the conclusion that Cs forms a highly ionic close packed layer, and then second layer growth occurs. This was based on the sequential development of first a c(2x2) pattern (associated with the first layer) and subsequently a p(2x2) pattern appeared as well which, with continued Cs deposition, compressed into an incommensurate hexagonal close packed "second layer". PAPAGEORGOPOULOS & CHEN (ref:- 48) and others later showed the c(2x2) structure to be due to hydrogen contamination, and that only one layer of caesium was deposited after all!

PAPAGEORGOPOULOS & CHEN also found that when hydrogen was coadsorbed with caesium on W(100) the work function curve changed in the same way that the presence of oxygen changed it but that the trends were much more noticeable. Hydrogen coadsorption led to a much deeper work function minimum and a much larger work function value at saturation Cs coverage. This result is surprising since oxygen is more electronegative than hydrogen; one would expect that the trends would be less pronounced in the case of hydrogen coadsorption. Unfortunately, no satisfactory explanation has been found for this behaviour.

Hence it seems that even less can be said about how the presence of CO, H_2 and N_2 could affect the properties of alkali metal overlayers:

* Small, submonolayer amounts of alkali metal can either increase or decrease the sticking coefficients of CO, H_2 and N_2. The sticking coefficient of these gases on alkali metal monolayers is, however, reduced.
* Coverage calibrations as assessed by LEED may be wrong if unsuspected coadsorbates also form ordered overlayers.

2.8 Oxygen on Aluminium

The initial stages of the adsorption of oxygen on aluminium have been challenging theoreticians and experimentalists alike for many years. This is partly due to the theoretical appeal of an "apparently simple" chemisorption system and partly because in practice the processes involved appear far from simple and are still poorly understood. (A discussion of the theoretical aspects of the problem, however, is beyond the scope of this review: further information may be found in ref:- 50 and references 19-26 therein).

Early experimental studies of the oxidation of polycrystalline aluminium were found to be misleading with the discovery that the oxidation mechanism was face dependent (ref:- 51). Since most workers agree about the initial stages of oxygen adsorption on

Al(100) and Al(110) surfaces (refs:- 51,52,53; however, see ref:- 54) and as only the (111) plane was used in this study no more will be said about these faces.

Inconsistencies between the results obtained by different workers using the same technique (refs:- 51,53,54,55) has cast some doubt on the equivalence of their sample preparation procedures and has led some workers (refs:- 56,57) into growing their aluminium (111) surfaces in situ by vapour deposition and subsequent annealing. Gradually, it has also become apparent that the properties of the oxygenated (111) surface depend on the partial pressure of the oxygen used during the exposures (refs:- 53,57,58).

It appears that the oxidation of the aluminium (111) surface is roughly a two step process, although SORIA et al have further resolved it into a four step process (ref:- 57). During the first stage, oxygen is chemisorbed up to a coverage of about one monolayer. XPS and synchrotron radiation studies (refs:- 55,59) of the binding energies of the O 1s and Al 2p core levels show shifts characteristic of chemisorbed, although not oxide-like, oxygen up to this coverage. Auger electron spectroscopy (see bibliography) also shows the absence of oxide like features at this coverage (ref:- 57). Heating the overlayers at these coverages, however, results in the appearance of bulk aluminium oxide-like spectral features (refs:- 55,59). FLODSTRÖM/MARTINSON et al (refs:- 52,59) inferred that the monolayer of oxygen formed a commensurate (1x1) surface structure because the symmetry of the LEED pattern did not alter, and there were drastic changes in the energy dependence of the intensities of the diffracted beams. This model is also consistent with angle resolved UPS measurements (ref:- 60).

The evidence for an initial chemisorbed monolayer must be weighed against conflicting information coming from work function data (refs:- 51,53,54,55). The work function oxygen exposure curves, although all subtly different, show a reduction in the work function during the formation of the oxygen monolayer. A reduction in work function on oxygenation is usually evidence of oxide formation and this contrasts with the results from the other techniques. One possible explanation is an incorporation process, i.e. chemisorption, but below or in the aluminium surface plane. In order to find the position of the oxygen layer full LEED intensity analyses have been performed (refs:- 56,61,62). These calculations, however, place the oxygen atoms in 3 fold hollow sites outside the aluminium surface of monolayer coverage, by 1.54Å (ref:- 62), 1.33 ± 0.05Å (ref:- 61) and 1.46 ± 0.05Å (ref:- 56). Not only is the agreement between them poor, but they are inconsistent with the work function data and recent (EXAFS) measurements (ref:- 63) imply that they overestimate the aluminium-oxygen distance considerably.

YU et al (ref:- 56), however, performed their LEED analysis as a function of oxygen coverage and came to the conclusion that up to 1/3 of a monolayer the oxygen atoms seem to prefer an in-plane configuration probably located in defect sites with some oxygen atoms below the surface, but without forming on ordered underlayer. Subsequently, when all such sites are full, an ordered overlayer is formed on top of the surface. This model is certainly consistent with both the work function data and the 'chemisorbed' data.

Subsequently SORIA et al (ref:- 57) explained the differences between the various LEED analyses by showing that the overlayer-substrate separation is coverage dependent and so will depend on how the various workers calibrate their oxygen coverage.

Above ≈ 1 monolayer coverage all workers agree that there is a progressive oxidation of the aluminium surface. This was shown by the XPS, AES and synchrotron studies mentioned earlier.

2.9 Carbon monoxide, water, hydrogen and nitrogen on aluminium

There appears to be much controversy surrounding the adsorption of CO on aluminium. Some workers (ref:- 64) have not seen room temperature adsorption of CO on Al (111), (100), (110) even up to exposures of 54K-langmuirs. Others (ref:- 65) have seen slow or fast adsorption kinetics depending on the sample preparation, and plausibly suggest that the initial adsorption at least may be defect sensitive.

Even amongst workers who have all seen room temperature adsorption there is disagreement about the mechanism. Hence KHONDE et al (refs:- 44,65) observe the sequential appearance of first aluminium oxide spectral features, and then aluminium carbide spectral features. KATAYAMA et al (ref:- 66), working with polycrystalline films, see the reverse happening. Neither can the differences be necessarily put down to the different types of sample as BARGERON & NALL (ref:- 64) did not see CO adsorption on either single crystal or polycrystalline samples!

Water adsorbs on aluminium at room temperature with an initial sticking coefficient of ≈ 0.05 (ref:- 67). For the aluminium (111) surface at least, no new LEED patterns are seen. There is just a reduction in the intensity of the (111) spots (ref:- 68). The adsorption mechanism is thought to involve the dissociation of the H_2O molecule with the subsequent growth of aluminium oxide islands (refs:- 67,69,70). The hydrogen at this stage appears to be given off in the form of gaseous H_2 (ref:- 68). The oxide islands themselves, however, once produced, act as more efficient sites for water adsorption and hydration and reduction of the oxide patches occur (refs:-

67,69). These hydrated/hydroxide patches are responsible for a large subsequent fall in the work function by ≈1.4 eV (ref:- 71).

This behaviour is entirely consistent with the fact that hydrogen does not adsorb either molecularly or dissociately on clean Al(111) surfaces at room temperature (refs:- 43,72,73) and with the known strength of the Al-O bond. (Nitrogen also appears not to adsorb on the alkali metals or aluminium under normal conditions (ref:- 43)).

2.10 Summary

In the first part of this chapter we have looked in more detail at the experimental evidence for alkali metal chemisorption. We have seen that there are well defined trends which are reproduced qualitatively by the theory, but that the simple and supposedly ideal Na/Al system behaves anomalously.

In the second part of this chapter attempts were made to try and assess how contamination would affect the results. This was required because the results of PORTEUS and those subsequently to be discussed here may have been influenced by contaminants.

Hydrogen and nitrogen would appear the least important, even though hydrogen is not directly detectable with AES, which makes it difficult to assess its effects.

We are left with O_2, CO and H_2O. The latter two gases both appear to decompose on clean aluminium surfaces, and it is likely that it is the oxygen species so produced that dominates. In later chapters we shall have need to refer to some of the information presented in this one.

REFERENCES

1. S. ANDERSON and U. JOSTELL. Surface Sci. 46 (1974) p.625
2. S. THOMAS and T.W. HAAS. J. Vac. Sci. Technol. Vol.9 No. 2 p.840 (1972)
3. A.G. FEDORUS and A.G. NAUMOVETS. Surface Sci. 21 (1970) p.426
4. S.A. LINDGREN and L. WALLDEN. Phys. Rev. B. Vol. 22 No.12 p.5967 (1980)
5. R.L. GERLACH and T.N. RHODIN. Surface Sci. 17 (1969) p.32
6. V.K. MEDVEDEV, A.G. NAUMOVETS and A.G. FEDORUS. Sov. Phys.- Solid State Vol. 12 No.2 p.301 (1970)
7. S.B. LEE, M. WEISS and G. ERTL. Surface Sci. 108 (1981) p.357
8. G. BRODEN and H.P. BONZEL. Surface Sci. 84 (1979) p.106
9. E.L. GARFUNKEL and G.A. SOMORJAI. Surface Sci. 115 (1982) p.441
10. C.A. PAPAGEORGOPOULOS and J.M. CHEN. Surface Sci. 52 (1975) p.40
11. C.A. PAPAGEORGOPOULOS and J.M. CHEN. Surface Sci. 39 (1973) p.283
12. E.A. WOOD. J. Appl. Phys. Vol. 35 No.4 p.1306 (1966)
13. S. ANDERSSON and U. JOSTELL. Solid State Commun. 11 p.829 (1972)
14. R.L. GERLACH and T.N. RHODIN. Surface Sci. 19 (1970) p.403
15. VAPOUR PRESSURE CHART: Radio Corporation of America. PRINCETON N.J.
16. CHEN-SHOW WANG. J. Appl. Phys. Vol.48 No.4 p.1477 (1977)
17. R.A. MARBROW and R.M. LAMBERT. Surface Sci. 61 (1976) p.329
18. M. KITSON and R.M. LAMBERT. Surface Sci. 109 (1981) p.60
19. P.J. GODDARD and R.M. LAMBERT. Surface Sci. 79 (1979) p.93
20. See for example: 'Double layer' in Fundamentals of Electromagnetic Field Theory, Zaky and Hawley. HARRAP LONDON

21. A.J. TOPPING. Proc. Roy. Soc. (LONDON) A 114 (1927) p.67

22. A.G. NAUMOVETS and A.G. FEDORUS. JETP LETT. 10 p.6 (1969)

23. V.K. MEDVEDEV and T.P. SMEREKA. Sov. Phys. Solid State Vol.16 No.6 p.1046 (1974)

24. M.S. GUPALO, V.K. MEDVEDEV, B.M. PALYUKH and T.P. SMEREKA Sov. Phys. Solid State Vol.23 No.7 p.1211 (1981)

25. M.S. GUPALO. Sov. Phys. Solid State Vol. 22 No.8 p.1345 (1980)

26. V.K. MEDVEDEV, A.G. NAUMOVETS and T.P. SMEREKA. Surface Sci. 34 (1973) p.368

27. J-L. DESPLAT and C.A. PAPAGEORGOPOULOS. Surface Sci. 92 (1980) p.97

28. J.O. PORTEUS. Surface Sci. 41 (1974) p.515

29. B.A. HUTCHINS, T.N. RHODIN and J.E. DEMUTH. Surface Sci. 54 (1976) p.419

30. K.D. GRONWALD and M. HENZLER. Surface Sci. 117 (1982) p.180

31. M. VAN HOVE, S.Y. TONG and N. STONER. Surface Sci. 54 (1976) p.259

32. G. PIRUG, H.P. BONZEL and G. BRODEN. Surface Sci. 122 (1982) p.1

33. G. PIRUG, G. BRODEN and H.P. BONZEL. Surface Sci. 94 (1980) p.323

34. C.A. PAPAGEORGOPOULOS and J.M. CHEN. Surface Sci. 52 (1975) p.53

35. C.A. PAPAGEORGOPOULOS and J.M. CHEN. Surface Sci. 39 (1973) p.313

36. C.A. PAPAGEORGOPOULOS. Solid State Commun. Vol.27 p.1069 (1978)

37. E. BAUER and T. ENGEL. Surface Sci. 71 (1978) p.695

38. P. HOFMANN, R. UNWIN, W. WYROBISCH and A.M. BRADSHAW. Surface Sci. 72 (1978) p.635

39. C.A. PAPAGEORGOPOULOS and J.M. CHEN. J. Vac. Sci. Technol. Vol.9 p.570 (1972)

40. J.E. CROWELL, E.L. GARFUNKEL and G.A. SOMORJAI. Surface Sci. 121 (1982) p.303

41. M.P. KISKINOVIA. Surface Sci. 111 (1981) p.584

42. G. BRODEN, G. GAFNER and H.P. BONZEL. Surface Sci. 84 (1979) p.295

43. B.M.W. TRAPNELL. Proc. Roy. Soc. (LON) A 218 (1953) p.566

44. K. KHONDE, J. DARVILLE and J.M. GILLES. Vacuum 31 (1981) p.499

45. J. BENZIGER and R.J. MADIX. Surface Sci. 44 (1980) p.119

46. G. ERTL, S.B. LEE and M. WEISS. Surface Sci. 114 (1982) p.527

47. G. ERTL, S.B. LEE and M. WEISS. Surface Sci. 111 (1981) L711

48. C.A. PAPAGEORGOPOULOS and J.M. CHEN. Surface Sci. 39 (1973) p.283

49. A.U. MACRAE, K. MÜLLER, J.J. LANDER and J. MORRISON. Surface Sci. 15 (1969) p.483

50. I.P. BATRA and O. BISI. Surface Sci. 123 (1982) p.283

51. P.O. GARTLAND. Surface Sci. 62 (1977) p.183

52. C.W.B. MARTINSON and S.A. FLÖDSTRÖM. Surface Sci. 80 (1979) p.306

53. P. HOFMANN, W. WYROBISCH and A.M. BRADSHAW. Surface Sci. 80 (1979) p.344

54. R. MICHEL, J. GASTALDI, C. ALLASIA, C. JOURDAN and J. DERRIEN. Surface Sci. 95 (1980) p.309

55. A.M. BRADSHAW, P. HOFMANN and W. WYROBISCH. Surface Sci. 68 (1977) p.269

56. H.L. YU, M.C. MUNOZ and F. SORIA. Surface Sci. 94 (1980) L184

57. F. SORIA, V. MARTINEZ, M.C. MUNOZ and J.L. SACEDON. Phys. Rev. B<u>24</u> No.12 p.6926 (1981)

58. R.Z. BACHRACH, G.V. HANSSON and R.S. BAUER. Surface Sci. <u>109</u> (1981) L560

59. S.A. FLODSTRÖM, C.W.B. MARTINSSON, R.Z. BACHRACH, S.B.M. HAGSTROM and R.S. BAUER. Phys. Rev. Lett. Vol.40 No.13 p.907 (1978)

60. P. HOFMANN, C.V. MUSCHWITZ, K. HORN, M. JACOBI, A.M. BRADSHAW and K. KAMBE. Surface Sci. <u>89</u> (1979) p.327

61. C.W.B. MARTINSON, S.A. FLODSTRÖM, J. RUNDGREN and P. WESTRIN. Surface Sci. <u>89</u> (1979) p.102

62. R. PAYLING and J.A. RAMSAY. J. Phys. C<u>13</u> (1980) p.505

63. D. NORMAN, S. BRENNAN, R. JAEGER and J. STÖHR. Surface Sci. <u>105</u> (1981) L297

64. C.B. BARGERON and B.H. NALL. Surface Sci. <u>119</u> (1982) L319

65. K. KHONDE, J. DARVILLE, J.M. GILLES. Surface Sci. 126 (1983) p.414

66. Y. KATAYAMA, K.L.I. KOBAYASHI and Y. SHIRAKI. Surface Sci. <u>86</u> (1979) p.549

67. W.H. KRUEGER and S.R. POLLACK. Surface Sci. <u>30</u> (1972) p.280

68. F.P. NETZER and T.E. MADEY. Surface Sci. <u>127</u> (1983) L102

69. J.C. FUGGLE, L.M. WATSON and D.J. FABIAN. Surface Sci. <u>49</u> (1975) p.61

70. W. EBERHARDT and C. KUNZ. Surface Sci. <u>75</u> (1978) p.709

71. T. FORT and R.I. WEISS. Surface Sci. <u>32</u> (1972) p.543

72. F. PELLERIN, C. LE GRESSUS and D. MASSIGNON. Surface Sci. <u>111</u> (1981) L705

73. S.A. FLODSTRÖM, L-G. PETERSSON and S.B.M. HAGSTRÖM.
J. Vac. Sci. Technol. Vol.13 No.1 p.280 (1976)

BIBLIOGRAPHY

Low Energy Electron Diffraction:

E. BAUER: "Low Energy Electron Diffraction (LEED and Auger Methods)" in Topics in Applied Physics Volume 4, ed. by R. GOMER (SPRINGER-VERLAG 1977)

J.B. PENDRY: "Low Energy Electron Diffraction" (ACADEMIC PRESS LONDON 1974)

Thermal Absorption Spectroscopy

D. MENZEL: "Desorption Phenomena" in Topics in Applied Physics Volume 4, ed. by R. GOMER (SPRINGER-VERLAG 1977)

Auger Electron Spectroscopy

D. CHATTARJI: "The Theory of Auger Transitions", Chapter 8 (ACADEMIC PRESS LONDON 1976)

X-ray Photoelectron Spectroscopy and Ultraviolet Photoelectron Spectroscopy

T.A. CARLSON: "Photoelectron and Auger Spectroscopy" (PLENUM PRESS NEW YORK 1975).

CHAPTER 3

THE EXPERIMENTAL ARRANGEMENT

Introduction

In this chapter the preparation and analysis techniques used in this study are described. For the sake of brevity an in-depth description of some of the techniques, e.g. LEED and AES, has been omitted. More information on these standard surface science techniques can be found in the bibliography in Chapter 2.

3.1 Sample preparation and mounting

The sample used throughout this study took the form of a small disc ≈ 3mm thick and ≈ 12mm in diameter, which was spark machined from a 99.99% pure single crystal of aluminium (METALS RESEARCH, CAMBRIDGE, UK). The LAUE X-ray back diffraction method (ref:- 1) was used to orient the large stock crystal and to ensure that the sample was cut and spark-planed so that its flat sides were parallel to within ±1° of the (111) plane. The sample was then held in a quick setting plastic and mechanically polished with first fine carborundum paper and then with successively finer grades of diamond paste ($6\mu m \longrightarrow 3\mu m \longrightarrow 1\mu m \longrightarrow 0.25\mu m$). When a shiny, although slightly "milky", surface had been obtained, the mounting plastic was dissolved away in chloroform and the crystal was ultrasonically cleaned in chloroform, acetone and then ethanol.

In order to smooth out the small scratches left by the mechanical polishing, the crystal was electropolished in a solution of 20% perchloric acid and 80% absolute ethanol. The method used was that described by TEGART (ref:- 2), and details are shown in figure 3.1.

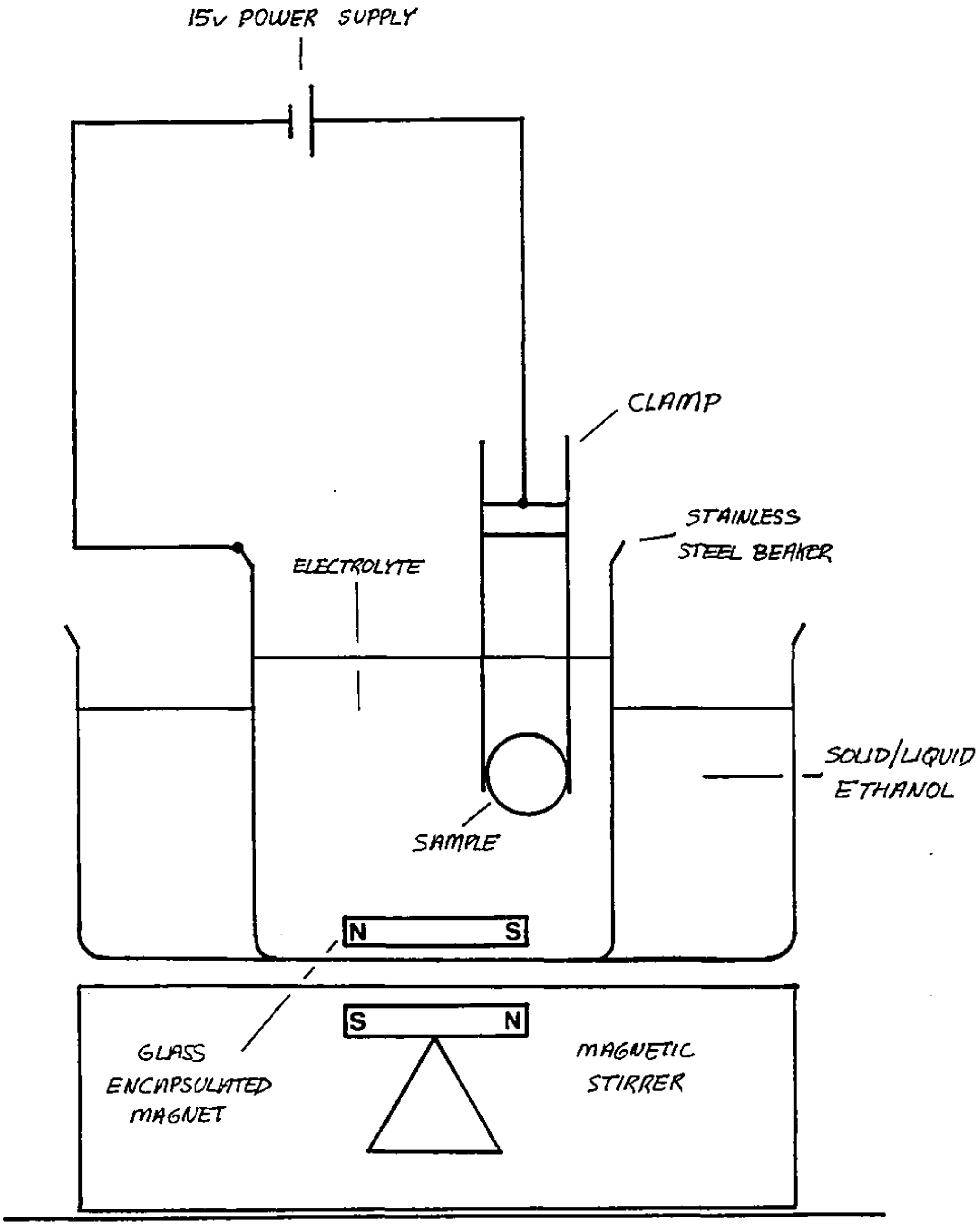

Figure 3.1: Experimental set-up used for electropolishing the aluminium sample.

The sample was held in the electrolyte between the jaws of a small metal clamp which was also connected to the positive terminal of a power supply unit. To protect the sides and the back of the sample and the clamp during the electropolishing procedure, these surfaces had been previously covered with a (chloroform soluble) varnish. The electrolyte was contained in a stainless steel beaker which was connected to the negative terminal of the power supply unit, and the solution was kept mobile by a magnetic stirrer.

Because the electrolyte is potentially explosive, its temperature must be kept as low as possible, i.e. $\approx {}^{-}30°C$. This was effected by placing the stainless steel beaker in a bath of ethanol which was maintained in a solid/liquid state by cooling with liquid nitrogen.

The sample was polished by applying a voltage of $\approx$ 15 volts between it and the beaker for a period of about 15 minutes. This produced a mirror-bright surface with only a low density of etch pits. After the electropolishing, the sample and its clamp were rinsed in ethanol, the protective varnish was removed with chloroform, and the sample was given another ultrasonic cleaning as before.

The crystal was then laser welded onto a thin aluminium backing plate (99.99% pure Al : GOODFELLOW METALS, CAMBRIDGE, UK), which was subsequently attached to a Vacuum Generators' (V.G. SCIENTIFIC, EAST GRINSTEAD, UK) HPT manipulator (see figure 3.2). The manipulator possessed full translational and rotational degrees of freedom as well as a facility for heating and cooling the sample. For the latter, a thick copper braid was used to place the sample and its backing plate in thermal contact with a copper block which could be cooled by a supply of liquid nitrogen. It was found that sample temperatures as

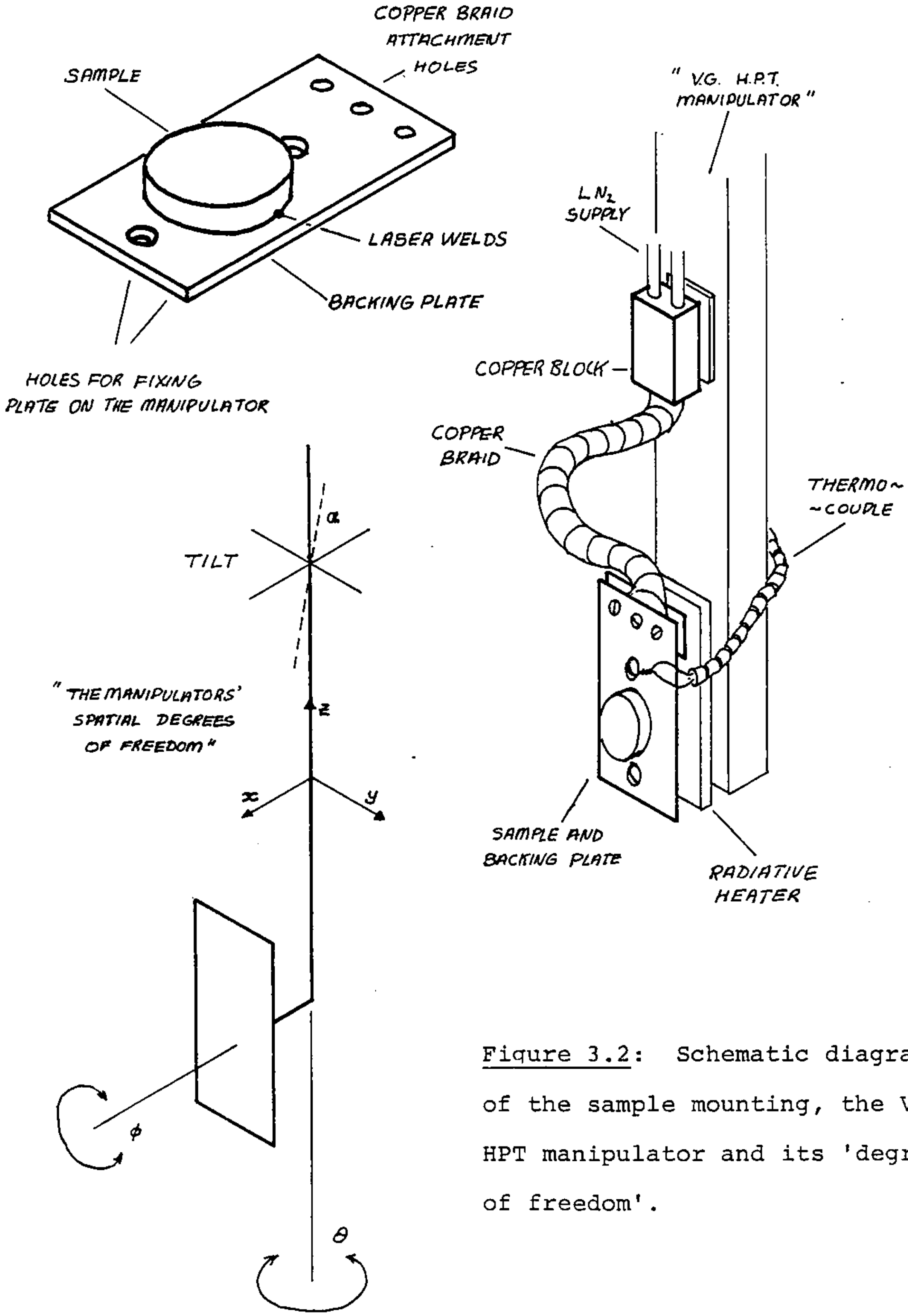

Figure 3.2: Schematic diagram of the sample mounting, the V.G. HPT manipulator and its 'degrees of freedom'.

low as ~ -200°C could be attained in 30 minutes. Most of the experiments, however, were performed at room temperature or, more precisely, as the sample cooled down from its annealing treatment (see later). No measurements or alkali metal depositions were made until the crystal temperature had fallen to below 100°C. The sample was heated radiatively by a resistance heater that was situated behind the backing plate.

The temperature of the sample was measured with a chromel/alumel thermocouple. Several methods of fixing the thermocouple to the sides of the sample and backing plate were tried. It was found that spot welding was useless and that laser welding produced a bond that would subsequently fail during an experiment! In spite of this, because the thermojunction could be laser welded very close to the sample, good estimates of the true sample temperature could be obtained while the weld lasted.

The most robust form of thermocouple attachment used was to clamp the thermojunction under one of the heads of the bolts that fixed the backing plate to the manipulator (see figure 3.2). This meant, however, that the thermojunction was located much further from the sample.

The thermocouple also provided the only means by which the sample could be electrically earthed since the backing plate was electrically isolated from the manipulator and the rest of the system. This earth connection was made outside the vacuum system (via UHV compatible isolated feed throughs), so that the sample potential could also be set to other values as was required for the work function measurements to be described later.

3.2 The vacuum system

All of the experiments were performed in a liquid nitrogen trapped, diffusion pumped stainless steel vacuum system shown schematically in figure 3.3. After a 12 hour bakeout at 200°C the system would routinely attain a base pressure of 1×10^{-10} Torr, as measured by an outgassed BAYARD/ALPERT type ionisation gauge. Internal μ metal shielding provided adequate protection against external magnetic fields, as was demonstrated by a previous user of this machine (ref:- 3).

The system was equipped with the following items: a V.G. mod 668 3 grid LEED display optics with an integral L.E.G. 21 electron gun; a V.G. A.G.S2 high energy argon ion gun which was used for sputter cleaning; a V.G. ANAVAC mass quadrupole which was used for residual gas analysis during leak testing and filament outgassing; a V.G. L.E.G. 3 side incidence electron gun; an alkali metal evaporator; two shutters, one to regulate the flux of alkali metal, and the second to protect the LEED optics during alkali metal deposition and sputter cleaning; and finally, a viewport.

The 3 grid LEED optics were also used as a retarding field analyser for A.E.S. and electron energy loss spectroscopy, EELS, in the standard way (refs:- 4,5). In addition to the usual programmable voltage ramp, a 2 frequency oscillator and the phase sensitive detection circuitry, a NICOLET 1170 signal averager (NICOLET INC. WARWICK, U.K.) was used to increase the signal to noise ratio (see section 3.6). A schematic of the analyser configuration and detection circuitry is shown in figure 3.4.

3.3 In situ cleaning

Once mounted within the vacuum system, the polished

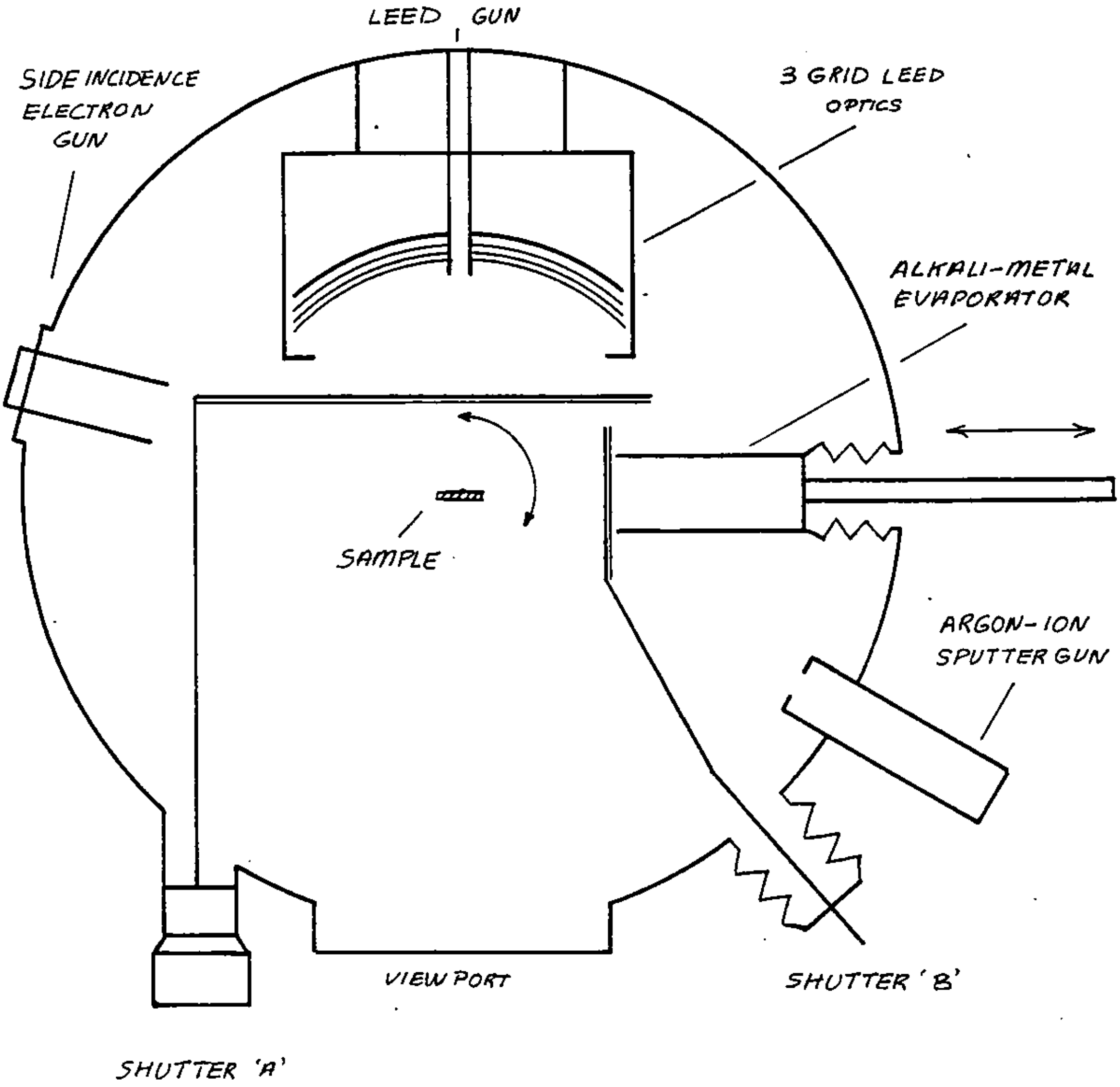

Figure 3.3: Schematic diagram of the UHV chamber used in this study.

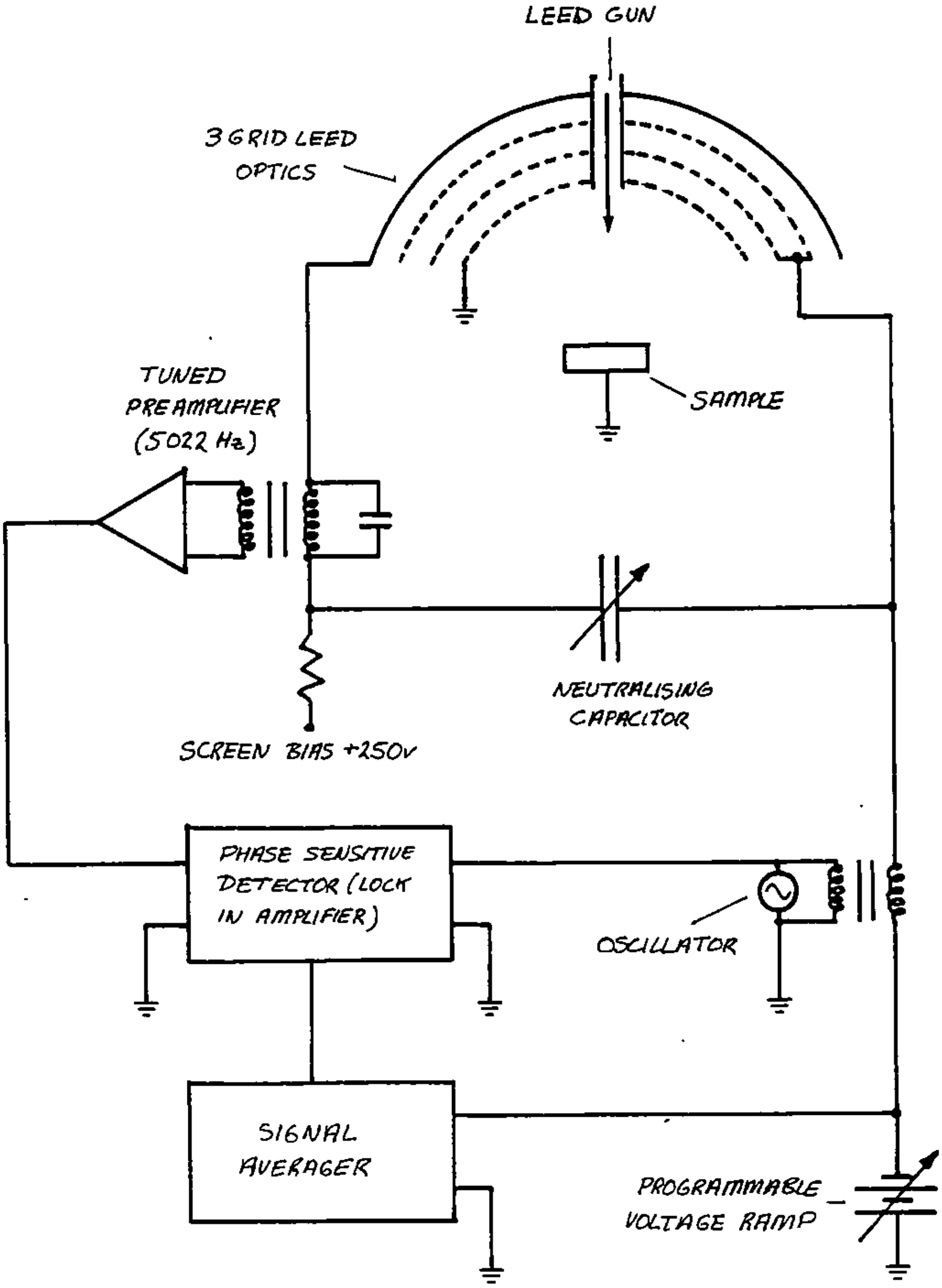

Figure 3.4: Schematic diagram of analyser configuration and circuitry used for obtaining the $\frac{dN}{dE}(E)$ (AUGER) and N(E) (energy-loss) spectra. Since the preamp was tuned for 5022 Hz, for the $\frac{dN}{dE}$ (E) spectra, a modulating frequency of 2511 Hz was used, and for the N(E) spectra a modulating frequency of 5022 Hz was used.

aluminium (111) surface was cleaned by repeated cycles of argon ion bombardment (with a beam energy of 4KeV and a current density at the sample of $5\mu Acm^{-2}$ for periods of 15 minutes duration) and annealing (at temperatures around 400°C for periods of an hour duration).

Cleanliness was assessed using normal incidence A.E.S. in the $\frac{dN(E)}{dE}$ mode with a primary beam energy of 1KeV, a beam current of 2µ Amps and grid modulation of 5 volts peak to peak. The surface was considered clean when the Auger peaks due to oxygen and carbon - the principal contaminants - could not be resolved from the background noise and when no further changes in the aluminium 68eV $L_{2,3}$.VV Auger feature occurred between successive cleaning cycles (see section 3.6). Initially this required about 12 cycles, although subsequently only one was required to clean the surface prior to each experiment.

3.4 Alkali metal deposition

Potassium (or caesium) could be adsorbed onto the aluminium crystal by passing an electric current through a commercial high purity alkali metal "getter" (SAES GETTERS, CROYDON, UK) mounted approximately 10cm from the sample. Each getter contains an alkali metal chromate which is reduced by heating with a non-evaporable zirconium-aluminium alloy St 101 ^{R}. This alloy is also responsible for the subsequent high purity of the evolved alkali metal since it sorbs at source any gas produced in the reaction. Details of a getter and the evaporator construction are shown in figure 3.5: in addition to the current supply to the getter, a thermocouple was spot welded to the casing, allowing accurate temperature measurements to be made. The entire evaporator was mounted

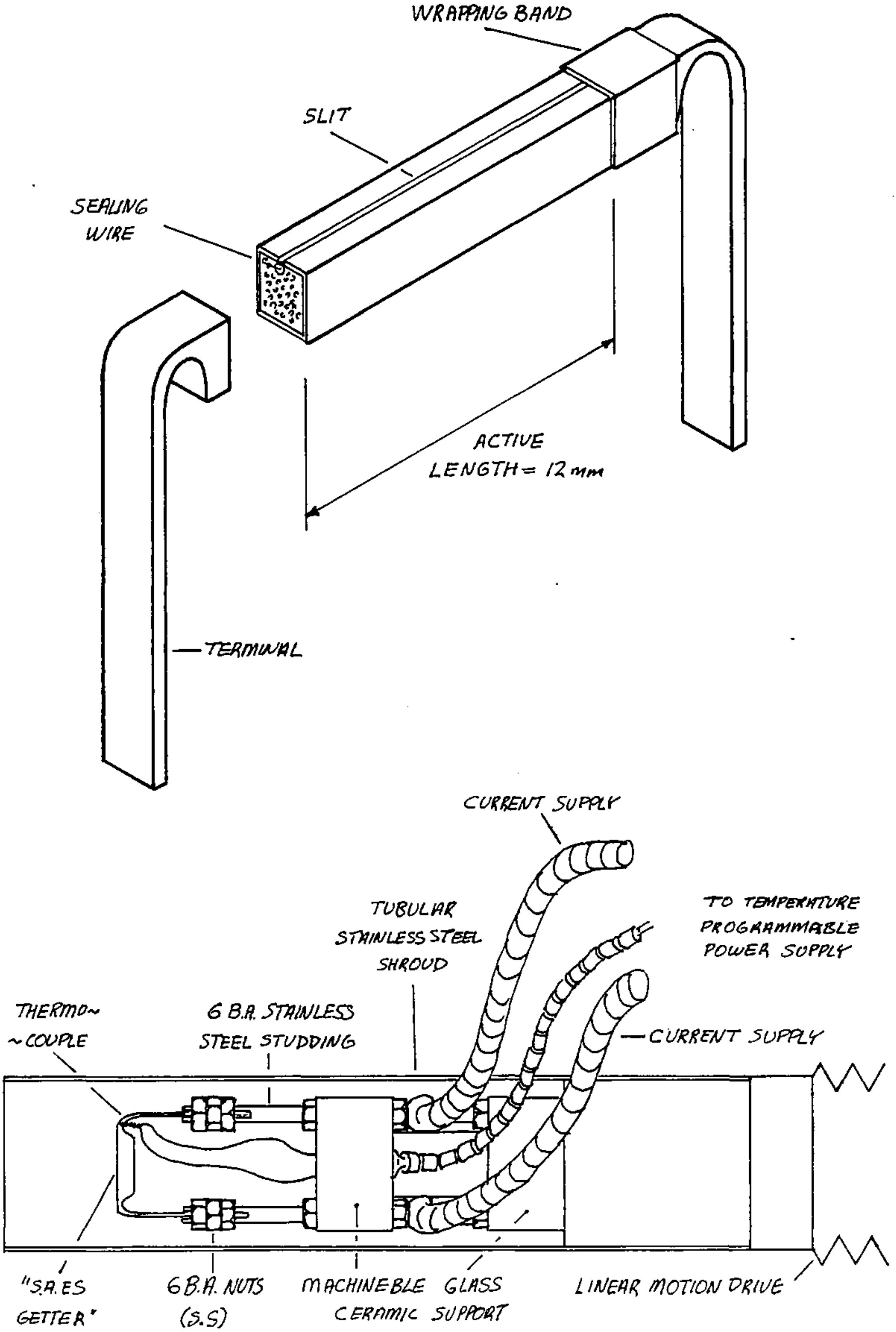

Figure 3.5: Diagram of S.A.E.S. GETTER (exploded view, top) and evaporator construction (bottom).

on a precision linear drive mechanism which allowed it to be retracted during the sputter cleaning procedure and repositioned accurately afterwards (see figure 3.3). Each getter had to be thoroughly outgassed at a temperature not exceeding 500°C before use. During this outgassing procedure quantities of CH_4, H_2O, N_2, CO, CO_2 and H_2were evolved. Once properly outgassed and "activated" (temperature >500°C), however, the ambient pressure in the system did not exceed 3×10^{-10} Torr during the experiments for getters of either type (i.e. K or Cs).

These sources of potassium and caesium were chosen because of their apparent freedom from contaminants (ref:- 6 and section 3.6) and because they were easy to use and replace when exhausted. Other sources of alkali metal could also have been used. For example, zeolite sources (ref:- 7) or pure alkali metal contained in evacuated glass ampoules which could then be broken and heated in the vacuum system (e.g. ref:- 6). The zeolite class of evaporators produce a flux of alkali metal ions and so have the advantage that coverage can be checked or assessed using current measurements and the assumption of unity sticking coefficients. Unfortunately, they also appear to yield relatively large quantities of oxygen (e.g. ref:- 6), and so they were not used in this study. The alkali metal ampoule method of deposition can in principle produce high fluxes of high purity alkali metal. They are apparently less convenient to use than the "getter method".

In order to deposit potassium (or caesium) onto the aluminium crystal shutter 'A' in figure 3.3 is first raised to protect the LEED optics from contamination. The sample is then rotated about the vertical axis to face the evaporator and exposure times are controlled by lowering and raising a second shutter, 'B'. During the experiments the getter was maintained at a constant temperature (e.g. 575 ± 2°C) by the use of a direct current temperature programmable power supply (ref:- 8). For a given getter it was found that extremely reproducible results could be obtained, although there were differences in apparent yield between different getters - even of the same alkali.

It was also found that if a getter was operated at much higher temperatures (>650°C) in order to produce higher alkali metal fluxes, then not only was reproducibility lost (due to a progressive thermal distortion of its casing), but that it was also exhausted too quickly. The relatively small alkali metal content of the getters was their main disadvantage.

3.5 The measurements

Normal incidence LEED and AES were used to monitor surface crystallography and alkali metal up-take as a function of exposure time. Work function change measurements were made using the retarding field method (ref:- 9) with an incident electron beam energy of $\approx$60eV to allow the simultaneous observation of the LEED patterns. These measurements were cross checked with measurements of the shifts in the secondary electron cut-off in the bandscattered electron energy distribution (ref:- 10). In this second method it was found necessary to bias the sample with -9 volts w.r.t. earth to separate the true secondaries from those produced at the electron gun collimator and grids of the LEED optics (ref:- 11). In fact, it was the shifts in the $\frac{dN(E)}{dE}$ peak corresponding to the rapidly falling secondary electron distribution that were measured. Both methods gave identical results and are described in detail in section 3.7.

Electron energy loss spectra were recorded in both the N(E) and the $\frac{dN(E)}{dE}$ mode, depending on the circumstance (see later) for various primary beam energies and a beam current of 2μ Amps. In the N(E) mode the modulation at the grids was chosen to be 0.1v peak to peak - a compromise between signal strength and the desire to avoid dynamical broadening (ref:- 12) at large modulating voltages. In the $\frac{dN(E)}{dE}$ mode, however, in order to obtain sufficient signal, a modulation of 1v peak to peak was found to be necessary.

Each of the techniques mentioned above, AES, EELS, LEED and work function measurements, were performed at normal incidence using the standard LEED gain to assure that they all sampled the same area. Unfortunately, experimental constraints prevented the use of AES simultaneously with work function and EELS measurements. Since a priori there is no guarantee that constant getter characteristics will be maintained from one experiment to another, some quick and easy method was required to monitor the alkali metal up-take and/ or the getter characteristics for each experiment. The solution to this problem was found by measuring the total sample current to earth at fixed beam energy ($\approx$ 260 eV) and beam current (2μ Amps) as a function of alkali metal exposure time in a manner described by RHEAD et al (refs :- 13,14).

Figure 3.6(a) shows how the measurements were made, and figure 3.6(b) shows a graph of the crystal current (icc) to earth at constant electron gun emission current (2μ Amps) as a <u>function</u> of primary beam energy for the aluminium crystal used in this study. Also shown in figure 3.6(b) is the effect that the adsorption of a small amount of alkali metal (in this case potassium) has on the crystal current. The main

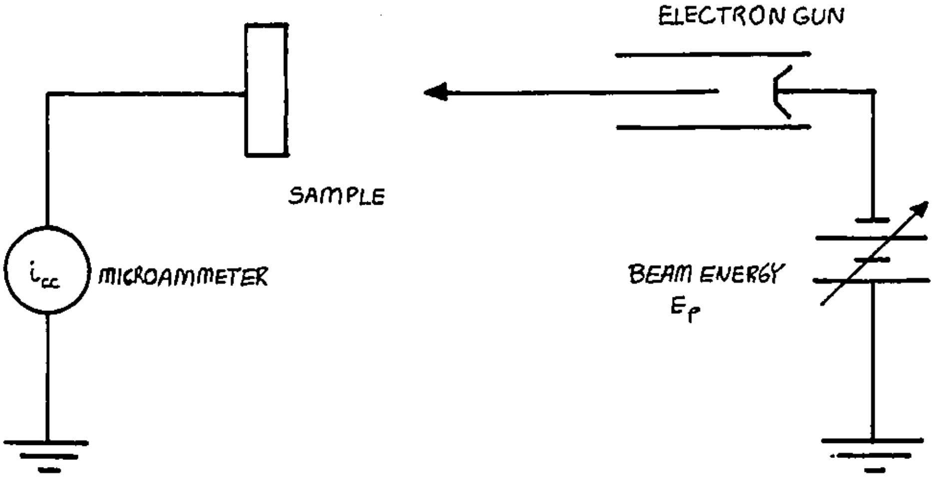

Figure 3.6(a): Schematic diagram of arrangement used for measuring crystal current.

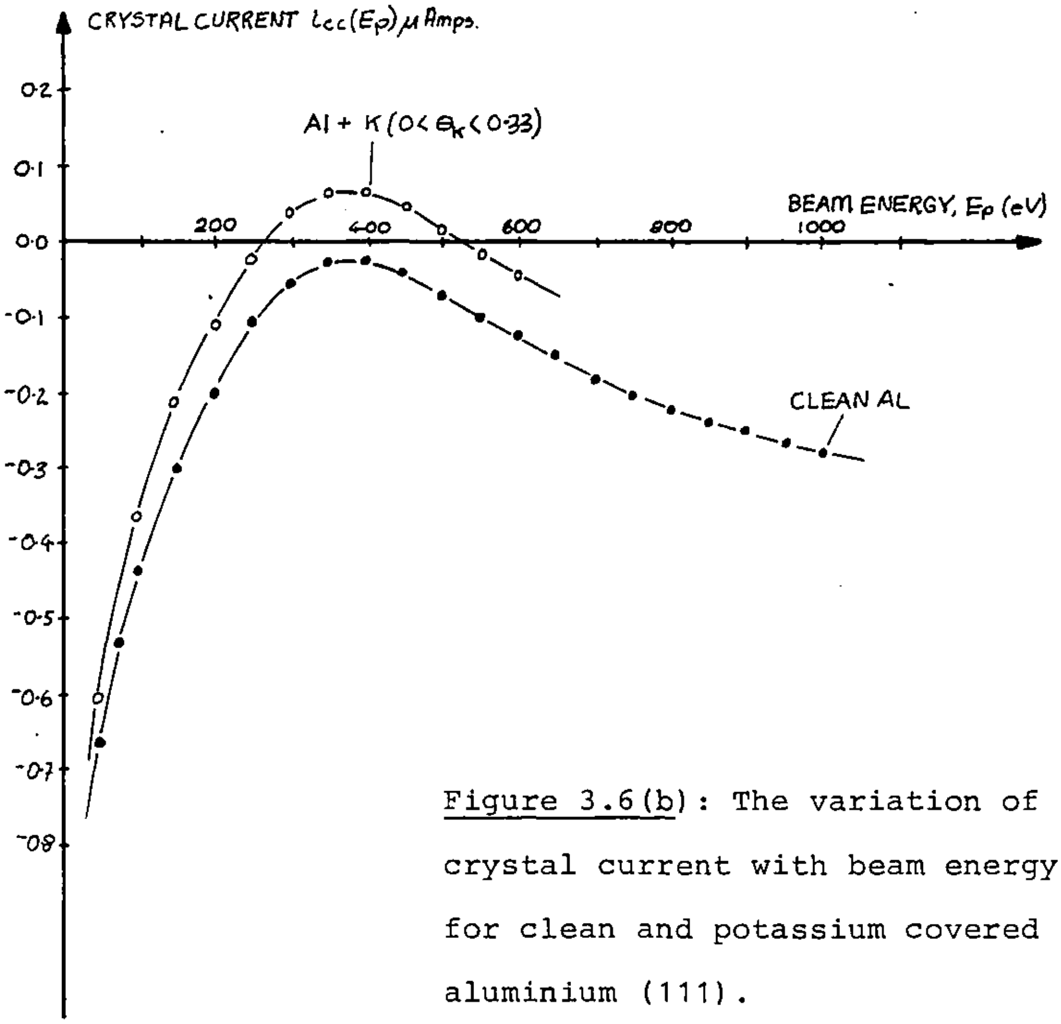

Figure 3.6(b): The variation of crystal current with beam energy for clean and potassium covered aluminium (111).

effect of alkali metal adsorption appears to be a vertical displacement from the "clean curve". It was found that this shift, i.e. the change in the crystal current to earth at constant beam energy, changed in a reproducible way as a function of alkali metal exposure time. Such current measurements were quick and easy to make, and the technique was compatible with all the other techniques. Indeed, once the crystal current measurements were calibrated against AES and LEED, they could be used to define absolute coverage (see Chapters 4 and 5).

3.6 The assessment of contamination

During the course of the experiments much trouble was caused by "noise" appearing on the various Auger and energy loss spectra. Fortunately, signal averaging helped to alleviate this problem. Signal averaging works by adding noisy, though otherwise identical, spectra. The true signal wave forms add with each successive 'scan', but the noise, if random, will tend to average out to a constant level which reflects its mean value. If we sum 'n' versions of the noisy spectra the true signal is increased by a factor of 'n'. The standard deviation of the noise, however, only increases by a factor of $\sqrt{n}$ (ref:- 15). Hence the ratio of the signal amplitude to the noise standard deviation improves by a factor of $\sqrt{n}$.

Signal averaging was used to a greater or lesser extent on all of the spectra presented in this thesis and is especially useful for the detection of small quantities of materials such as alkali metals or contaminants.

In Chapter 2 we have seen that oxygen would appear to be the most reactive contaminant. Figure 3.7 shows the normal incidence Auger spectra of the polished aluminium crystal recorded under identical conditions during the cleaning procedure (section 3.3). The peak at 510eV is due to the K $L_{23}L_{23}$ Auger transition of oxygen, present at the surface of the crystal in the form of a layer of passifying aluminium oxide. The peak at 270eV is due to the K $L_{23}L_{23}$ Auger transition of carbon and the 53eV feature is due to the LVV Auger transition of aluminium in aluminium oxide (ref:- 16). As the cleaning proceeds all these features become progressively smaller and an Auger feature at 68eV due to non-oxidised aluminium appears and grows in size. In the clean spectrum only aluminium Auger features can be seen.

Using the data in figure 3.7 and correcting for different amounts of signal averaging, we can obtain an order of magnitude estimate of the sensitivity to oxygen of the spectrometer and detection circuitry used in this study. Suppose that the Auger spectrum in figure 3.7(b) is predominantly due to aluminium oxide of stoichiometry, Al_2O_3 (ref:- 16) and that the peak to peak height of the oxygen Auger feature is proportional to the amount of oxygen in the sampled volume. The sample was usually considered 'clean' when this oxygen signal had been reduced to no more than that of the background noise fluctuation for 64 signal averaging scans . Typically, the oxygen signal was found to have been reduced by a factor of at least 60. Hence, within the sampled volume there is now one oxygen atom for every 40 (or more) aluminium atoms. Using SEAH and DENCH's inelastic mean free path compilation (ref:- 17) the sampling depth of the 510eV oxygen Auger electron is about 4 monolayers. If all of the remaining oxygen atoms are in or on the surface plane, then we would have an oxygen coverage of at most 4/40 = 1/10th of a monolayer. It is therefore suggested that an oxygen contamination level of as little as 1/10th of a monolayer or even less can be routinely detected.

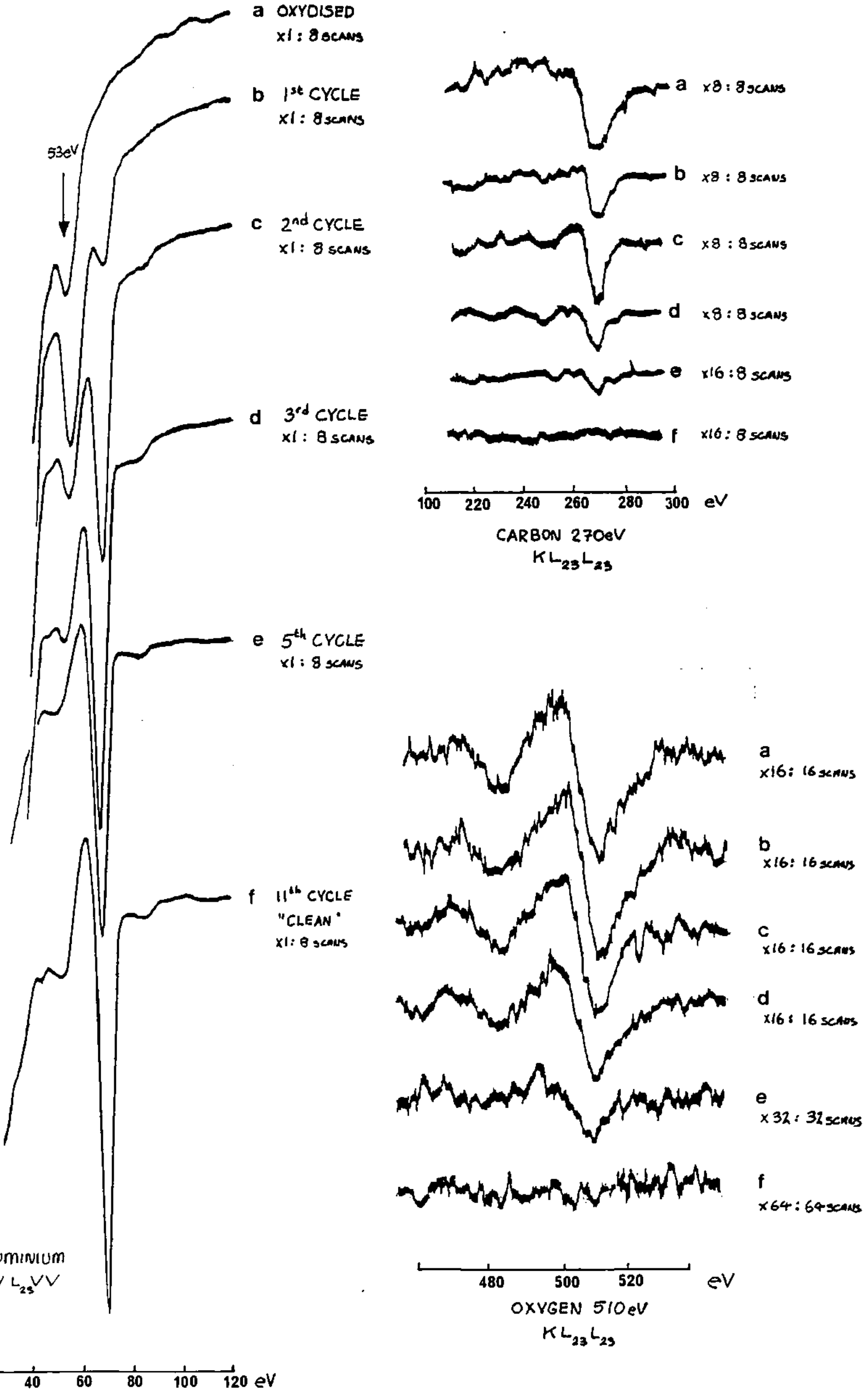

Figure 3.7: $\frac{dN}{dE}$ Auger spectra during cleaning procedure (E_p = 1 KeV, mod = 5V pK-pK).

Usually the sample received many more cleaning cycles than that required to reduce the oxygen signal below 'background level' and so at the beginning of each experiment at least, the sample may be considered clean. Similarly, when the alkali metal dispensers were properly outgassed the adsorbed alkali metal films were found to have no oxygen contamination beyond the effective detection threshold of (at most) 1/10th of a monolayer. To investigate the possibility of contamination further, AES studies were also made on very thick alkali metal layers which were deposited onto the crystal while it was held at liquid nitrogen temperatures (see Chapter 5). Again, no trace of any oxygen (or carbon) contamination was found, although for caesium multilayers a very small amount of potassium was detected.

Indirect evidence was found, however, for an alkali metal enhanced contamination rate. An experiment was performed in which the Auger signals for the crystal covered with one monolayer of potassium were studied as a function of time. During this experiment the AES beam was left on the sample and the evaporator was left running although shielded and otherwise unused. It was found that there was a gradual attenuation of the aluminium signal over the 2 hour duration of this experiment. No trace of any contamination, however, could be seen on the Auger spectra. Using SEAH and DENCH's inelastic mean free path compilation and the attenuation rate of the aluminium 68 eV Auger signal, a contamination rate of 1/30th of a monolayer per hour was estimated (which is below the estimated detection threshold for oxygen). As a matter of interest, the potassium Auger signal was unaffected - and this may imply that the contamination was in-plane or even under the potassium monolayer. The origin of this contamination is not known exactly: the rate is small enough to be due to the finite background pressure although CO outgassing from the hot parts of the electron gun may also be responsible if it is dissociated at the sample by the electron beam.

All experiments were therefore restricted to at most 3 hours duration (including the time taken for the sample to cool down from its annealing treatment).

Another possible explanation for the attenuations of the aluminium signal is that the incident Auger beam may anneal the overlayer. If the alkali metal deposit is not uniformly spread over the aluminium surface and there are regions of alkali metal that are 2 or 3 atoms thick, then impact with the high energy electron beam may cause the alkali metal to spread out more evenly. This would lead to an attenuation of the aluminium Auger signal, although the alkali metal Auger signal may remain unaltered. For the case of potassium or caesium where it appears that the coverage at room temperature saturates at one monolayer (see Chapters 2 and 4) this mechanism is probably unlikely. For sodium, where the mobility is lower and second layer growth is possible (see Chapter 2) electron beam effects may be important (ref:- 18) .

The apparatus was also equipped with a side incidence Auger gun. In principle the use of this gun would lead to a greater surface sensitivity because the primary excitation is confined more to the surface region (ref:- 5). Unfortunately, quantitative AES using the side incidence gun was found to be less reliable because the measurements were too sensitive to the small movements of the sample caused by the thermal distortion of the backing plate that occurred during the annealing treatments. Side incidence AES was used for spot checks on the contamination level and the results were in qualitative agreement with the normal incidence measurements.

3.7 Work function measurements

When two metals of different work functions are brought into electrical contact a contact potential difference (CPD) equal to the difference in the work function is formed between them (see figure 3.8(a)). Hence, if we measure this potential and if the work function of one of the metals is known, then the work function of the other can be determined. Of the many CPD measurement techniques (ref:- 19) two were used in this study :-

- * The electron beam retarding field technique (ref:- 9)
- * The secondary electron "cut-off" technique (ref:- 10)

In the first method the LEED gun is used to send a collimated low energy beam of mono-energetic electrons towards the sample. A retarding potential 'V' is applied to the sample and the sample current to earth 'I' is measured as a function of V. Figure 3.8(b) is a schematic diagram of the experimental set-up and figure 3.8(c) shows a typical I-V curve so obtained.

Changing the sample, or its surface conditions, by adsorbing an alkali metal, say, will shift the I-V curve along the voltage axis by an amount equal to the change in the work function if the curves remain parallel. In practice, parallelity was found to be good at the foot of the 'step' and so measurements were made of the shifts of the point representing 12% of the total current (see figure 3.8(c)).

In theory, however, adsorbate induced changes in the reflection coefficient (ref:- 20) could also cause apparent shifts in the curves. In addition to this, the large distance that the electrons have to travel to reach the com-

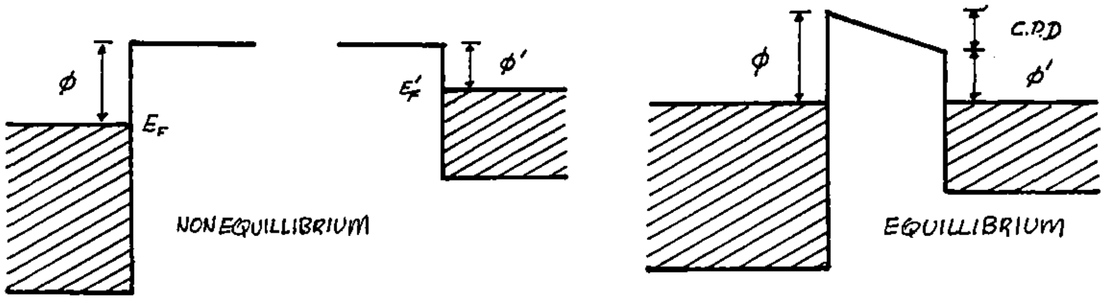

Figure 3.8(a): Diagram showing the CPD ($\phi - \phi'$) between two metals of dissimilar work functions, ϕ and ϕ'.

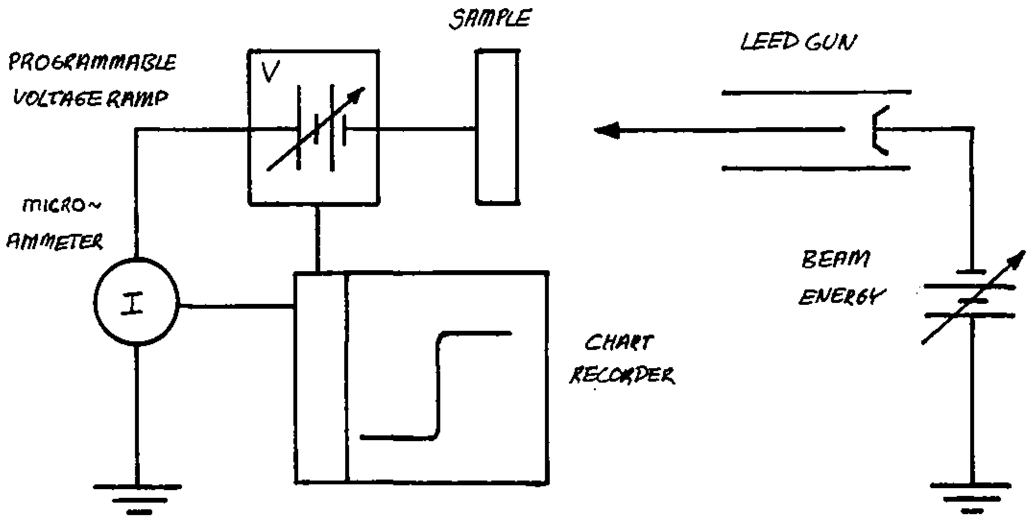

Figure 3.8(b): Schematic diagram of arrangement used for measuring the I-V characteristics of the sample.

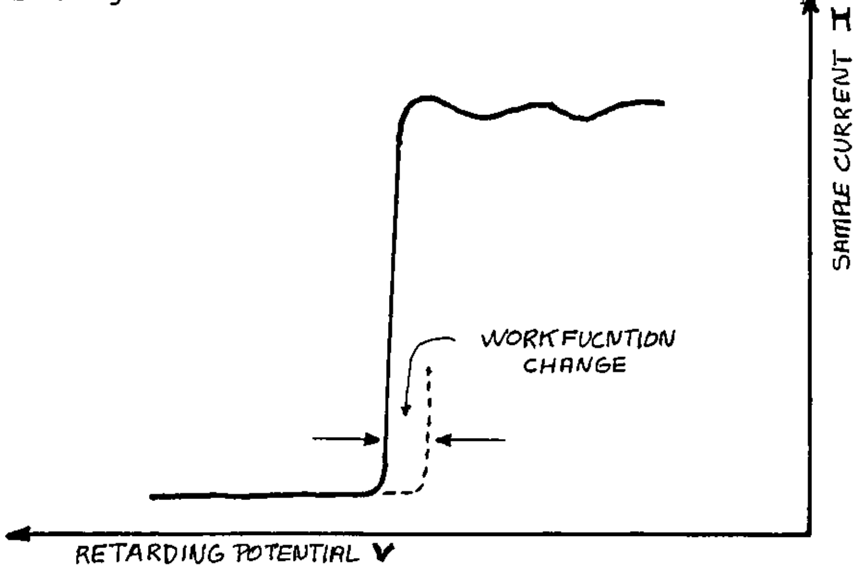

Figure 3.8(c): Typical I-V curve.

paratively small sample means that there is a chance that they may miss the sample and hit the backing plate instead (because the surrounding region is not field free). In order to check these measurements the second method was used.

Figure 3.9(a) shows the backscattered electron energy distribution, the N(E) or EELS spectra, as obtained by using the LEED optics as a retarding field analyser. Peak 'A' represents the elastically backscattered primary electrons, and peaks 'B' represent those backscattered primaries that have lost discrete amounts of energy by exciting plasma oscillations (see Chapter 5). The remainder of the spectrum may be loosely described as due to "secondary electrons" and is characterised by a large peak at low energies, 'C'. The details of the secondary electron production need not bother us yet. The important point here is that the cut-off near the origin is due to the CPD between the sample and the analyser which prevents the escape of very low energy electrons (energy $\lesssim$ 3eV).

In fact, figure 3.9(a) is misleading as it also contains a contribution from the secondary electrons produced at the analyser grids and the electron gun collimator (ref:- 11). This can be shown by biasing the sample negatively w.r.t. earth by -9 volts say (see figure 3.9(b)). The true sample secondaries now correspond to peak 'C^*' since they have acquired an additional 9 electron-volts of energy. By measuring the shifts of the point 'E', or, more accurately, the movement of the peak 'E^*' in the $\frac{dN}{dE}$ spectrum (figure 3.9(c)) corresponding to point 'E', <u>changes</u> in the work function can be found. These measurements yielded results that were identical to the first technique to within experimental error. To demonstrate that during these measurements the electron beam remained on the sample it was verified that LEED patterns would be observed at the same incident electron energy, with the -9 volt bias on the sample.

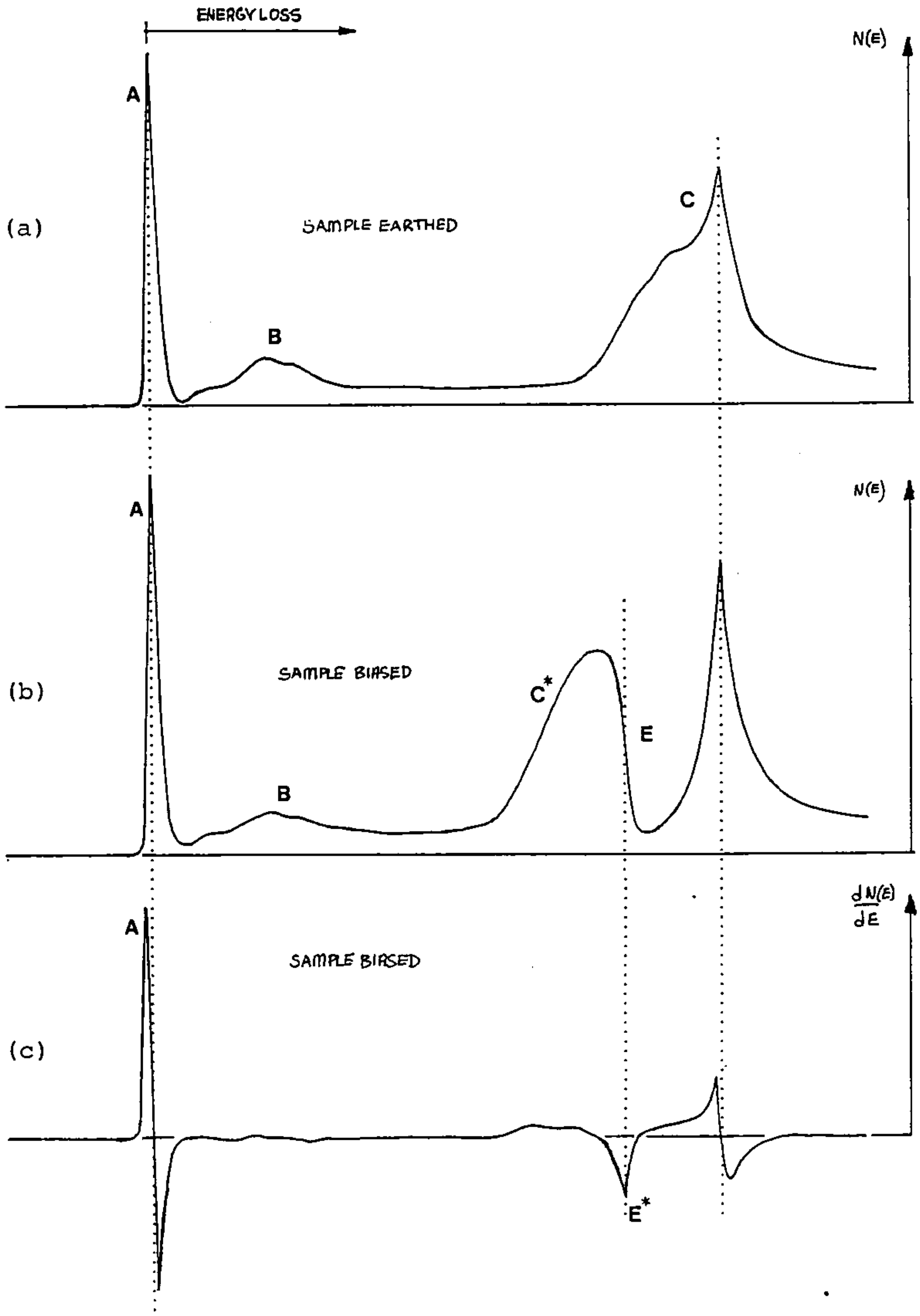

Figure 3.9(a): Top. N(E) spectrum, sample earthed.

Figure 3.9(b). Middle. N(E) spectrum, sample biased.

Figure 3.9(c). Bottom. $\frac{dN}{dE}$ (E) spectrum, sample biased.

REFERENCES

1. B.D. CULLITY: "Elements of X-ray Diffraction" (ADDISON-WESLEY, INC. MASSACHUSETTS U.S.A. 1967)
2. W.J. TEGART: "The Electrolytic and Chemical Polishing of Metals" (PERGAMON PRESS NEW YORK 1959)
3. A.E. HUGHES, Ph.D. thesis, University of London 1982
4. D. CHATTARJI: "The Theory of Auger Transitions" (ACADEMIC PRESS, LONDON 1976)
5. N.J. TAYLOR, Rev. Sci. Instrum. VOL. 40 No. 6 p.792 (1969)
6. E.L. GARFUNKEL and G.A. SOMORJAI. Surface Sci. 115 (1982) p.441
7. R.E. WEBBER and W.T. PERIA, Surface Sci. 14 (1969) p.13
8. C.E. ROJAS, Ph.D. thesis, University of London 1983
9. J.H. FRITZ and C.A. HAQUE, Rev. Sci. Instrum. VOL.44 No.4 p.394(1973)
10. A.U. MACRAE, K. MULLER, J.J. LANDER and J. MORRISON, Surface Sci. 15 (1969) p.483
11. J.A. CROSS, J. Phys. D: Appl. Phys. Vol.6 (1973) p.622
12. J.E. HOUSTON and R.L. PARK, Rev. Sci. Instrum. VOL. 43 No.10 (1972) p.1437
13. M-G. BARTHES-LABROUSSE and G.E. RHEAD, Surface Sci. 116 (1982) p.217
14. C. ARGILE and G.E. RHEAD, J. Phys. C: Solid State Phys. 30 (1982) L193
15. P.A. LYNN: "An Introduction to the Analysis and Processing of Signals" (MACMILLAN PRESS, LONDON 1979)
16. D.T. QUINTO and W.D. ROBERTSON, Surface Sci. 27 (1971) p.645
17. M.P. SEAH and W.D. DENCH, Surface and Interface Analysis VOL. 1 No. 1 (1979) p.2
18. A.P. JANSSEN, Surface Sci. 52 (1975) p.230
19. J.C. RIVIERE: "Solid State Surface Science, Vol.1" ed. by M. GREEN (MARCEL DEKKER, NEW YORK 1969) p.179

20. G.A. HAAS and R.E. THOMAS in Chapter 2 of "Techniques of Metal Research VI: Measurement of Physical Properties Part 1" ed. by BRUNSHAH and PASSAGLIA (WILEY-INTERSCIENCE, CHICHESTER 1972).

CHAPTER 4

LEED AND AES STUDIES OF POTASSIUM AND CAESIUM ADSORBED ON ALUMINIUM (111)

Introduction

In this chapter the LEED data obtained from the adsorption of potassium and caesium is presented and discussed. By comparing the structured models with AES measurements the saturation monolayer coverage for potassium and caesium on aluminium (111) at room temperature is deduced. This information is used to calibrate the crystal current measurements, described in Chapter 3, which will be used in Chapter 5 as a simple method of assessing the alkali metal coverage.

4.1 Potassium on aluminium (111) : LEED and AES

Figure 4.1, photographs a ⟶ e, show the changes in the normal incidence LEED pattern that occur as potassium is adsorbed onto the aluminium (111) crystal surface at "room temperature". As deposition commences the substrate beams (photo a) become less intense and extra spots appear ($\theta \approx 0.15$, see later) and develop into the well defined pattern shown in photo b. (No diffraction spot movement, however, is observed). This pattern is analysed in figure 4.2a, where it is shown to be due to a ($\sqrt{3} \times \sqrt{3}$) R30° surface structure which would imply a potassium coverage of $\theta = 1/3$ if all the potassium is present as an ordered overlayer. A substantial increase in relative exposure time is then necessary to produce any further changes in the LEED pattern. These changes are the gradual disappearance of the ($\sqrt{3} \times \sqrt{3}$)R30° diffraction beams accompanied by the appearance and growth of 1/2 order beams (photo c) to result ultimately in the diffraction pattern shown in photo d - which has the same symmetry as one due to a p(2x2) surface structure.

No further structural changes were observed, even when much higher fluxes of potassium were used. If it takes 6 minutes to produce the well defined ($\sqrt{3} \times \sqrt{3}$)R30° diffraction pattern, then typically an additional 90 minutes or more (for the same potassium flux) is required to produce the final diffraction pattern (photo d). All of the diffraction patterns seen here for K on Al were found to be quite stable and observable at least 24 hours after the final potassium deposition: mild heating ($T \approx 100$°C), however, was found to reverse the diffraction pattern changes.

In summary, the same sequence of diffraction patterns was observed here for K on Al(111) as was seen by PORTEUS

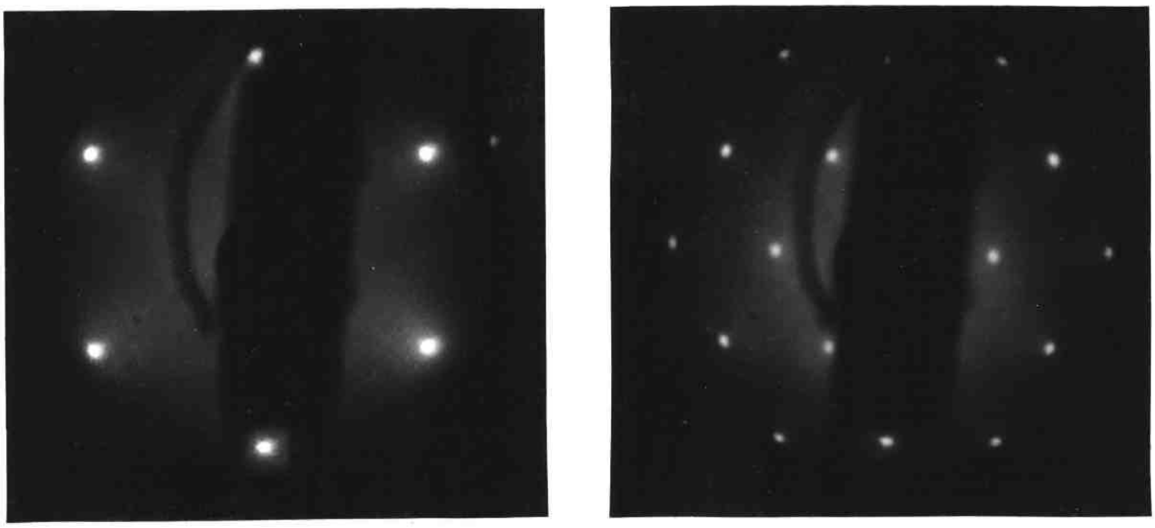

(a) clean Al(111)

(b) K($\sqrt{3}$ x $\sqrt{3}$)R30°/Al(111)

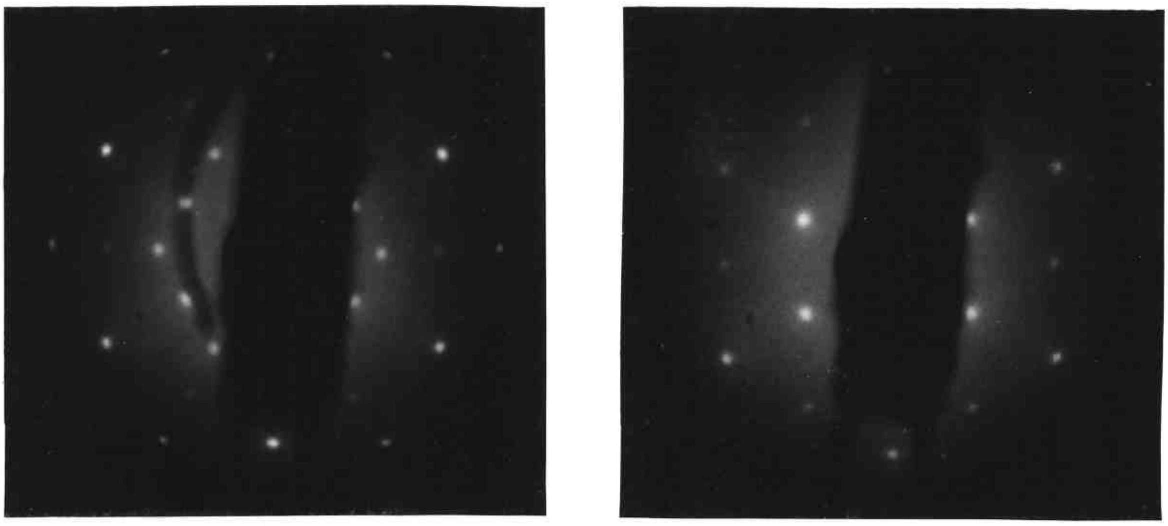

(c)

(d)

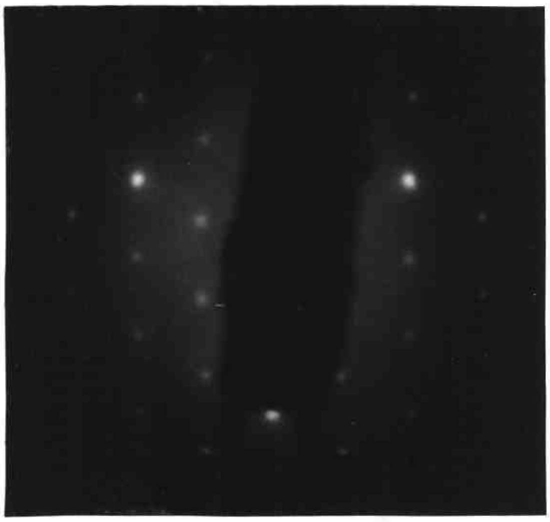

(e)

Figure 4.1: Normal incidence LEED patterns for clean and potassium covered (see text) Al(111). For photos (a) → (d) a primary beam energy of 68.8eV was used. A beam energy of 97eV was used for photo (e) which corresponds to the same structure as photo d.

(a)

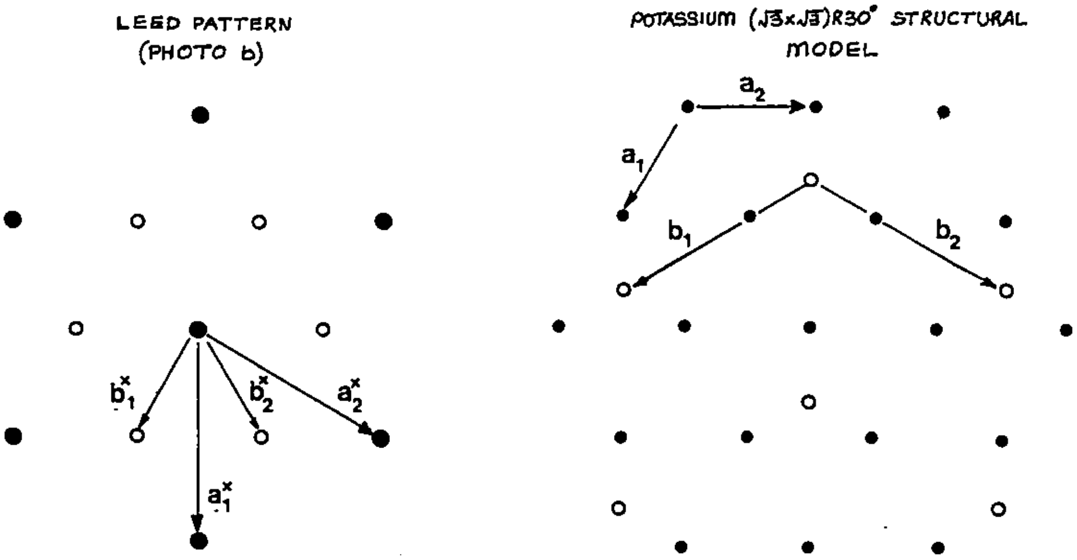

a_1 & a_2 are the primitive unit cell vectors of the Al(111) surface.

a_1^x & a_2^x are the corresponding reciprocal lattice vectors.

b_1 & b_2 are the primitive unit cell vectors of the overlayer.

b_1^x & b_2^x are the corresponding reciprocal lattice vectors.

(b)

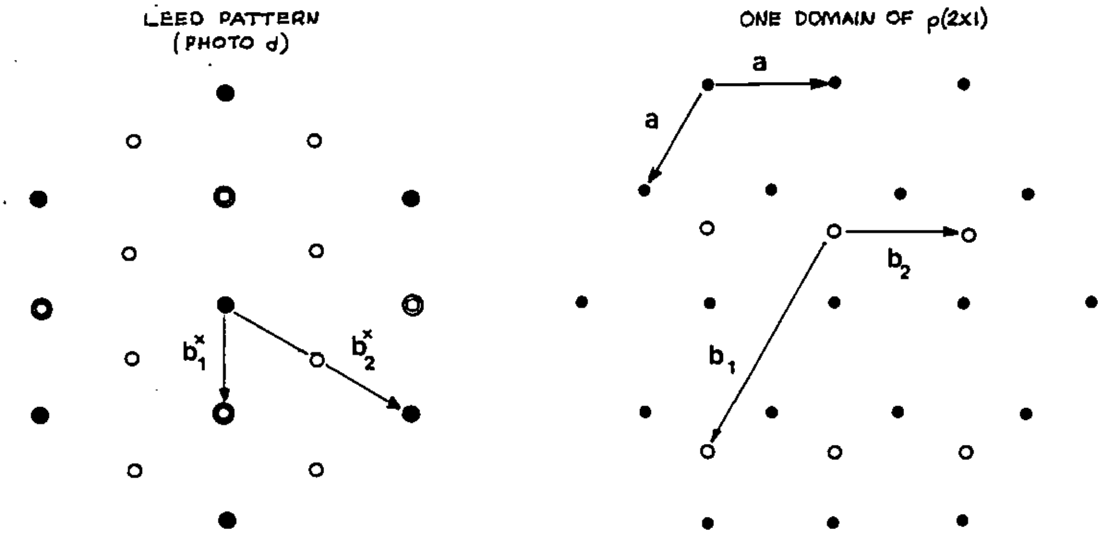

Figure 4.2(a) shows the LEED pattern of photo b and the real space K $(\sqrt{3} \times \sqrt{3})$R30° structure model

(b) shows the LEED pattern of photo d and PORTEUS' structural model: one domain of p(2x1) produces the ' ⭘ ' diffraction spots, 3 domain generate the entire diffraction pattern.

(Chapter 2) for Na on Al(111) - the only difference is that PORTEUS did not observe an apparent change in the sticking coefficient during this process. Once again no spot movement or ring patterns were seen.

PORTEUS explains his final diffraction pattern in terms of 3 domains of p(2x1) structure ($\theta = \frac{1}{2}$; see figure 4.2b) because a true p(2x2) structure requires a coverage of only $\theta = 1/4$ which is less than that required to produce the $(\sqrt{3} \times \sqrt{3})$R30° features - and these were seen first. Later, however, we shall have need to question this assignment and suggest an alternative interpretation of the diffraction pattern of photo d.

Figure 4.3 shows the evolution of the peak to peak heights of the aluminium 68 eV $L_{23}VV$ and the potassium 251 eV $L_3M_{23}M_{23}$ $\frac{dN}{dE}$ Auger signals as a function of the time for which the crystal was exposed to the potassium flux. The 251 eV $L_3M_{23}M_{23}$ potassium Auger signal corresponds to the strongest potassium Auger transition (ref:- 1) and occurs at an energy where fortunately the background signal in the dN/dE spectrum is horizontal and free from substrate peaks. Signal averaging was used to increase the signal to noise ratio of the potassium peaks by a factor of $\sqrt{8}$. Two examples of the potassium Auger signal, one at low coverage and one at high coverage, are also shown in figure 4.3. No change in the potassium peak shape with increasing potassium coverage was observed. The aluminium 68 eV Auger feature is the most prominent Auger transition of clean aluminium and in fact the second strongest Al Auger transitions (KL_3L_3) occur at 1396 eV and are outside the detection range of the Auger spectrometer used in this study.

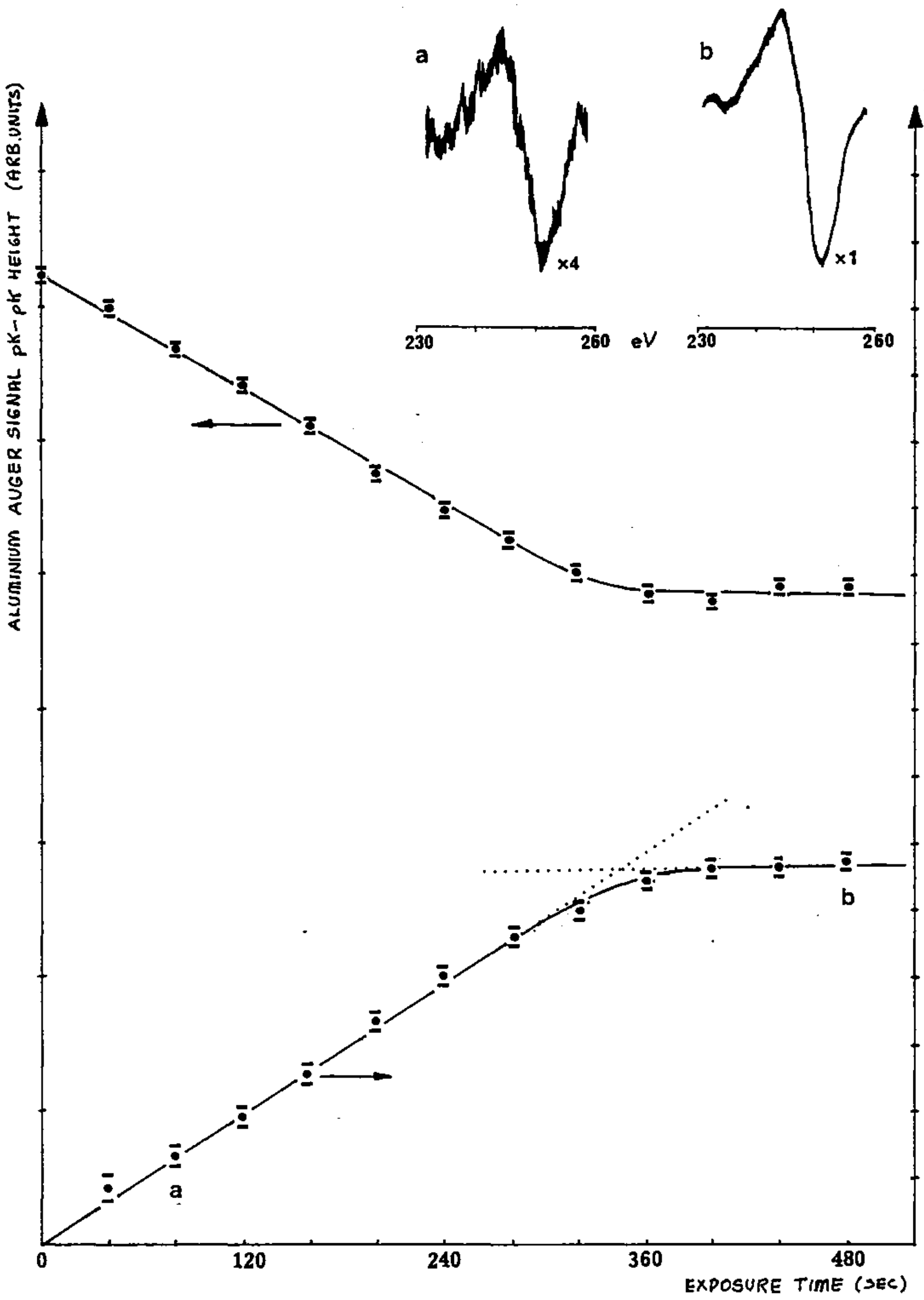

Figure 4.3: Graph of the pK-pK heights of the Al 68eV (LVV) and K 251eV ($L_3M_{23}M_{23}$) dN/dE Auger signal versus exposure time. Insert gives examples of the potassium signal at (a) low and (b) high coverages.

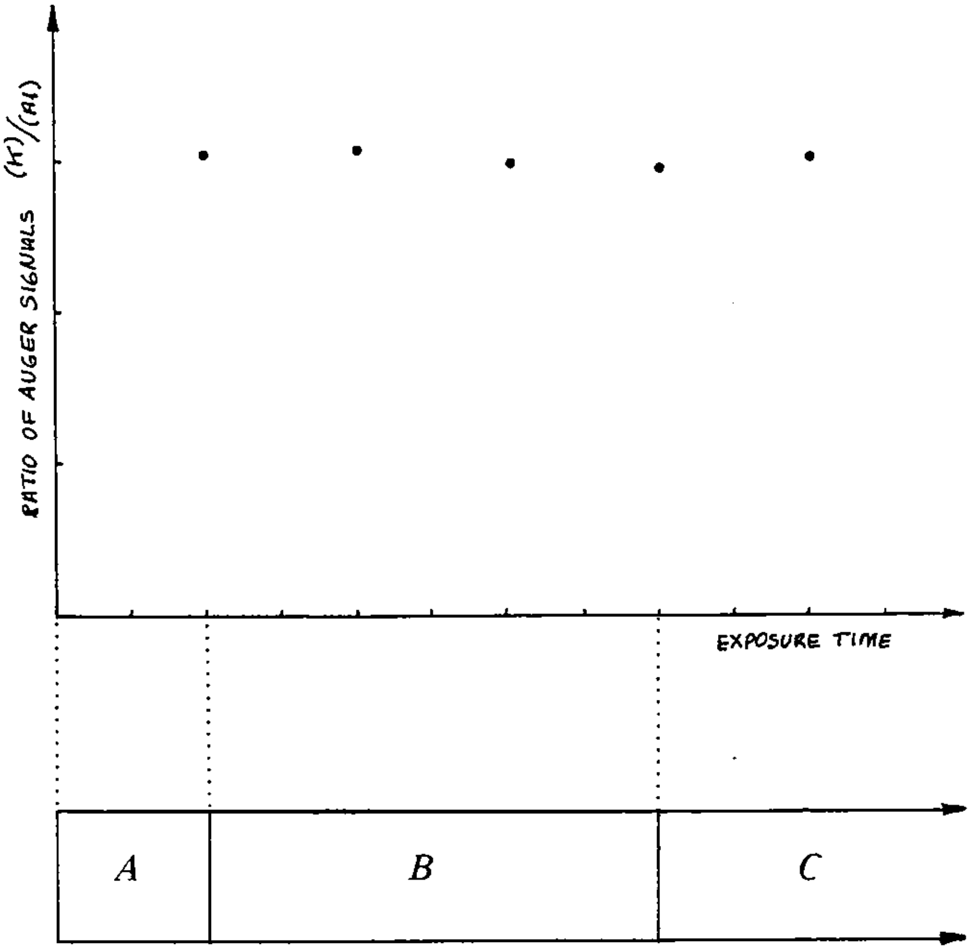

Figure 4.4: Ratio of $\frac{dN}{dE}$ Auger signals (potassium 251eV pK-pK Auger signal/aluminium 68eV pK-pK Auger signal) as a function of extended exposure time.

Region A corresponds to the $(\sqrt{3} \times \sqrt{3})R30°$ structure;
Region B corresponds to photo c;
Region C corresponds to photo d.

From figure 4.3 it can be seen that there is a gradual attenuation of the aluminium Auger feature as the potassium coverage increases. After ≈ 360 secs of exposure the potassium signal appears to saturate and there are then only very slow variations in both of the Auger signals.

The diffraction pattern due to the $(\sqrt{3} \times \sqrt{3})R30°$ structure is first observable from a time ≈ 140 secs onwards and becomes fully developed by the onset of the 'plateaus', i.e. at the break points. Attempts to perform AES on the final structure or during the extended exposure times necessary to produce it, however, yielded results that implied no significant change in the potassium coverage beyond the break points. Figure 4.4 shows the ratio of the 251 eV potassium Auger peak to the 68 eV aluminium Auger peak as a function of time for a much higher potassium flux (i.e. increased getter temperature). Also shown is an indication of the corresponding LEED pattern changes that occur under the same conditions.

These Auger measurements appear to conflict with the accompanying LEED pattern changes and with the results of PORTEUS, who observed that for sodium on aluminium (111), the sodium Auger signal increased (linearly) during the same sequence of diffraction pattern changes.

A possible explanation for the behaviour seen here is that the potassium coverage is really increasing beyond $\theta \simeq 1/3$ (as implied by the LEED pattern changes) but that the energetic Auger beam (1 KeV) causes potassium atoms to desorb or diffuse from the beam-impact area. Beam induced diffusion has been observed for Na on MgO substrates (ref:- 2) and in appendix 1 some evidence for a "beam annealing effect" for thick layers of sodium on aluminium (100) is presented.

No evidence, however, of any pronounced beam effects was found for the potassium coverages achieved in this study: a "p(2x2) pattern" when cooled to -200°C still showed there to be no increase in the potassium Auger signal; there was no change in the instantaneous potassium Auger signal, as measured directly from the phase sensitive detector (with a small time constant) even when the sample was rapidly translated perpendicularly to the Auger beam. In addition to this, during a LEED experiment no structural changes (i.e. a reversal of the diffraction pattern sequence) were observed when the primary beam energy was momentarily increased to 1 KeV. It would seem that the break points and plateaus in figure 4.3 are not electron beam induced.

It is therefore necessary to take the Auger data of figures 4.3 and 4.4 at 'face value' and question instead the origin of the diffraction pattern changes.

Figure 4.5 shows a hard-sphere model of the potassium $(\sqrt{3} \times \sqrt{3})$R30° surface structure. In this diagram the size of the potassium and aluminium atoms are drawn proportional to their metallic radii (from ref:- 3). It can be seen that the potassium $(\sqrt{3} \times \sqrt{3})$R30° structure covers nearly all of the aluminium surface. Attempts to explain the final diffraction pattern (photo d) in terms of 3 domains of p(2x1), however, are not only inconsistent with the Auger data (which implies no increase in potassium coverage beyond $\theta = 1/3$), but are also incompatible with a hard-sphere model based on metallic radii - the potassium atoms are just too big and would require a~40% decrease in size in order to form a p(2x1) structure! Even in PORTEUS' case a ~23% contraction in the

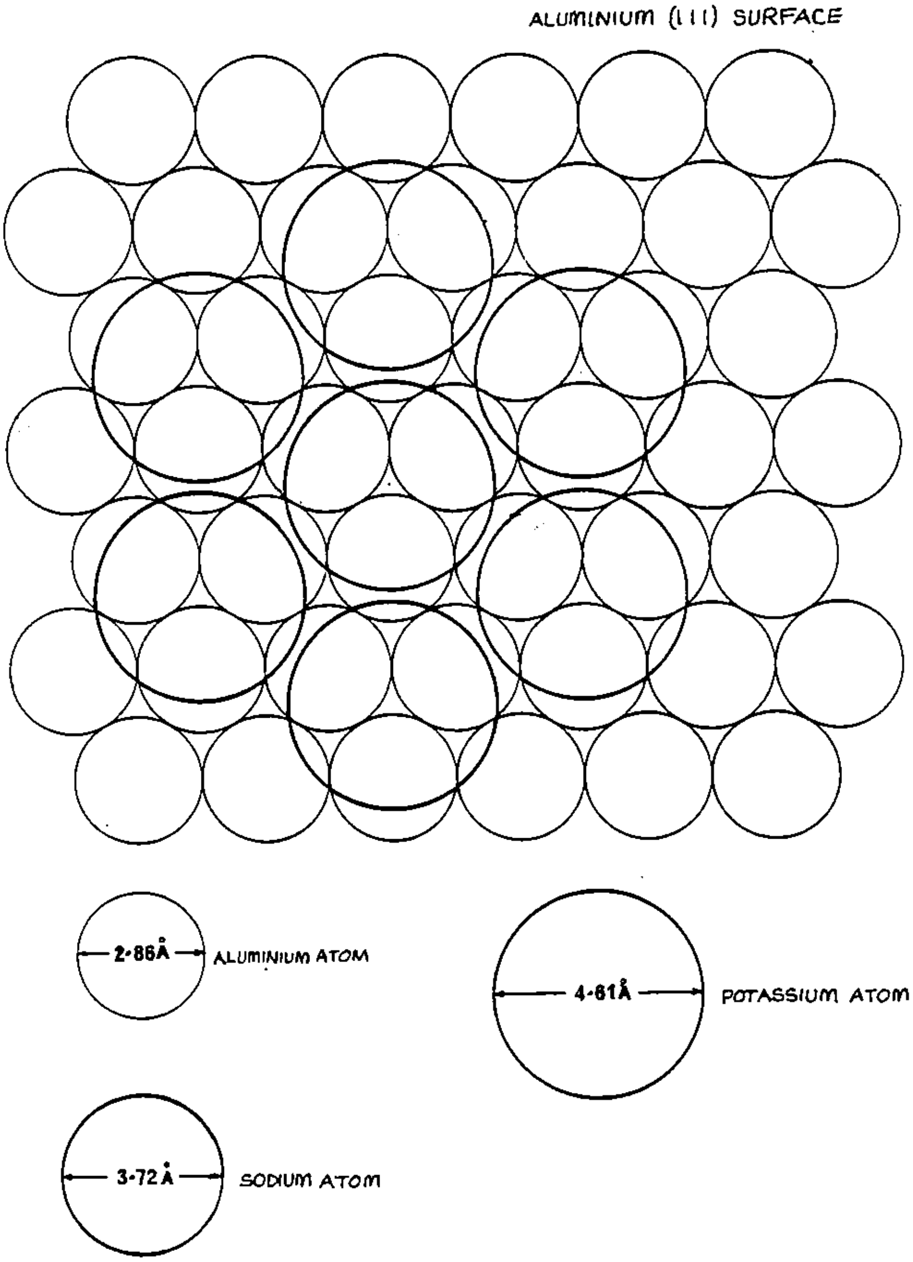

Figure 4.5: A hard sphere model (using metallic radii (ref:- 3)) of the potassium $(\sqrt{3} \times \sqrt{3})R30^\circ$ structure. For reference the metallic size of the sodium atom is also indicated.

size of the sodium atoms would be required, but he makes no mention of this. Such large reductions in the size of the potassium and sodium atoms are extremely hard to justify and so an alternative structural model is required. (In Chapter 2 it was mentioned that often adsorbed alkali metal monolayers are denser than the bulk alkali metal: the reduction in the atomic size, however, is measured in terms of a few tenths of an Angström).

4.1.1 Discussion of the potassium LEED and AES data

If we rule out the possibility of 3 domains of p(2x1) we have a paradoxical situation in that the ($\sqrt{3}$ x $\sqrt{3}$)R30° structure gives way to an apparent p(2x2) structure when the exposure time is increased. This seems to be contradictory because a potassium p(2x2) structure would be less dense than a potassium ($\sqrt{3}$ x $\sqrt{3}$)R30° structure.

In fact, it appears that the ($\sqrt{3}$ x $\sqrt{3}$)R30° structure is itself a good candidate for a saturated monolayer structure. Identical structures have been observed for potassium adsorbed onto the (111) plane of platinum. Platinum, like aluminium, is a face centred cubic metal but has a 3% smaller lattice parameter. PIRUG et al (ref:- 4) observed that when potassium was adsorbed onto Pt(111) a ($\sqrt{3}$ x $\sqrt{3}$)R30° structure was formed at saturation coverage. GARFUNKEL and SOMORJAI (ref:- 5) observed their diffraction patterns as potassium was desorbed from a platinum (111) surface. They saw a hexagonal close packed structure at full monolayer coverage ($\theta = 0.36$) which was then followed by a ($\sqrt{3}$ x $\sqrt{3}$)R30° structure at a slightly lower coverage ($\theta \simeq 0.33$). GARFUNKEL and SOMORJAI found no evidence to suggest that multilayer growth of potassium occurs at room temperature under conditions of ultra high vacuum, and they present a potassium 251 eV Auger signal versus exposure time curve that is similar to figure 4.3.

The evidence therefore suggests that not only is the final pattern not due to domains of p(2x1) structure, but that it corresponds to changes that occur after a complete monolayer of potassium has been adsorbed.

Three possible explanations of the observed behaviour are:-

(a) STRANSKI-KRASTANOV GROWTH-MODE

(b) COMPOUND FORMATION

(c) CONTAMINATION

and these will now be discussed in turn.

(a) The explanation of the observed behaviour in terms of a STRANSKI-KRASTANOV growth mode, i.e. crystallite growth on top of a completed monolayer, is unlikely - even though it can lead to Auger signal versus adsorbate deposition - time curves that are similar to figure 4.3 (see ref:- 6). The high vapour pressure of potassium would mean that any crystallites would be unstable, and it is doubtful whether such large accompanying LEED pattern changes could occur undetected by AES - especially since in this study both LEED and AES sampled the same area.

(b) Compound formation could also lead to plateaus in Auger signal versus deposition-time curves, since the fixed stoichiometry of the compound will be reflected in the Auger signals (ref:- 6). Alkali metals, however, have very low solubilities in bulk aluminium (ref:- 7), and in Chapter 1 it was noted that theoretical calculations imply bulk alkali metals have a high activation energy for diffusion through the aluminium surface. The possibility of a surface compound or alloy forming with a p(2x2) symmetry cannot, however, necessarily be ruled out. Surface alloys have been observed even when there is no bulk phase, such as, for example, Cu on W(100) (ref:- 8). A full LEED analysis in order to find the contents of the unit cell and spectroscopic data would be required to verify this model.

(c) Perhaps the most likely explanation of the observed behaviour, however, is that the diffraction pattern changes that occur after the formation of the $(\sqrt{3} \times \sqrt{3})R30°$ structure are <u>not</u> due to potassium, but are due to residual impurities in the potassium flux. The Auger data implies that the potassium coverage saturates when the $(\sqrt{3} \times \sqrt{3})R30°$ structure is complete. This structure is a good candidate for a close packed potassium monolayer and no more potassium is expected to stick at room temperature. Prolonged exposure to the potassium flux after the potassium coverage has saturated will therefore only encourage the contamination level to increase. In Chapter 2 it was noted that the most probable location of 'impurity' atoms is either <u>on</u> the alkali metal layer or <u>under</u> it - in either of these locations the impurity atoms will eventually destroy the order of the potassium $(\sqrt{3} \times \sqrt{3})R30°$ structure, causing its diffraction beams to disappear (photo c). In fact, because a new diffraction pattern is formed (photos c,d) it is probable that the impurities burrow under the saturated potassium layer to form an ordered structure with a disordered potassium layer on top (the double layer model).

This explanation is consistent with the observation made on deliberate co-adsorption studies where it is often found that new diffraction patterns are seen, which neither adsorbate alone would produce (see Chapter 2).

However, no proof of this explanation can be offered here. Contamination of the potassium layers was looked for, and even the apparent p(2x2) structure showed no detectable traces of impurities (in particular no oxygen). This may cast doubt on this explanation, or alternatively on the estimated sensitivity of the Auger spectrometer used in this study, although it is worth pointing out that even through it is unlikely that hydrogen would stick to the layers, its presence cannot be detected with AES.

As a matter of interest, PORTEUS's results are not inconsistent with this explanation, since the observed increase of the sodium Auger signal is no guarantee that it is solely responsible for the accompanying LEED pattern changes.

Because the appearance of the final diffraction pattern (photo d) obviously indicates some sort of anomalous behaviour, it will be assumed that the potassium coverage saturates with the formation of the complete $(\sqrt{3} \times \sqrt{3})$R30° structure, i.e. at a potassium coverage of 4.7×10^{14} atoms cm^{-2}. From graph 4.3, the coverage at which the $(\sqrt{3} \times \sqrt{3})$R30° beams are first observable is approximately 2.1×10^{14} atoms cm^{-2} ($\theta \simeq 0.15$).

4.2 Attempted investigation of the growth of the potassium $(\sqrt{3} \times \sqrt{3})$R30° structure

In Chapter 2 it was noted that the LEED pattern changes which PORTEUS observed for sodium adsorption on aluminium could be interpreted in terms of some kind of two dimensional island growth mechanism: the LEED pattern from an array of small disconnected islands will be a combination of the substrate reflections and the diffracted beams from the islands which will be broadened by the island shape transform. The intensities from the individual islands will add so that as the total area covered by the islands increases this diffracted intensity will also increase. If the mean island size increases we will also see a reduction in the size of the diffracted beams, i.e. a sharpening of the diffraction spots. During island growth observed with LEED, diffraction spot movement does not occur; only the intensity profiles are expected to change.

Because the changes that occur when potassium is adsorbed on aluminium (111) also imply island growth, attempts were made to investigate this further. Photographs of the LEED patterns were taken during the growth of the K($\sqrt{3}$ x $\sqrt{3}$)R30° structure and the intensity profiles of the beams from this structure were obtained by microdensitometry (see appendix 2). These intensity profiles of one of the ($\sqrt{3}$ x $\sqrt{3}$)R30° beams are shown in figure 4.6. No beam narrowing was observed, only an increase in the intensity occurs as the coverage increases.

It appears that the 'maximum resolvable distance'* of the LEED optics used in this study is too small to be useful for this type of analysis and so the approach was abandoned (ref:- 9)*. However, by integrating the area under the curves of figure 4.6, it was shown that the intensities of the ($\sqrt{3}$ x $\sqrt{3}$)R30° beams reached a constant value at an exposure time which coincided with the plateaus in the Auger signals which agrees with the more subjective visual observations reported earlier (see figure 4.7).

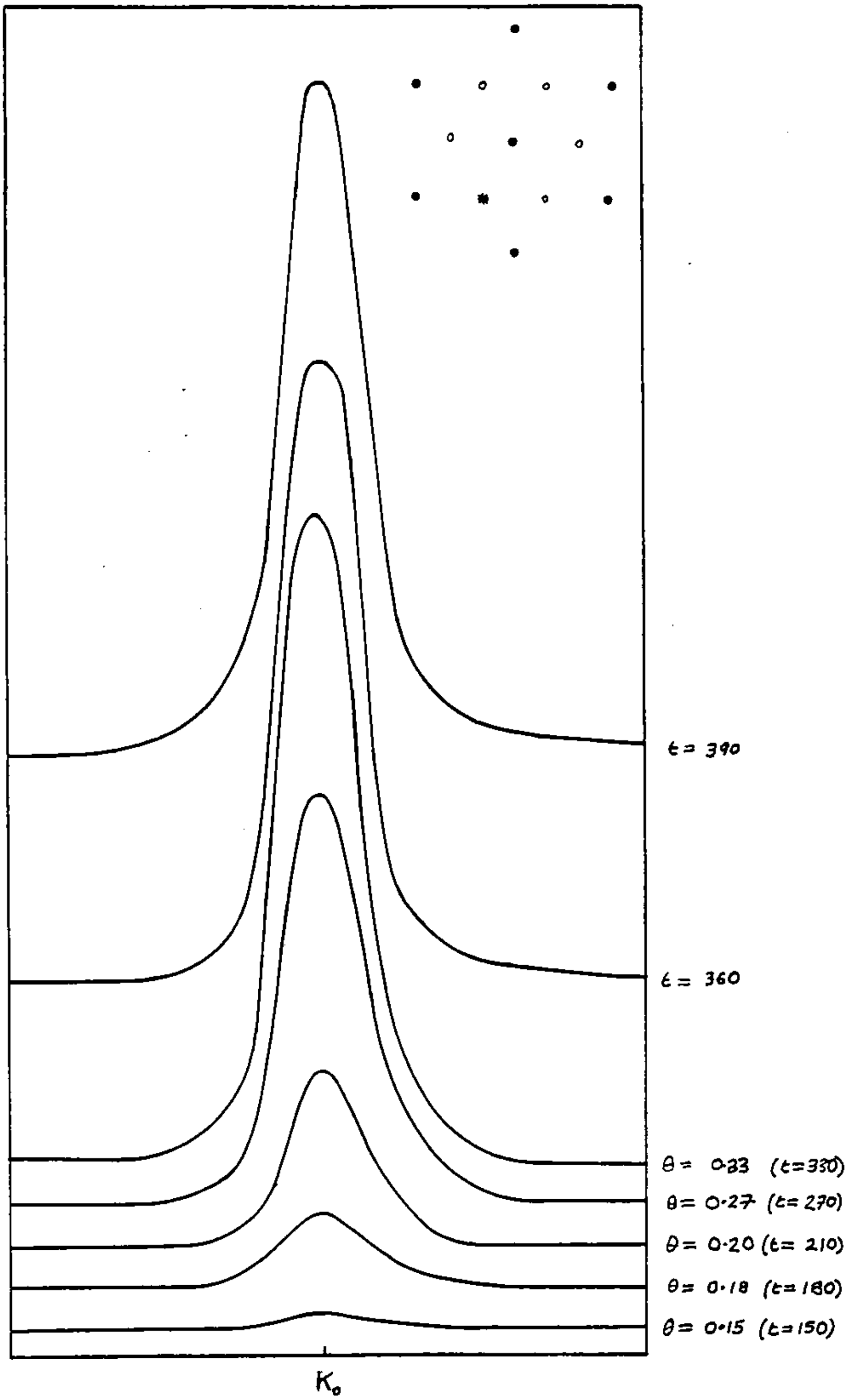

Figure 4.6: LEED beam intensity profile (arb. units) of the K($\sqrt{3}$ x $\sqrt{3}$)30° beam (shown in insert), as a function of coverage (θ) and exposure time (t). (See figure 4.7).

See appendix 2.

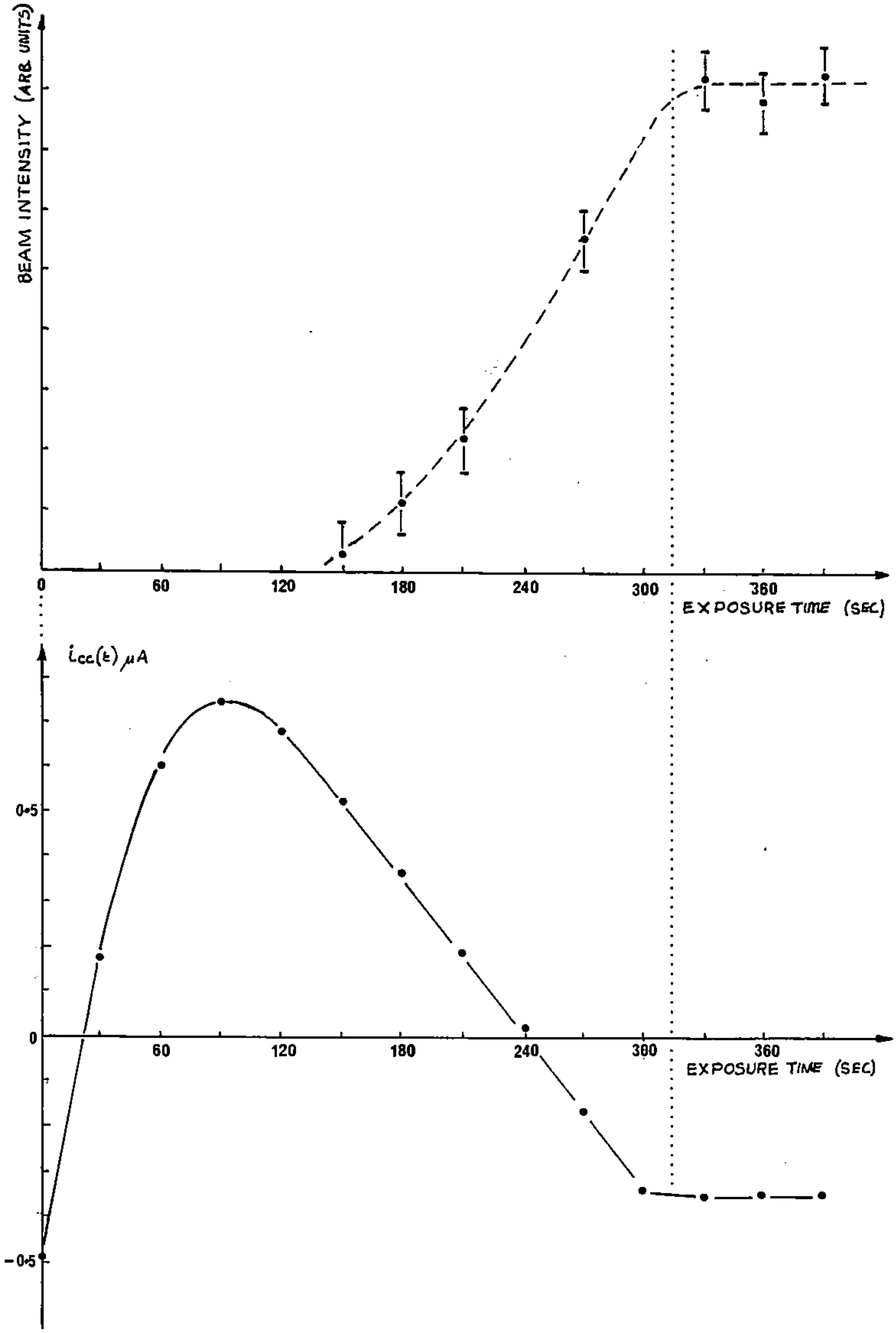

Figure 4.7: (top) Intensity of the potassium ($\sqrt{3}$ x $\sqrt{3}$)R30° diffraction beam of figure 4.6, as a function of exposure time; (bottom) The accompanying crystal current measurements, $i_{cc}(t)$, used to calibrate the coverages in figure 4.6 (see section 4.4.

4.3 Caesium on aluminium (111): LEED and AES

Figure 4.8 photos f$\longrightarrow$j show the changes that occurred in the normal incidence LEED pattern when caesium was adsorbed onto the aluminium crystal at room temperature. Initial adsorption causes a reduction in the intensity of the substrate beams and at $\theta \approx 0.14$ (see later) an extremely faint hexagonal array of streaky spots appears. These spots become more intense (photo g: $\theta \approx 0.16$: see later) and move away from the (0,0) beam as the caesium coverage increases (photos g,h,i) to produce the diffraction pattern of photo j ($\theta = 0.28$: see later). No further changes in the diffraction pattern were observed, except for an increase in the background intensity after prolonged exposure to the Cs flux. The diffraction patterns were found to be stable and observable, though with an increased background intensity 24 hours later. The diffraction pattern sequence was found to be quite reproducible.

In addition to the expanding array of hexagonal spots, diffuse lines of intensity, indicative of disorder (ref:- 10) develop towards the end of the diffraction pattern sequence. See photo j. These lines originate from the 'extra spots' (other than those already mentioned) that are present in the LEED patterns of intermediate coverages. These extra spots are at their brightest in photo i and appear to move along the lines, connecting them as the coverage is changed. It was not found possible to follow the movement of these features in a detailed way, however, since slight coverage changes from that of photo i ($\theta \approx 0.21$: see later) resulted in a substantial reduction in their intensity.

An attempt was made to find a structural model that could produce the diffraction pattern shown in photo i since

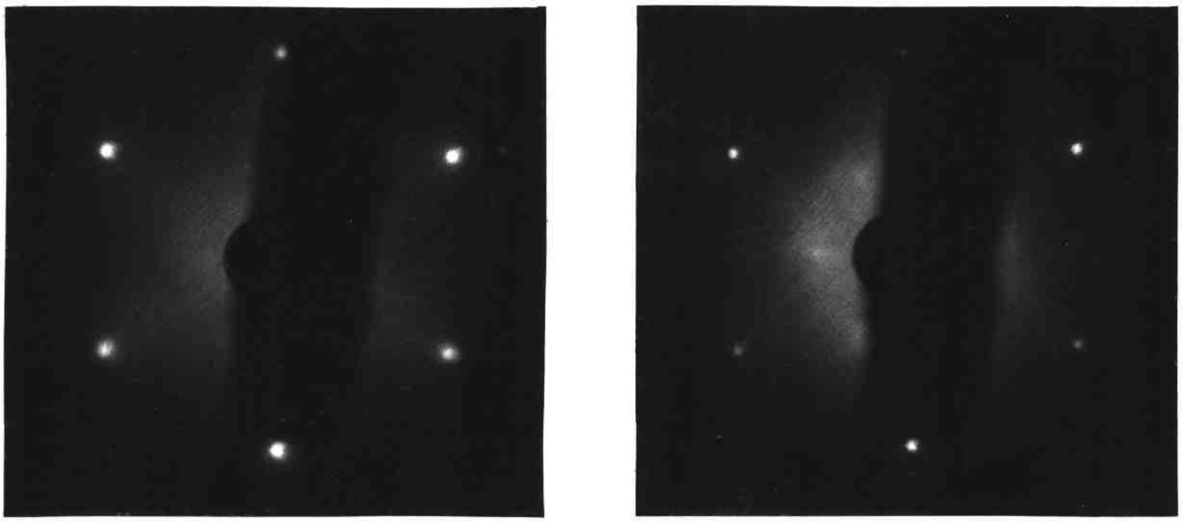

(f) clean Al (111)

(g) t = 210 secs ($\theta \approx 0.16$)

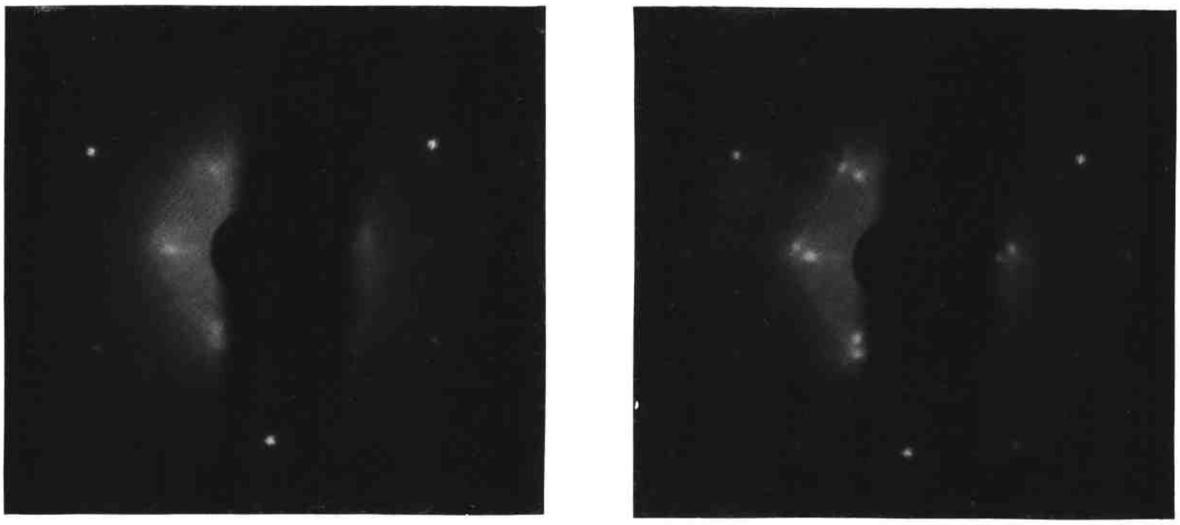

(h) t = 240 secs ($\theta \approx 0.19$)

(i) t = 270 secs ($\theta \approx 0.21$)

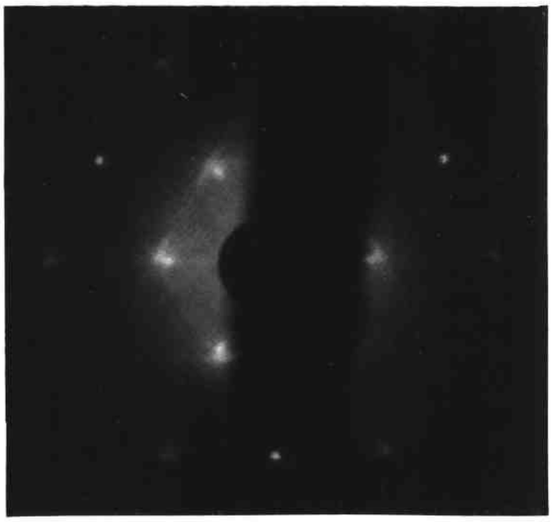

(j) t = 360 secs ($\theta = 0.28$)

Figure 4.8: Normal incidence LEED patterns (primary beam energy = 62.2eV) for clean and caesium exposed Al(111) surfaces. The exposure times are related to Auger signals in figure 4.10 and the approximate coverages are deduced from a structural model of the saturated monolayer (see later).

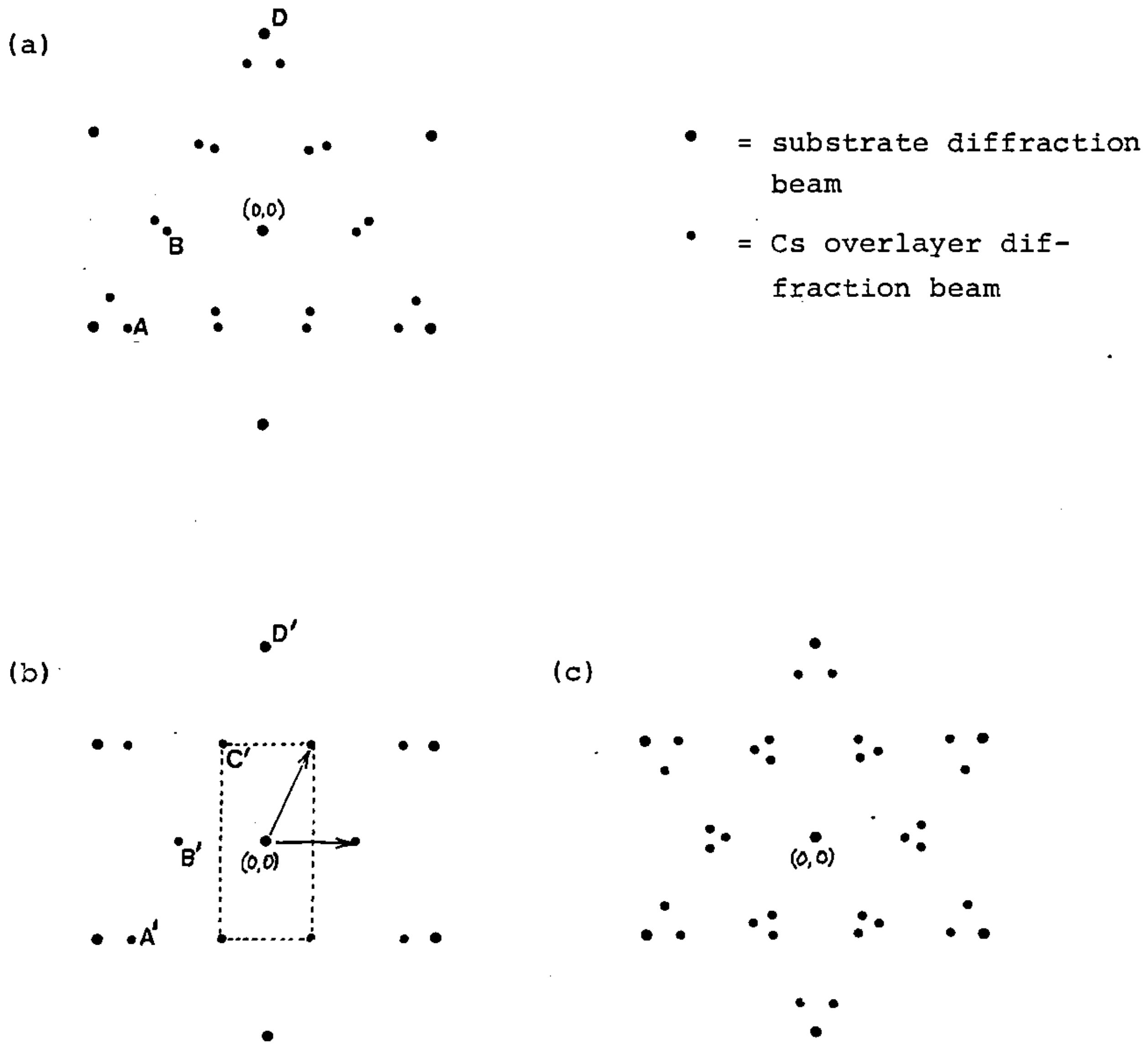

Figure 4.9: (a) shows a scale diagram of photo i; (b) shows a superposition of the reciprocal lattice of the Al(111) surface and the reciprocal lattice of a slightly distorted close packed Cs(110) plane. (Bulk Cs has a body centred cubic structure). 3 rotations of the latter produce (c), which is very similar to (a) (dynamical scattering would account for the intensity variations of the spots). However, the spots ABD do not line up as they ought if the structural model (b) was correct. (A full LEED intensity study at other primary beam energies, however, would be a much more rigorous test of the model).

double diffraction between the substrate and the overlayer (if it is assumed to be of hexagonal symmetry given by the inner array of spots) does not appear to be the cause of the extra spots. A model based on the assumption that, as the coverage reaches saturation, the Cs atoms will try to adopt a distorted hexagonal structure reminiscent of the close packed (110) plane of bulk caesium appeared promising at first, but failed to predict the spot positions with sufficient accuracy. (The details of the model are shown in figure 4.9. Figure 4.9(a) shows a scale diagram of photo i, in which only the most intense spots are indicated. Figure 4.9(b) shows a reciprocal lattice derived from a slightly distorted Cs (110) plane superimposed on the substrate reciprocal lattice. Three rotations of this 'Cs lattice' yield the pattern shown in figure 4.9c, which is very similar to the real diffraction pattern. On closer examination, however, it can be seen that points A, B, D on figure 4.9a do not line up as they ought if the model was correct). No other likely models could be found and so no detailed explanation can yet be offered for the structure of the caesium layer at this intermediate coverage ($\theta \approx$ 0.21).

Figure 4.10 shows the variation of the aluminium and caesium ($\frac{dN}{dE}$) Auger signals as a function of exposure time. Unfortunately, the Cs 49eV $N_5O_3O_3$ Auger feature (ref:- 1) that was used to characterise the caesium coverage is superimposed on one of the satellites of the aluminium 68eV $L_{23}VV$ Auger feature (see figure 4.11). This is why the caesium coverage curve does not pass through the origin and the extrapolation from high coverages (the dotted line in figure 4.9) gives a much better estimation of the low coverage signal. In principle, the high energy Cs M N_5N_5 ($\sim$560eV) Auger

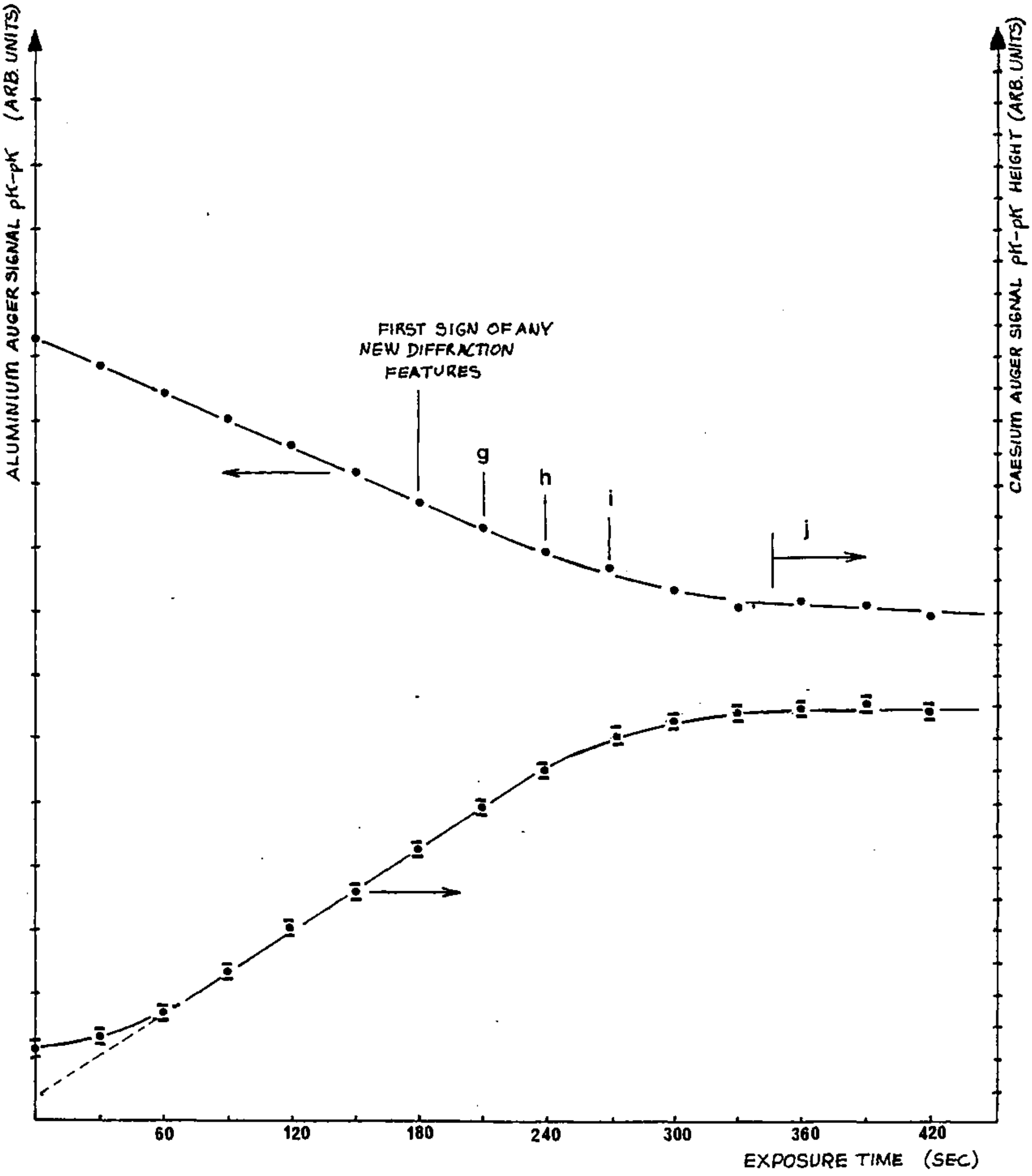

Figure 4.10: Graph of the pK-pK heights of the Al 68 eV (LVV) and the Cs 49 eV ($N_5O_3O_3$) dN/dE Auger signals versus exposure time. The letters correspond to the photographs of figure 4.8.

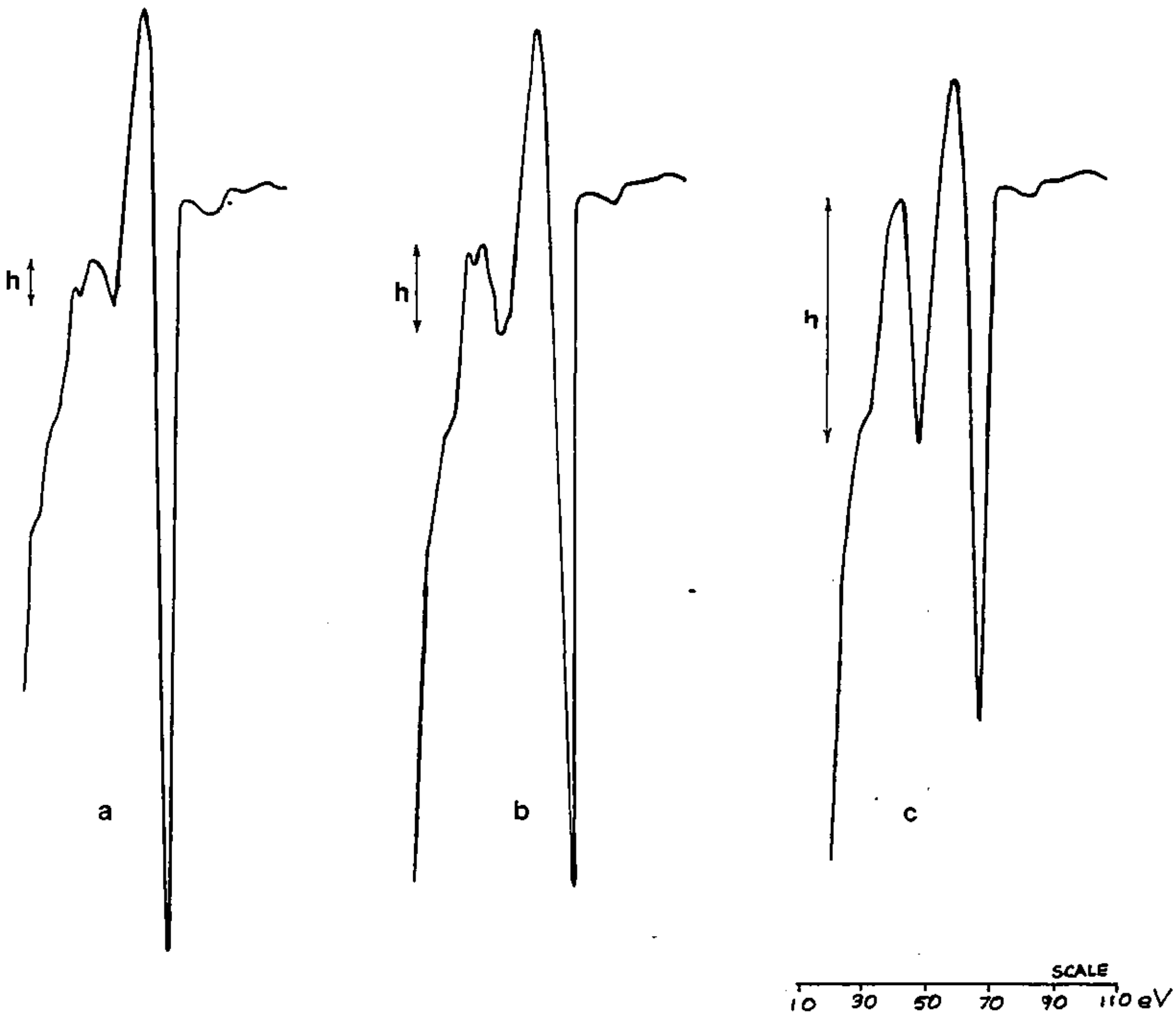

Figure 4.11: Auger signals at various Cs coverages. (a) is the clean Al 68eV (LVV) $\frac{dN}{dE}$ Auger signal (E_p = 1KeV) and (b) and (c) are the $\frac{dN}{dE}$ Auger signals corresponding to Cs exposure times 90 and 300 secs respectively (see figure 4.10). As the Cs 49eV ($N_5O_3O_3$) Auger feature coincides with the Al Auger features the height h was taken as a measure of the Cs Auger intensity which explains the deviation from linearity of the Cs curve near the origin of figure 4.10.

transition should be used to avoid this difficulty. This transition, however, is much less intense than the low energy transition and was too weak to be used to calibrate the coverage (as has been found by others, ref:- 11).

Apart from the deviation from linearity near the origin the peak to peak height of the caesium Auger feature grows with increasing exposure time until it reaches a saturation level - the plateau in figure 4.10. The aluminium Auger signal displays complementary behaviour: a linear attenuation with increasing Cs coverage and then a slightly less well defined plateau (probably due to a build-up of residual contamination, see Chapter 3) when the Cs signal has saturated. It is reasonable to assume that the plateaus in the Auger signal curves occur when the caesium coverage has saturated at one full monolayer and from the corresponding diffraction pattern shown in photo j a structural model can be calculated:

Figure 4.12 shows a scale diagram of photo j and the reciprocal lattice vectors that are used to construct the real space lattice.

Figure 4.13 shows the hard ball model of the proposed saturated monolayer structure. The size of the caesium atoms turns out to be 5.4 ± 0.1 A, which agrees well with the metallic size of 5.30 A (ref:- 3). As can be seen from the diagram Cs forms an incommensurate hexagonal close packed structure at saturation coverage. The orientation of this structure is the same orientation as the $(\sqrt{3} \times \sqrt{3})R30°$ structures that potassium and sodium atoms form on the Al(111) surface. The larger size of the Cs atoms prevents the final contraction required for complete registry. From this

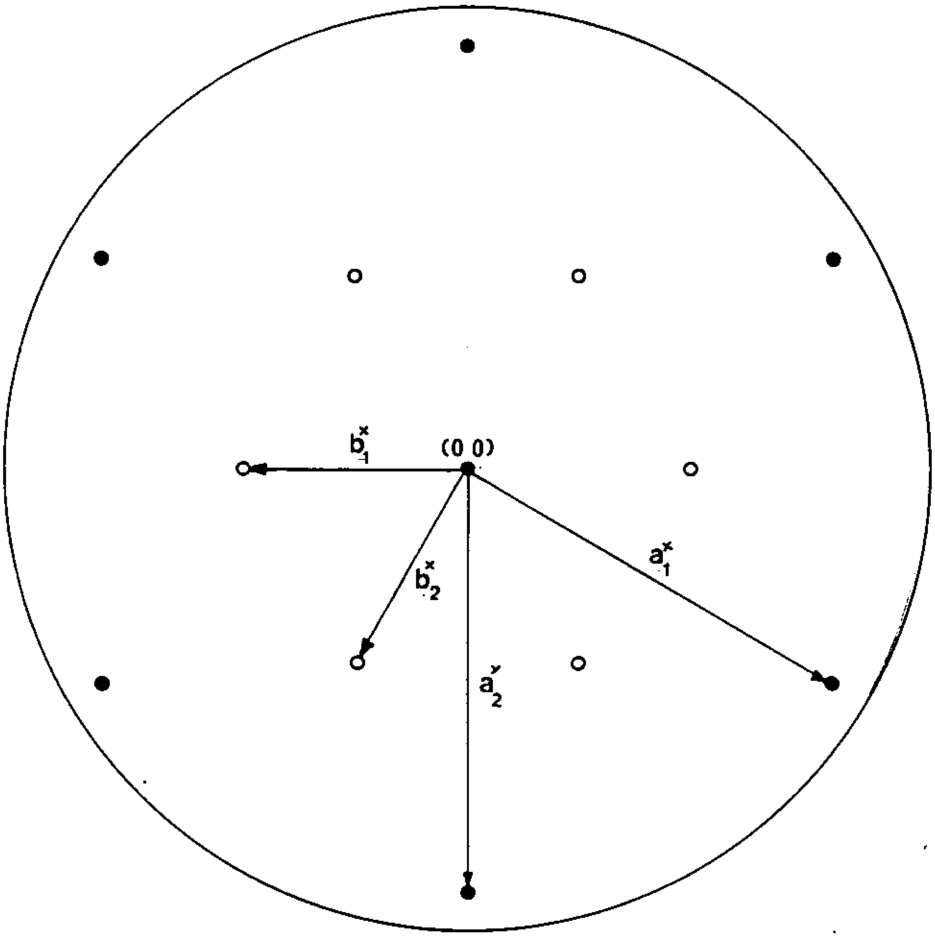

$a^*_{1,2}$ are the reciprocal lattice vectors of the Al(111) surface

$|a^*_1| = |a^*_2| = 2\pi\left(2{\cdot}86\,\text{Å}\right)^{-1}$

$b^*_{1,2}$ are the reciprocal lattice vectors of the Cs superstructure

$|b^*_1| = |b^*_2| = 2\pi\left(5{\cdot}4 \pm 0{\cdot}1\,\text{Å}\right)^{-1}$

Figure 4.12: A scale diagram of photo j showing substrate diffraction beams (●) and the diffraction beam (o) from the Cs overlayer.

The diffuse lines due to disorder have been omitted from this diagram.

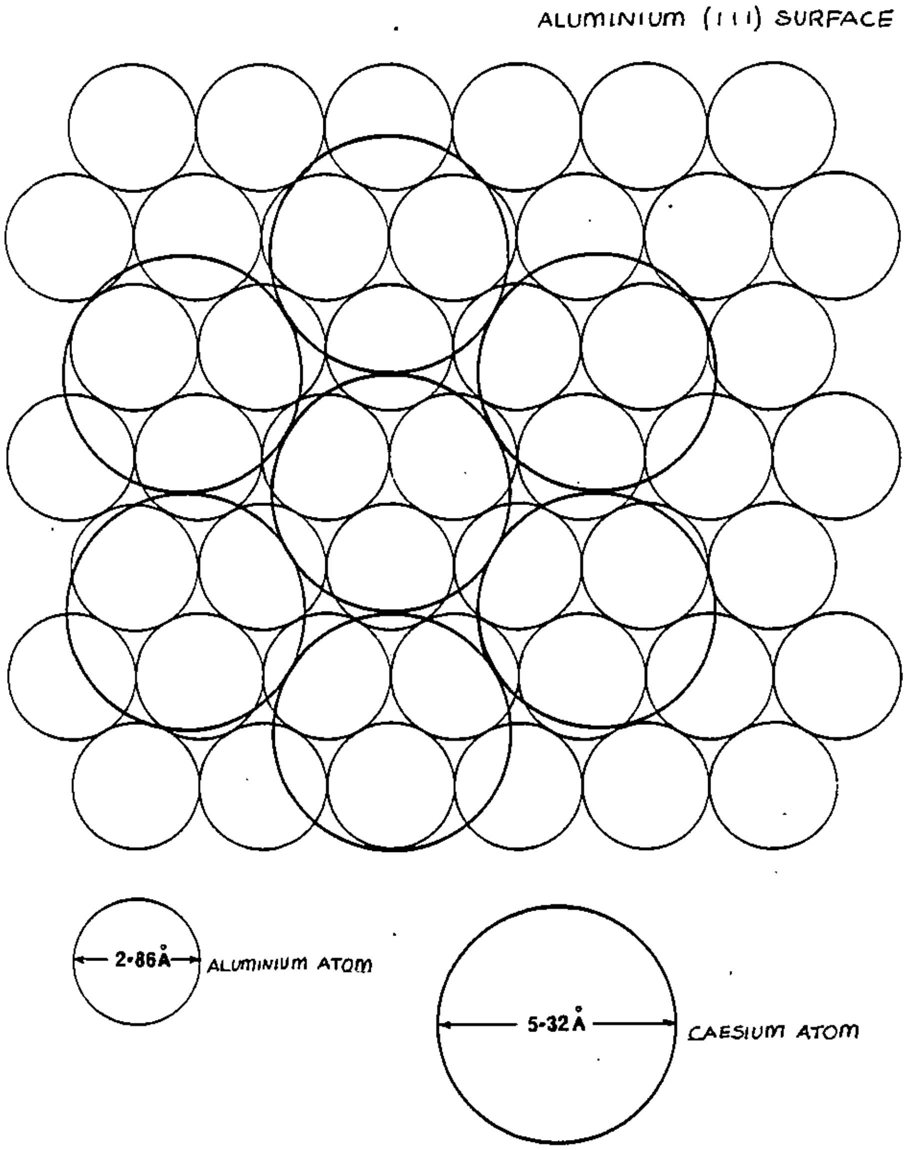

Figure 4.13: Hard ball model showing the incommensurate hexagonal close packed structure that Cs forms on the Al(111) surface at saturation coverage.

structural model the saturation caesium coverage on the Al(111) surface was calculated to be 3.95 ± 0.15 x 10^{14} atoms cm^{-2} (θ = 0.28 ± 0.01). Working back from this coverage and using figure 4.10, the Cs coverages corresponding to photos g, h, j are <u>approximately</u> $\theta \approx$ 0.16; 0.19; 0.21 respectively. The first, barely observable new diffraction feature was found to occur at $\theta \approx$ 0.14.

4.4 <u>Crystal current to earth measurements</u>

Figures 4.14 and 4.15 show the changes in the crystal current to earth measurements that were recorded simultaneously with the Auger data of figures 4.3 and 4.10. As can be seen, these $i_{cc}(t)$ curves are similar and so will be discussed together.

Initially, i_{cc} increases with increasing alkali metal coverage. At some submonolayer coverage, however, i_{cc} reaches a minimum value and then falls and eventually levels off at a constant value. The position of the onset of the plateaus in each curve corresponds very closely with the plateaus in the Auger data and so the alkali metal coverage at these points will also be defined as a full monolayer.

Even though the origin of these crystal current fluctuations is not yet understood (see Chapter 5), figures 4.14 and 4.15 were extremely reproducible. In particular, the alkali metal induced diffraction features (i.e. spots or "streaky spots") were always first observable just past the maximum in the i_{cc} curves and teh corresponding structures became fully developed by the onset of the plateau. The most noticeable difference between figures 4.14 and 4.15 is that for caesium adsorption a small hump or shoulder is observed just before the plateau. This feature occurs at the coverage where the LEED patterns imply that the structure of the Cs overlayer is quite complicated.

Because the Auger data implies that the alkali metal coverage

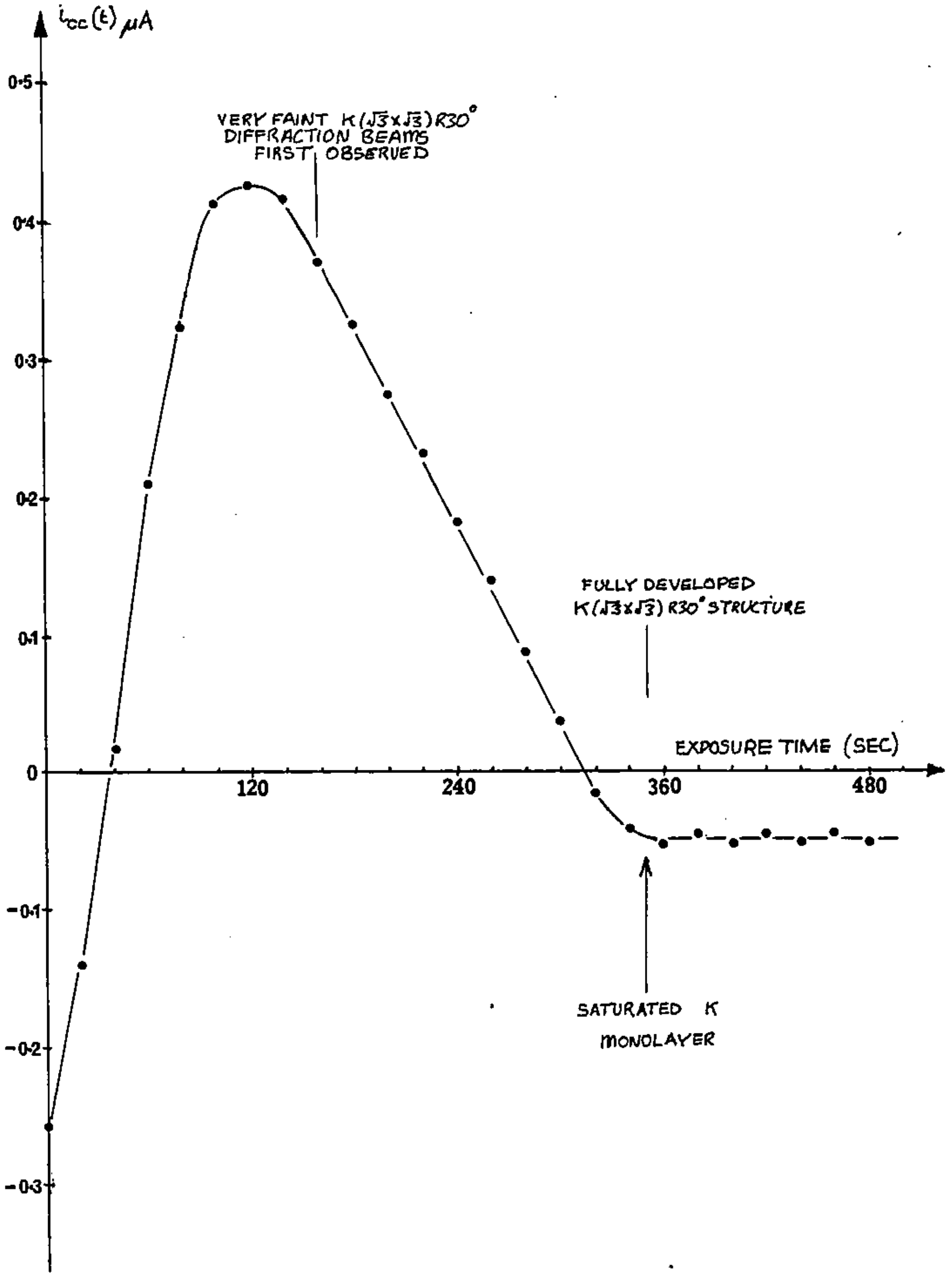

Figure 4.14: The variation of the total crystal current to earth, i_{cc} (t) , (at fixed primary beam energy, 260 eV, and emission current 2μ Amps) as a function of potassium exposure time. The data was collected simultaneously with the AES data of figure 4.3.

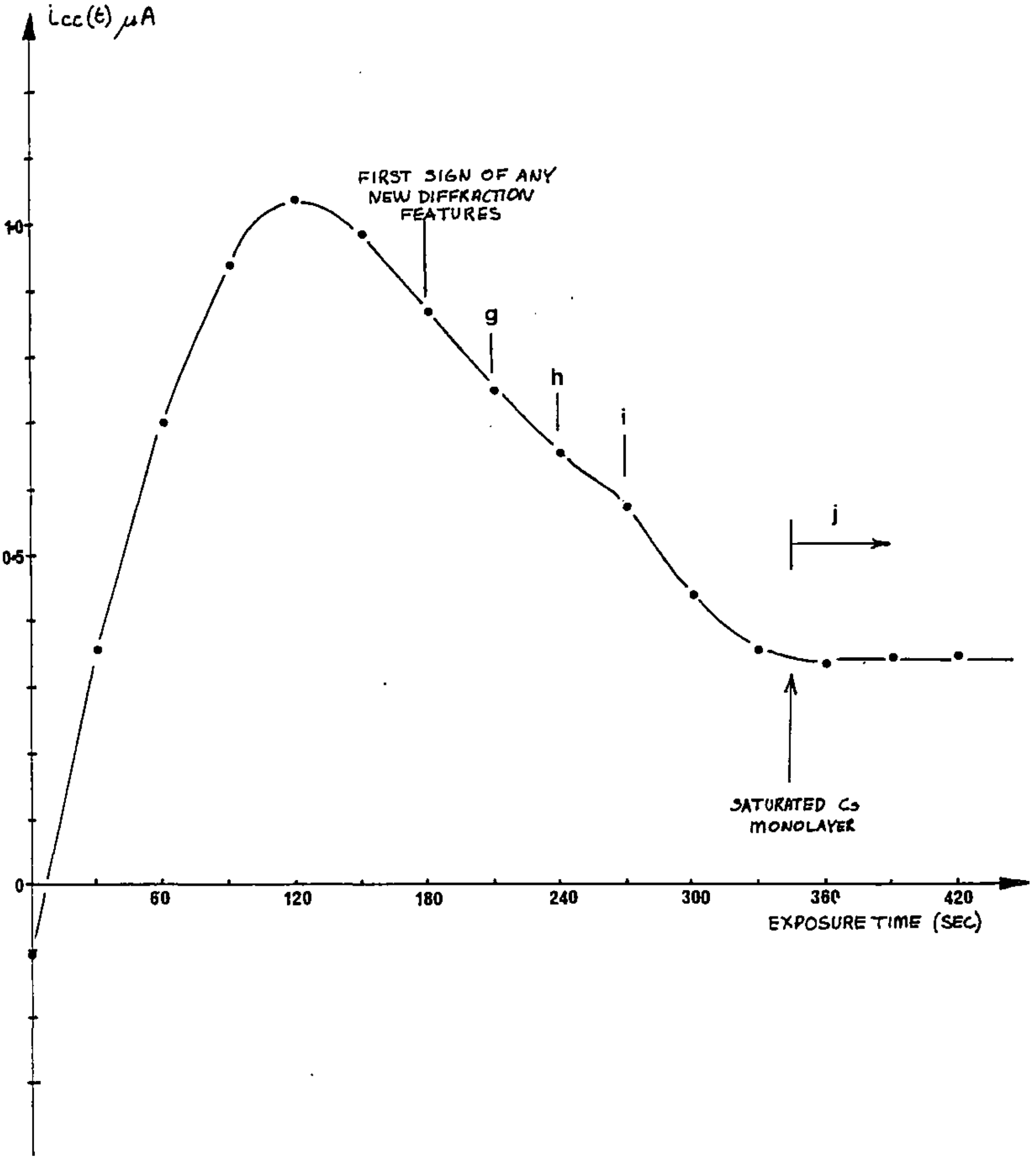

Figure 4.15: The variation of the total crystal current to earth, $i_{cc}(t)$ (at fixed primary beam energy, 260 eV, and emission current 2µ Amps) as a function of caesium exposure. This data was collected simultaneously with the AES data of figure 4.10. The letters correspond to the photographs of figure 4.8.

increases approximately linearly up to the beginning of these plateaus, in Chapter 5 submonolayer coverages will be deduced from the exposure time required to produce them.

4.5 Summary of the LEED results for K and Cs on Al(111)

When potassium is adsorbed on Al(111) the same sequence of diffraction patterns is seen as PORTEUS saw for sodium adsorption on Al(111), i.e. a LEED pattern ascribed to a $(\sqrt{3} \times \sqrt{3})R30°$ superstructure is observed, and then on continued exposure a LEED pattern of the same symmetry as that produced by a p(2x2) superstructure is observed. Again, no diffraction spot movement is seen, and so the potassium adlayer appears to grow in islands - which is not expected from what is observed for alkali metal adsorption on transition metals. However, in the case of potassium, the changes that occur after the formation of the K $(\sqrt{3} \times \sqrt{3})R30°$ structure do not appear to be accompanied by an expected increase in potassium coverage as assessed by A.E.S. In addition to this, PORTEUS' structured model for the final diffraction pattern, 3 domains of p(2x1) would require an unusually large contraction in the size of the adsorbed atoms.

It is suggested that residual contamination may be responsible for the final structures although it is pointed out that other phenomena, such as unexpected surface alloying, could also produce the observed behaviour.

The K $(\sqrt{3} \times \sqrt{3})R30°$ structure was therefore defined as a monolayer $\theta_K = 0.33$ $(4.7 \times 10^{14}$ atoms $cm^{-2})$ which is consistent with the AES data and a hard-sphere model.

When caesium is adsorbed on Al(111) an expanding hexagonal array of spots is observed as the coverage is increased from $\theta_{Cs} = 0$. Cs adsorption on Al(111) therefore displays trends more typical of alkali metal adsorption on other metals. At saturation coverage an incommensurate hexagonal close packed structure is formed and the coverage is deduced to be $\theta_{Cs} \simeq 0.28 \pm 0.01$ ($3.95 \pm 0.15 \times 10^{14}$ atoms cm^{-2}).

The $(\sqrt{3} \times \sqrt{3})R30°$ structure that potassium and sodium (- PORTEUS) form on Al(111) demonstrate that the periodicity of this substrate has a strong influence on the ordering of the overlayers. $(\sqrt{3} \times \sqrt{3})R30°$ structures have also been seen for iodine adsorbed on Ag(111) (ref:- 12) where full LEED analysis has shown that the subsurface structure of the substrate influences the adsorption site.

The structures that caesium forms on Al(111) also appear to be influenced by the periodicity of the substrate and even though an incommensurate structure is observed at saturation coverage, the Al(111) surface still has a strong orientational effect on the overlayers at all coverages. It is probable that it is the lateral strain introduced into the adlayer by this effect that causes the observed disorder saturation coverage.

Therefore LEED observation of K, Cs and Na (- PORTEUS) show that the Al(111) substrate appears to have a much greater influence on the adlayers than would be expected from the calculated surface migration energies (table 1.3, Chapter 1) which imply that the alkali metals ought to be highly mobile on the aluminium (111) surface and at room temperature.

REFERENCES

1. Auger Catalogue by W.A. COGHLAN and R.E. CLAUSING (ACADEMIC PRESS NEW YORK 1973)
2. A.P. JANSSEN, Surface Sci. 52 (1975) p.230
3. Laue Atlas, EDUARD PREUSS, BERNHARD KRAHL-URBAN RAINER BUTZ. Ed. by KERNFORSCHUNGSANLAGE JÜLICH (J. WILEY & SONS NEW YORK 1974)
4. G. PIRUG, H.P. BONZEL and G. BRODEN, Surface Science 122 (1982) p.1
5. E.L. GARFUNKEL and G.A. SOMORJAI, Surface Science 115 (1982) p.441
6. G.E. RHEAD, M-G. BARTHES and C. ARGILE, Thin Solid Films 82 (1981) p.201
7. Constitution of Binary Alloys by M. HANSEN and K. ANDERKO (McGRAW-HILL NEW YORK 1958)
8. N.J. TAYLOR, Surface Sci. 4 (1966) p.161
9. K.D. GRONWALD and M. HENZLER, Surface Sci. 117 (1982) p.180
10. P. DELESCLUSE and A. MASSON, Surface Sci. 100 (1980) p.423
11. S. THOMAS and T.W. HAAS, J. Vac. Sci. Technol. Vol. 10 No. 1 p.218 (1973)
12. F. FORSTMANN, W. BERNDT and P. BÜTTNER, Phys. Rev. Letts. Vol. 30 No. 1 p.17 (1973).

CHAPTER 5

WORK FUNCTION AND CORE LEVEL EXCITATION THRESHOLD STUDIES OF K AND Cs ADSORBED ON Al(111)

Introduction

In the first section of this chapter the work function/coverage curves of K and Cs adsorbed on Al(111) are presented and compared. This section is followed by a discussion of the use of core level excitation thresholds, measured by EELS, as a means of probing the charge state of an adsorbate. The EELS data for K on Al(111) and for Cs on Al(111) are then discussed. These sections are followed by a short section on plasmon losses and finally by a section on the crystal current measurements.

5.1 Work function change for potassium and caesium adsorption on aluminium (111)

Figures 5.1 and 5.2 show the change in the work function that occurs when potassium and caesium are adsorbed onto a clean aluminium (111) surface. The coverage axes are determined by the onset plateaus in the corresponding $i_{cc}(t)$ curves since A.E.S. studies indicate that the alkali coverage increases approximately linearly with exposure time up to these points (see Chapter 4). On comparing these work function/coverage curves we see that there are fundamental differences.

For potassium adsorption the work function falls approximately linearly with coverage to reach its final value corresponding to $\Delta\phi$ -2.2eV by about $\theta_K \approx 0.15$. At approximately the same coverage the $(\sqrt{3} \times \sqrt{3})R30°$ diffraction beams appear and grow in intensity during the

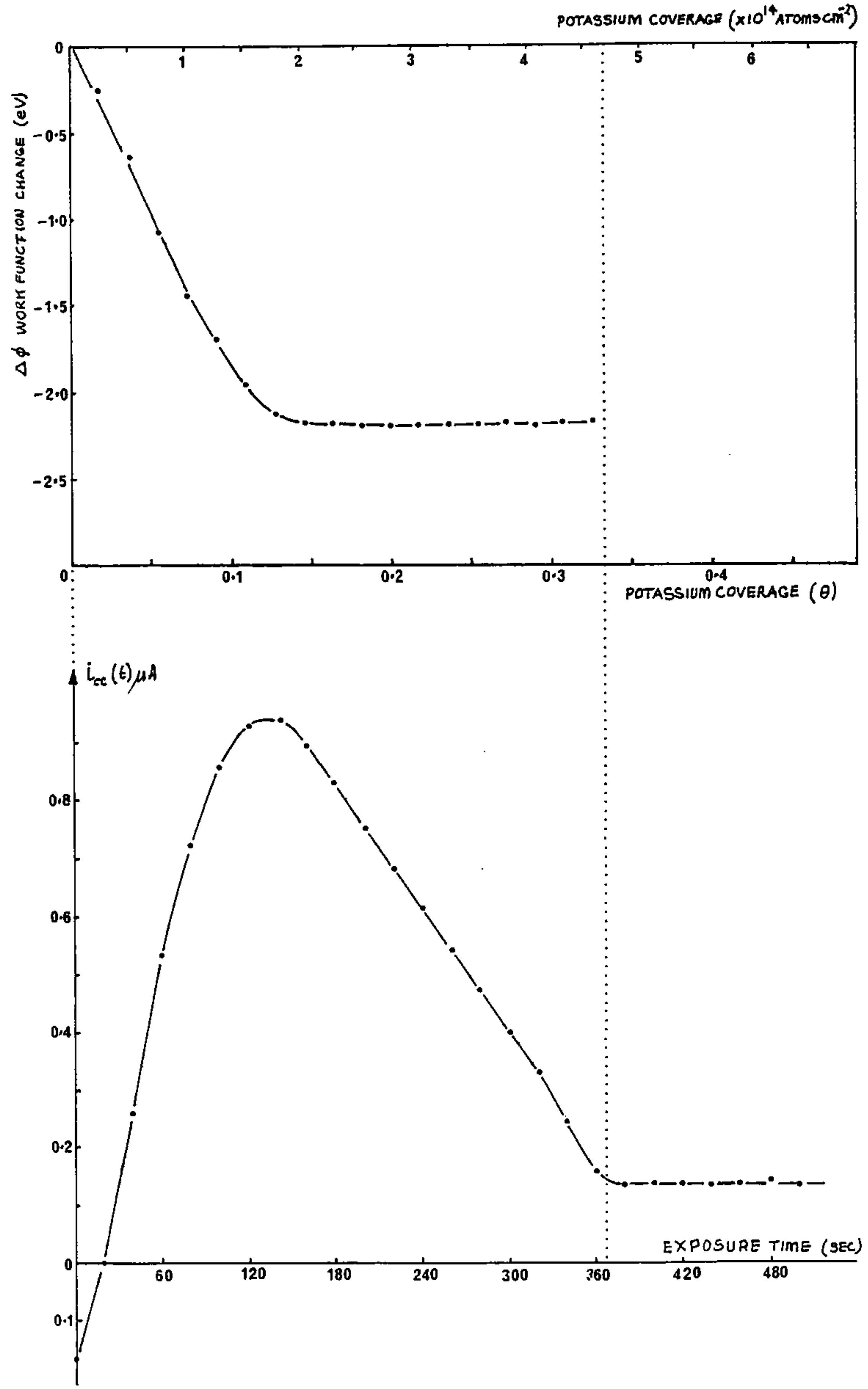

Figure 5.1: (top) Work function change as a function of potassium coverage on Al(111); (bottom) The accompanying crystal current measurements.

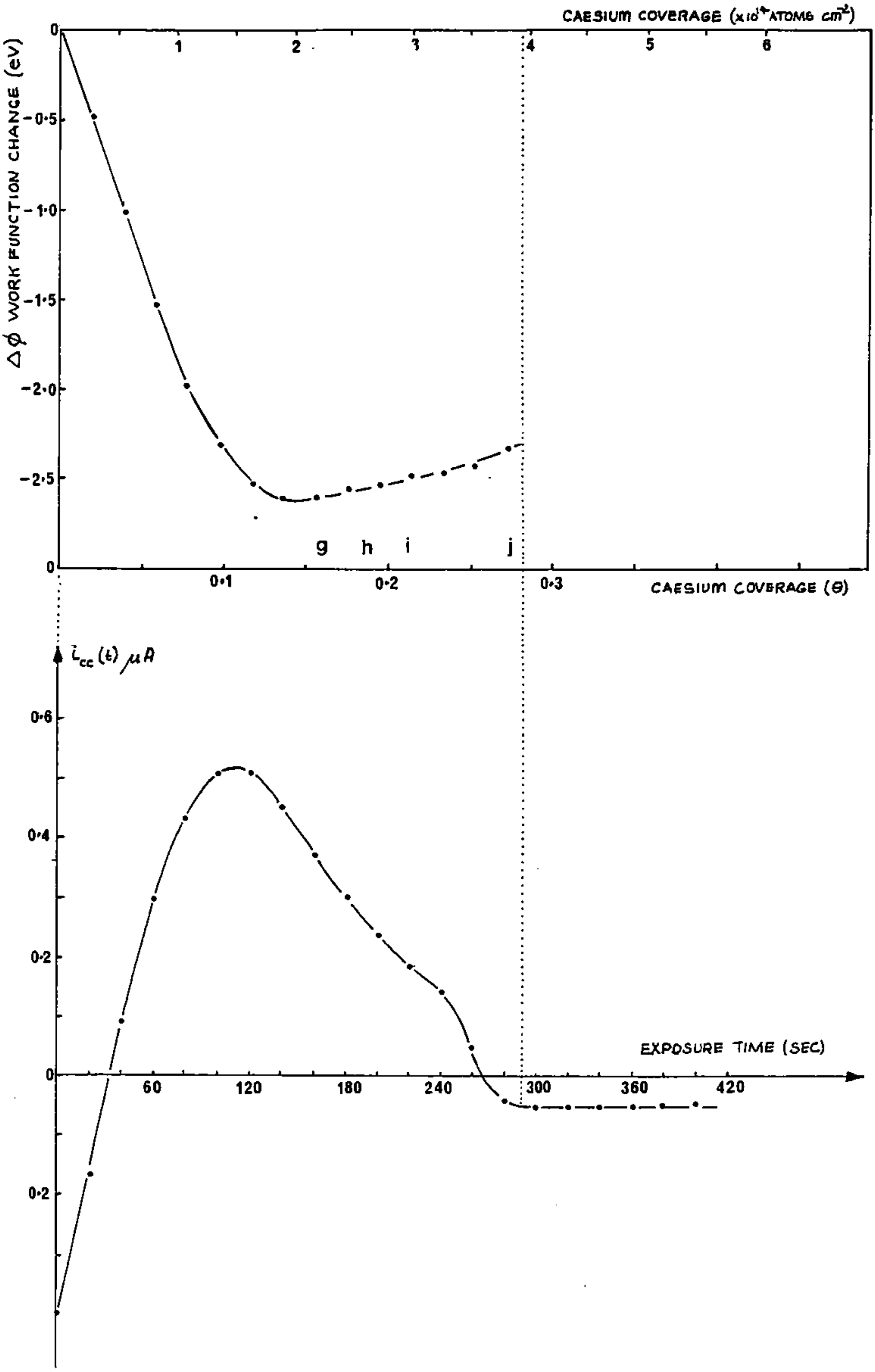

<u>Figure 5.2</u>: (top) Work function change as a function of caesium coverage on Al(111);
(bottom) The accompanying crystal current measurements.

completion of the monolayer. No significant change in the work function occurs from then on, even during the long exposure times required to produce the final diffraction pattern (photo d). The work function does not pass through a minimum and is similar to the curves of PORTEUS for Na on Al(111) and Al(100). See figure 2.2.

When caesium is adsorbed onto the clean aluminium (111) surface, however, the work function passes through a distinct minimum at $\theta_{Cs} \approx 0.14$ corresponding to $\Delta \phi \approx -2.6$eV and then rises to $\Delta\phi = -2.3$eV at full monolayer coverage. The letters on figure 5.2 correspond to the LEED photograph of figure 4.8. Continued exposure leads to no further changes in work function. Caesium behaves just as we would expect an alkali metal to behave on adsorption according to the theories outlined in Chapter 1 and the bulk of the experimental data summarised in Chapter 2.

If we assume that the work function of the aluminium (111) surface of 4.24eV (ref:- 1), then the work functions of potassium and caesium at monolayer coverage is 2.04 and 1.94eV respectively. Both of these values are slightly <u>lower</u> than the corresponding bulk values of 2.30 and 2.14 (refs:- 2,3). The measurement techniques used in this study, however, only measure differences in work function and so the substrate work function may be slightly less than 4.24eV, possibly due to surface roughness.

Using equation 1 and the work function data of figures 5.1 and 5.2, the dipole moments as a function of alkali metal coverage can be calculated. These are shown in figure 5.3 as well as the theoretically predicted values of KAHN and YING from table 1.2 (Chapter 1). Both sets of experimental

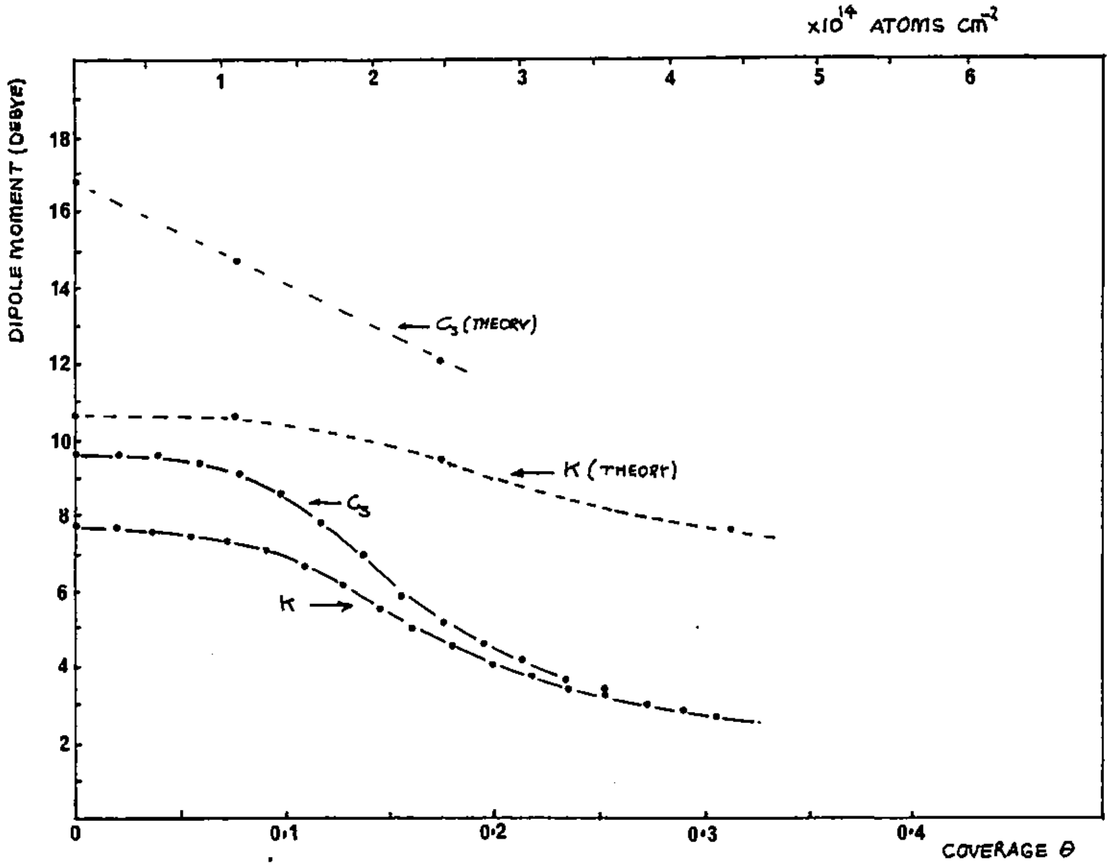

Figure 5.3: Dipole moments of K and Cs calculated from figures 5.1 and 5.2 using equation 1 compared with the theoretical values to KAHN and YING (table 1.1). Both sets of experimental data are below the theoretical curves. For K, where island growth is suspected, it is doubtful whether this type of analysis is valid (see text). For Cs, where LEED and core level excitation threshold measurements (see section 5.2.3) imply a coverage dependent charge transfer, the disagreement with theory may be due to the failure of the latter to take into account the periodicity of the Al (111) substrate. It is worth pointing out that this (often used) way of presenting the data conceals the shape of the work function/coverage curve (compare figures 5.1 and 5.2).

data are consistently lower than the theoretical curves. The initial dipole moments are 7.7 ± 0.1 Debye for potassium and 9.6 ± 0.1 Debye for caesium. PORTEUS finds that the initial dipole moment for sodium on aluminium (111) is 6.8 ± 0.1 Debye which is in good agreement with the theoretical values of table 1.1

This agreement, however, appears coincidental. LEED studies imply that sodium and potassium atoms do not spread uniformly over the aluminium surface but form two dimensional islands which grow in size and eventually cover the surface at full monolayer coverage. Under these conditions equation 1 is no longer valid. Instead the work function change would be described (more accurately) by the average of the work function of the islands and the exposed substrate weighted by the alkali metal coverage. This would certainly give the observed trend in the work function variation with coverage.

5.2 Electron energy loss spectroscopy (EELS) of potassium and caesium adsorbed on aluminium (111)

ANDERSSON and JOSTELL (ref:- 4) have demonstrated how EELS can provide useful qualitative information about the charge transfer that accompanies the adsorption of alkali metals on (transition) metals. They used EELS to relate shifts in the alkali metal core level excitation thresholds to the 'chemical shifts' (Chapter 1) of the core levels that occur due to valence electron transfer.

In EELS the energy distribution of the electrons that are backscattered in, say, a LEED experiment is analysed and a curve as shown in figure 3.9 (Chapter 3) may be obtained. At zero energy loss there is a peak (A) which represents those primary electrons that have been elastically BRAGG reflected as well as those primary electrons which have been incoherently, although elastically, backscattered. This 'elastic peak' will often be followed by one or more prominent losses (B: figure 3.9) which occur when primary electrons lose discrete amounts of energy by exciting plasma oscillations in the conduction band of the sample. There are two types of plasma oscillations: bulk plasmons and surface plasmons. The energy of the bulk plasmons is $\hbar\bar{\omega}_p$ where $\bar{\omega}_p$ is the plasmon frequency. This frequency is given by $\epsilon(\omega) \simeq 0$ where $\epsilon(\omega)$ is the dielectric function of the solid. For a free electron gas with no plasmon damping the dielectric function is

$$\epsilon(\omega) = 1 - \frac{ne^2}{m\epsilon_0\omega^2} = 1 - \frac{\omega_p^2}{\omega^2}$$

(e.g. ref:- 5) where n = conduction band electron density, m = mass of electrons, -e is its charge and ϵ_0 is the permittivity of free space.

Therefore,

$$\epsilon(\omega) = 0 \Rightarrow \bar{\omega}_p = \omega_p = \sqrt{\frac{ne^2}{m\epsilon_0}}$$

For real solids the band structure determines the lifetime of the plasmons, i.e. the damping, and this has the effect of reducing the plasmon frequency, i.e. (ref:- 6).

The energy of the surface plasmon is $h\omega_s$ where is the surface plasmon frequency and is related to the bulk plasmon frequency by $\omega_s = \frac{\bar{\omega}_p}{\sqrt{1+\epsilon^*}}$. ϵ^* is the relative permittivity of the medium outside the surface and in a U.H.V. experiment ϵ^* is unity, so that $\omega_s = \frac{\bar{\omega}_p}{\sqrt{2}}$.

Plasmons are collective excitations since they involve a large number of electrons. Single particle excitations are also possible and occur when the incident electrons excite valence or core electrons into empty states above the Fermi level. To excite core electrons a certain minimum or 'threshold' energy is required - the binding energy of the core electron relative to the Fermi level - and so core level excitation thresholds occur at well defined loss energies in EEL spectra.

Figure 5.4 shows the details of how the energy loss of the backscattered incident electrons can be used to probe the core levels. An incident electron can lose: (a) all of its energy, (b) part of its energy, or (c) lose just the minimum threshold energy in exciting the core electron. Figure 5.4 shows that (a) and (c) are equivalent processes (ref:- 7) and in between them all combinations (e.g. b) of final energies of the initial and excited core electrons, which are consistent with Pauli's exclusion principle and conservation of energy are possible. The probability of a given combination of final energies is proportional to the joint density of dates (D.O.S.) for the two energies. Since the one electron D.O.S. is a slowly varying function of energy for states well above the Fermi level, core level excitations give rise to thresholds where shape near the edge is proportional to the conduction band D.O.S. For alkali metals a weak threshold is expected as the D.O.S., even in the vicinity of the Fermi level, is thought to be nearly-free-electron metal-like.

If relaxation effects are small (Chapter 1), shifts in the alkali metal core level excitation threshold as a function

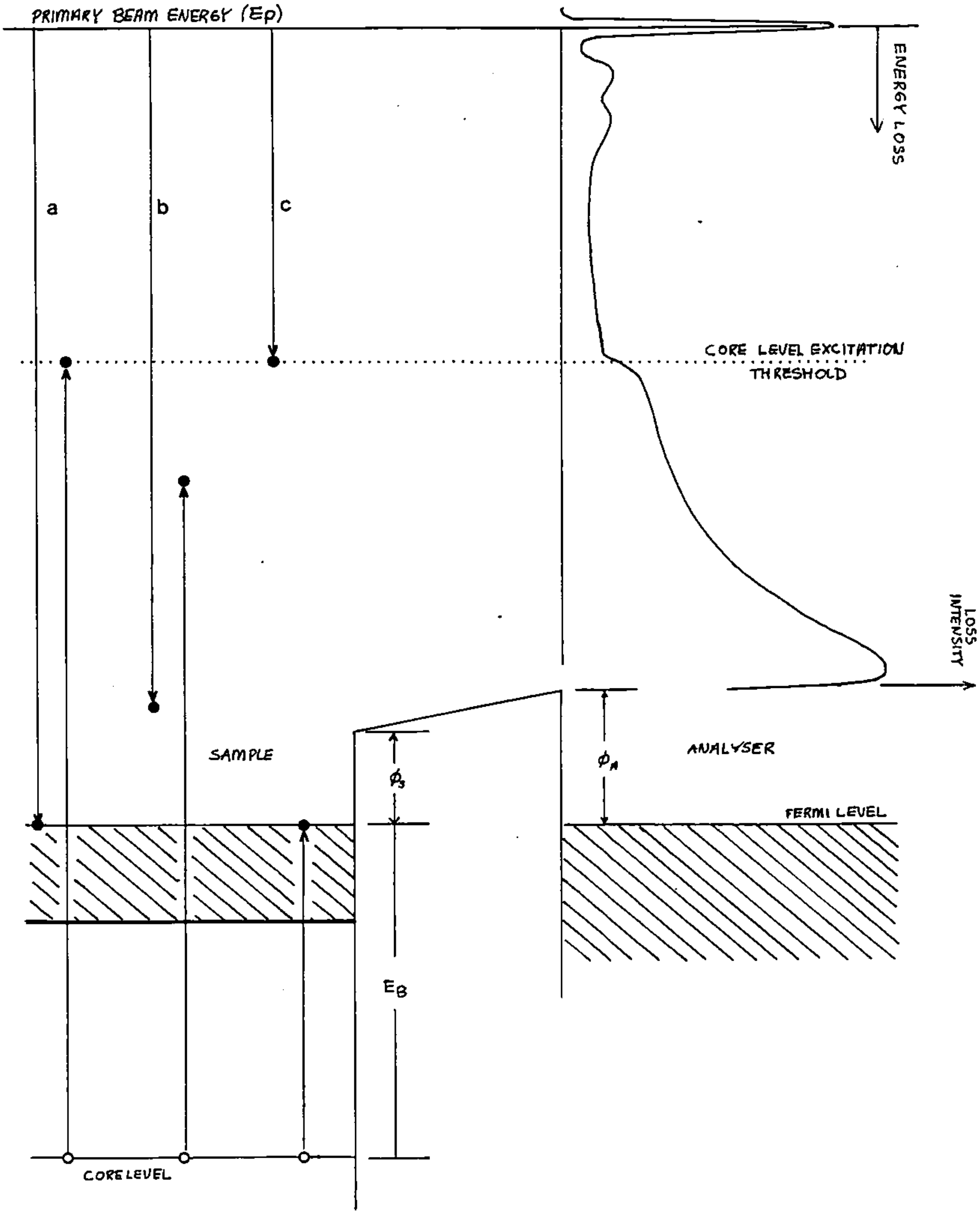

<u>Figure 5.4</u>: Energy level diagram showing how core level excitation thresholds can be measured using EELS. The binding energy of the core level relative to the fermi level is E_B.

of coverage will reflect the chemical shifts due to charge transfer and so the depolarisation of the adlayer can be studied.

The core hole left by the excitation, however, can be filled by an Auger transition (ref:- 8). In this process an electron from a higher energy level fills the 'hole' and the energy released by this transition is given to a third electron which may then escape from the solid. The energy of this electron is dependent only on the particular transition and on the Fermi level of the solid, and so Auger features are 'emission processes' and do not occur at constant loss energy.

5.2.1 EELS study of the 3p core level excitation threshold of potassium adsorbed on aluminium (111)

For potassium, the highest energy core levels are the 3p levels. U.P.S. meaasurements (where the energy distribution of the ejected electrons is not influenced by the D.O.S. just above the Fermi level) imply that these levels are about 18.7eV below the Fermi level (ref:- 9). In fact, the 3p levels are spin-orbit split into a doublet: $3p_{3/2\ 1/2}$. This splitting is very small, however, $\sim$ 0.6eV (ref:- 9) and so it will be neglected in what follows. Normal incidence angle integrated EELS experiments, using the LEED optics as a retarding field analyser in the N(E) mode, were therefore performed to look for and study losses of this magnitude as potassium was adsorbed onto the aluminium (111) surface.

Figure 5.5 shows the changes that occur in the energy loss spectra as the potassium coverage is increased from $\theta = 0$. (The coverage was deduced from the exposure time required to produce a plateau in the i_{cc} curve). The primary beam energy ($\approx$ 40eV) was chosen so that the loss due to the

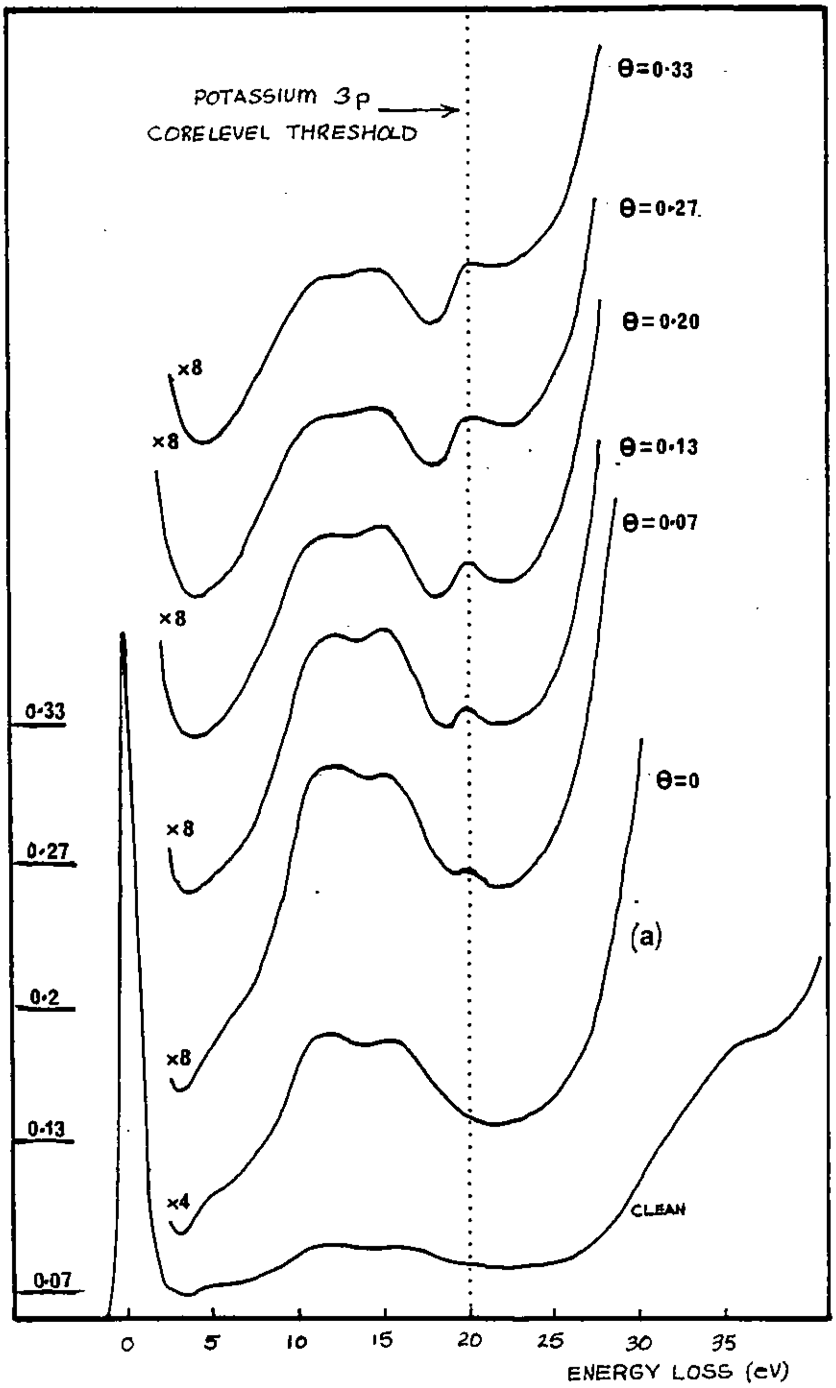

Figure 5.5: Normal incidence angle integration of energy loss spectra (primary beam energy = 40eV) showing the potassium 3p core level excitation threshold at various potassium coverages.

expected K 3p threshold would appear at a (kinetic) energy where the background electron distribution from clean aluminium is flat and free from structure. See curve (a). As can be seen, a feature at an energy loss of 20.0eV appears and grows in intensity with increasing coverage. This feature is ascribed to the potassium 3p cover level excitation threshold - however, it has an unexpected 'peak-like' shape and remains at constant loss energy as the potassium coverage increases.

Figure 5.6 shows the results of a much higher resolution EELS study, at the same primary beam energy ($\approx$40eV) and confirms the 'peak-like' shape of the threshold and its apparent non-dependence on coverage. For reference, the primary electron beam profile is also shown in this figure.

As has been mentioned, care was taken to ensure that the K3p threshold loss would be superimposed on a constant background signal. If, however, a primary beam energy of $\approx$35eV was chosen, this feature could be superimposed on the sloping secondary electron cascade, where it then has a step-like shape. This is illustrated in figure 5.7. A bad choice of beam energy can therefore conceal the true shape of this feature.

In order to demonstrate that the shape of the potassium 3p threshold was not being influenced by the aluminium substrate, EELS studies were also performed on very thick potassium layers that could be deposited onto the crystal when it was cooled to liquid nitrogen temperature. Under these conditions sufficient potassium could be adsorbed to completely attenuate the 68eV aluminium Auger signal. Only potassium features could be seen in the Auger spectrum, and figure 5.8 shows these in detail. It was therefore considered

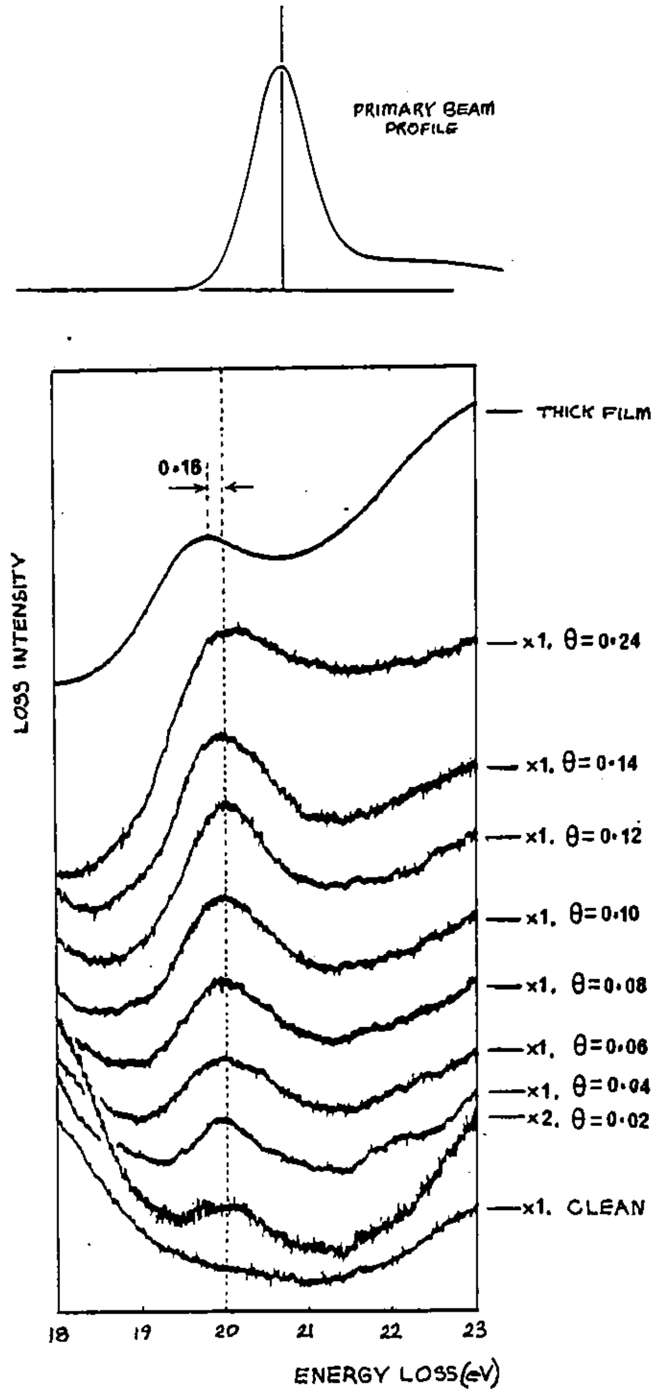

Figure 5.6: (bottom) High resolution normal incidence energy loss spectra (primary beam energy = 39.76) of the K 3p core level excitation threshold over the coverage range where the work function is falling rapidly (see figure 5.1); (top) The primary beam profile (corresponding to θ_K = 0.24) on the same energy scale and measured under the same conditions as the other spectra. For thick films depicted on a coded substrate a small shift of 0.16eV to lower loss energies is observed.

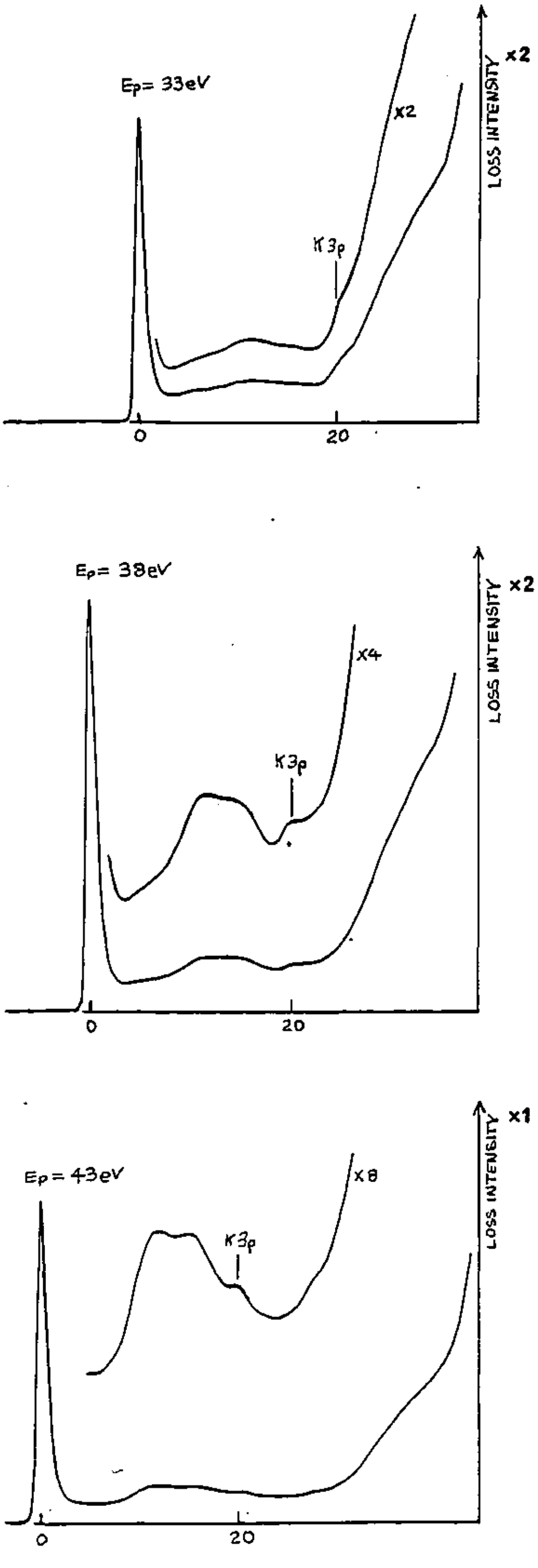

Figure 5.7: Normal incidence energy loss spectra for $\theta_K \approx 0.33$ demonstrating that for primary beam energies, $E_p < 38$eV, the K 3p core level excitation threshold is superimposed on the secondary electron cascade where its shape is obscured. For $E_p > 40$eV, the threshold is superimposed on a sloping background due to multiple substrate plasmon excitation.

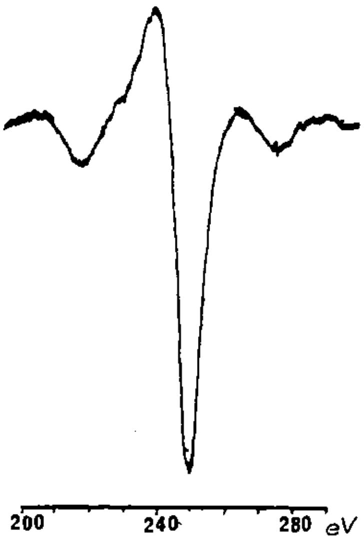

Figure 5.8: The potassium 251eV $(L_3M_{23}M_{23})$ $\frac{dN}{dE}$ Auger signal, from a thick film of K deposited onto the cooled Al(111) substrate (E_p = 1KeV)

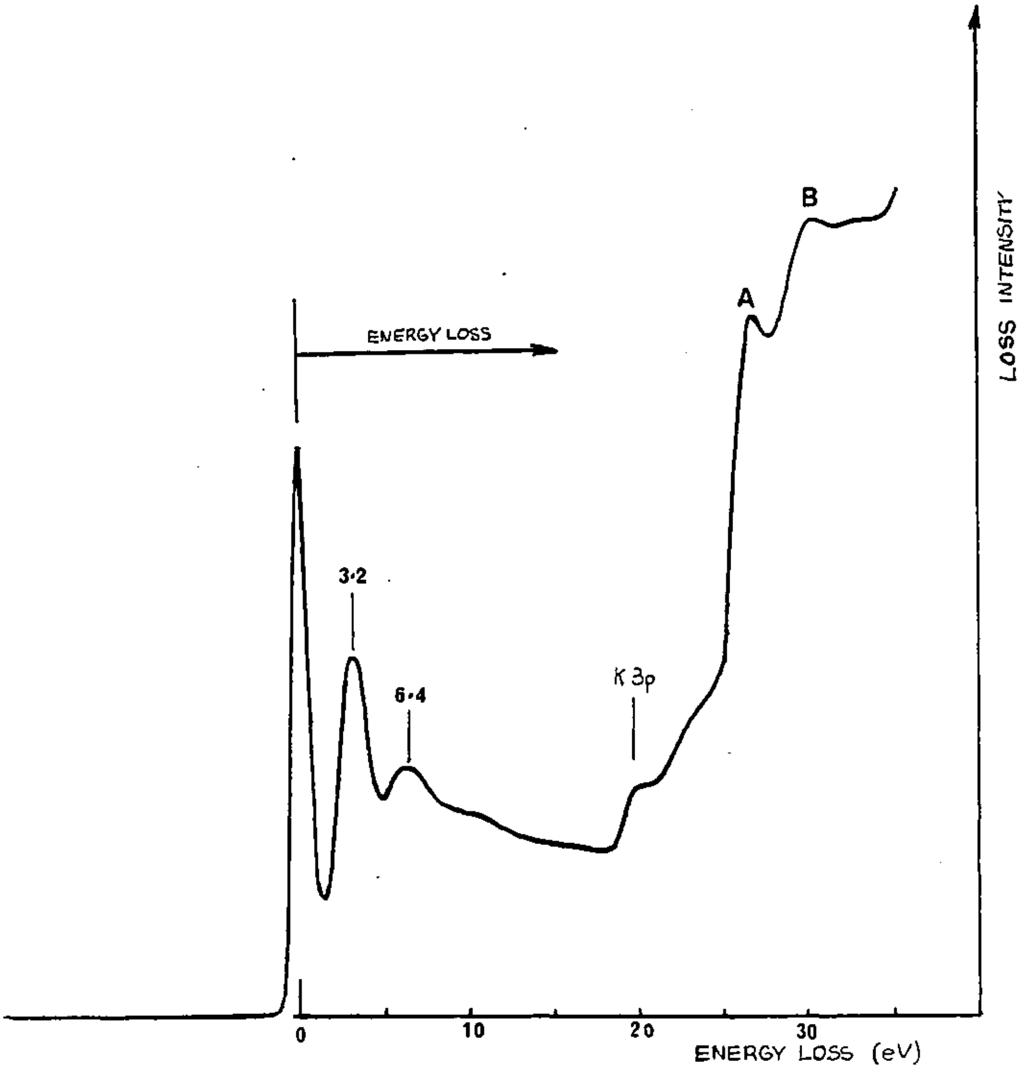

Figure 5.9: Normal incidence energy loss spectra primary beam energy = 39eV) from a thick film of potassium deposited onto the cooled Al(111) substrate.

that such layers would have the properties of bulk potassium. Figure 5.9 shows the whole EELS spectra from such a deposit. The multiple losses at low energies ($\approx$3;6.eV) are due to potassium plasmon losses and will be discussed in section 5.3 The feature marked A was found to be an Auger transition and occurs at a kinetic energy (with respect to the analyser) of $\approx$ 13eV. It is ascribed to the potassium $M_{23}VV$ Auger transition which is consistent with previous studies (ref:- 10) and calculated Auger data (ref:- 11). The feature marked B is believed to be due to those potassium $M_{23}VV$ Auger electrons which have lost energy in exciting plasmons. The potassium 3p threshold is also indicated in figure 5.9 and in greater detail in figure 5.6. It can be seen that the potassium 3p threshold loss from a thick layer of supposedly non-contaminated potassium also displays a peak at the threshold edge, although, compared with the other curves of figure 5.6, it occurs at a slightly smaller loss energy, i.e. a shift of 0.16eV is observed.

5.2.2 Discussion of the potassium 3p core level excitation threshold

These EELS measurements of the potassium 3p core level threshold are surprising because the simple theory outlined in the beginning of this section predicts that there should be a weak threshold and not a peak. A peak would require a very high DOS just above the Fermi level, such as is found for some transition metals.

Soft x-ray adsorption studies of alkali metal layers, however, also show unusual peak-like features at the 'p' core level excitation thresholds of all the alkali metals. Figure 5.10 shows the SXA spectra from references 12 and 13, and in the case of sodium (at least) it was verified that the structure

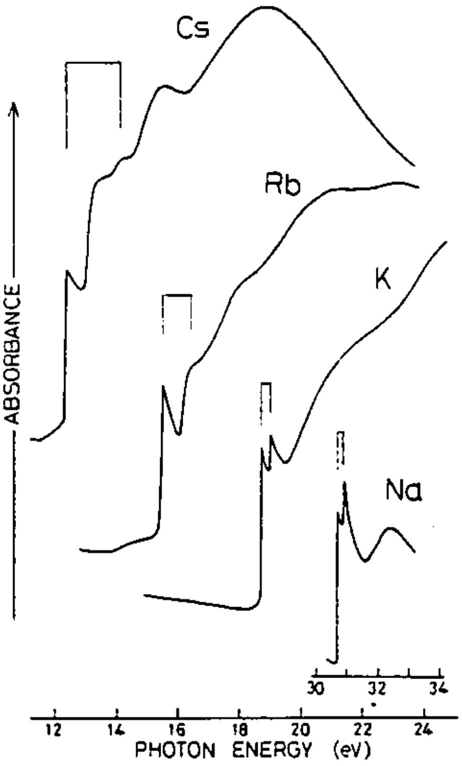

Figure 5.10: Soft x-ray adsorption spectra of outermost p-shell electrons in Na (ref:- 13) and K, Rb and Cs (ref:- 12)

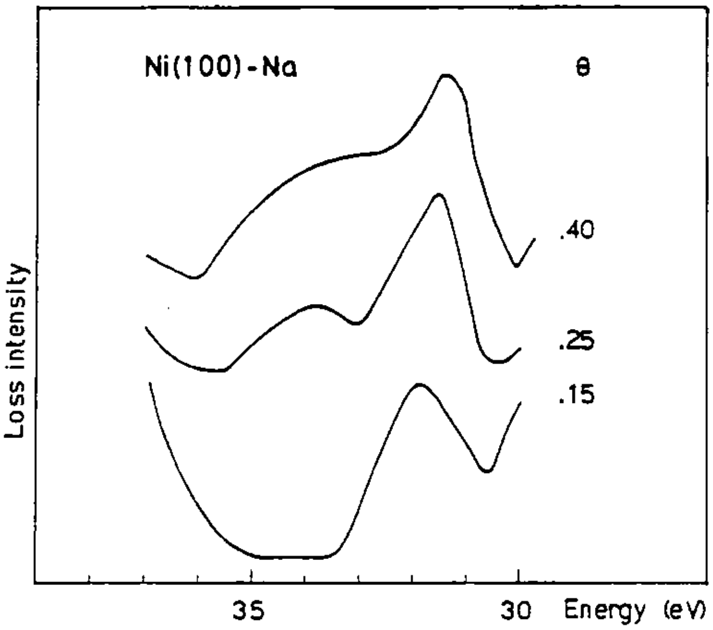

Figure 5.11: The Na 2p core level excitation threshold measured with EELS from reference 15.

at the threshold was not due to oxide formation (ref:- 13). The doublet at these thresholds is due to the spin orbit splitting of the p core levels: in this study the potassium $3P_{1/2}$ and $3P_{3/2}$ levels could not be resolved.

Much theoretical effort has been spent on explaining these "threshold singularities" and the theories depend heavily on many-body concepts. See review article by MAHAN (ref:- 14) and references in ref:- 12. It appears that the single particle picture of the absorption process is naive because it takes no account of the effect that the creation of the core hole has on the valence electrons. In Chapter 1 it was pointed out that relaxation effects can cause a shift in the core level binding energy - the sophisticated theories in the references above show that such effects can also change the shape of the threshold from that predicted by the one particle D.O.S. In the case of alkali metals, a peak or a "singularity" is expected at the p thresholds, whereas for other thresholds or material peaks may or may not be expected, depending on the transitions or material involved.

In ANDERSSON and JOSTELL's study fo the K3p excitation threshold a primary beam energy was used which meant that the threshold was superimposed on the sloping secondary electron cascade of the (nickel (100)) substrate and so it is not easy to deduce its real profile (ref:- 4). ANDERSSON and JOSTELL measured the shift of the inflection point in the leading edge of the K 3p threshold and showed that it varied from an energy loss of 19.9eV, in the low coverage limit, to an energy loss of 19.3eV at a complete potassium monolayer. This would imply a total binding energy decrease of 0.6eV, which is consistent with a reduction in charge transfer during the growth of the adlayer although it must be realized that the exact magnitude of the shift may also be influenced by relaxation effects.

ANDERSSON and JOSTELL's results are also consistent with the U.P.S. measurements of BRODEN and BONZEL, who study potassium adsorption on Fe(110) (ref:- 10). These workers see the potassium 3p binding energy change from 18.6 to 18.0eV during the growth of the first monolayer. Even though the absolute values are in poor agreement with ANDERSSON and JOSTELL's, (possibly due to the different techniques and analyses used), a binding energy decrease of ~0.6eV is again observed.

No shifts of this magnitude were, however, observed here for potassium adsorption on aluminium (111). Using ANDERSSON and JOSTELL's definition of the position of the 3p threshold, the inflection points in the leading edge of the spectra of figure 5.6 occur in the energy loss range of 19.0 → 19.5eV.

Although the shape of the K 3p threshold is not apparent from ANDERSSON and JOSTELL's work, JOSTELL (ref:- 15) has also studied the 2p threshold of Na adsorbed on nickel. The results of this study are reproduced in figure 5.11. We see immediately a very pronounced peak at the threshold, especially at low coverage. This peak, however, moves to lower binding energies as the sodium coverage increases, which is again consistent with a gradual depolarisation of the adlayer. JOSTELL ascribes this peak to the aforementioned threshold singularity.

More recently, workers using EELS to study alkali metal core level shifts on adsorption use the first derivative,

$\frac{dN}{dE}$ (as in A.E.S.) or even the second derivative, $\frac{d^2N}{dE^2}$ method of presenting their data (e.g. refs:- 16,17). The use of both of these methods of presenting the data, however, results in the loss of much information about the threshold profile and so it is not clear whether other workers have also seen 'peaks'. In fact, the $\frac{d^2N}{dE^2}$ method has been criticised (ref:- 18) since it can generate features which are not present in the true N(E) distribution. As a matter of interest, some workers using the $\frac{dN}{dE}$ representation have noted structure in the loss spectra of the core level thresholds at submonolayer coverages that does not appear to be due to spin-orbit splitting of the core level (e.g. Rb/Ni(100) (ref:- 15), Cs/Cu(111) (ref:- 19)).

Therefore, it is not known at this stage whether the peak seen at the K 3P threshold in this study (or the peak seen by JOSTELL at the Na2p threshold) is due to the "threshold singularity" or residual impurities which were undetected by AES. The important point is, however, that no shifts are observed in the K 3p core level threshold during the growth of the monolayer. A small but significant shift in the core level threshold of 0.16eV is observed when thick layers of K are deposited. It is not known whether this can be associated with a chemical shift or with a change in the relaxation energy. Because the core level thresholds at submonolayer coverages are nevertheless very close to the bulk value it would seem that the potassium adlayer is essentially neutral at all coverages, which is consistent with the LEED data and could account for the island growth.

5.2.3 EELS study of the 5p core level excitation threshold of caesium adsorbed on aluminium (111)

The energy loss study of the Cs5p core level threshold was complicated by the fact that it occurs at a loss energy ($\approx$12eV;

ref:- 19) which coincides with the surface and bulk plasmon losses of the aluminium substrate. The latter were found to occur at loss energies of 10.1 ± 0.1eV and 15.0 ± 0.1eV respectively. (These values agree very well with a list of values compiled in ref:- 6). The situation was found to be even worse for the Cs5s threshold ($\approx$27eV; ref:- 20) since at the primary beam energies required to excite it the multiple plasmon losses of the substrate dominate.

Therefore the Cs5p core level threshold was studied with a low primary beam energy, $\approx$34eV in the $\frac{dN}{dE}$ Auger mode (modulation at the LEED grid = $1V_{p-p}$) in the hope that some information could be extracted. The spectra are shown in figure 5.12 where, at zero coverage, the structure is due to the substrate plasmon losses. As caesium is adsorbed, two features marked A and B appear and shift towards smaller loss energies as the coverage increases. Both of these features are ascribed to the Cs5p threshold: the spin-orbit splitting of the Cs5p level is $\approx$ 2eV (ref:- 20,21), and so in this experiment the different levels are just resolvable (modulation = $1V_{p-p}$). Photoelectron emission experiments (ref:- 21) give the binding energies of the $Cs5p_{3/2}$ and $Cs5p_{1/2}$ core levels relative to the Fermi level as 11.4 and 13.1eV respectively. The feature B is therefore thought to be due to the $Cs5p_{3/2}$ core level threshold - unfortunately it is superimposed on the substrate surface plasmon structure and so it is easier to measure shifts in peak A - the $Cs5p_{1/2}$ threshold.

Figure 5.13 shows the shifts of the $Cs5p_{1/2}$ threshold as caesium coverage is increased from $\theta = 0$. This threshold moves from a loss of 14.9eV to a loss of 13.4eV over the

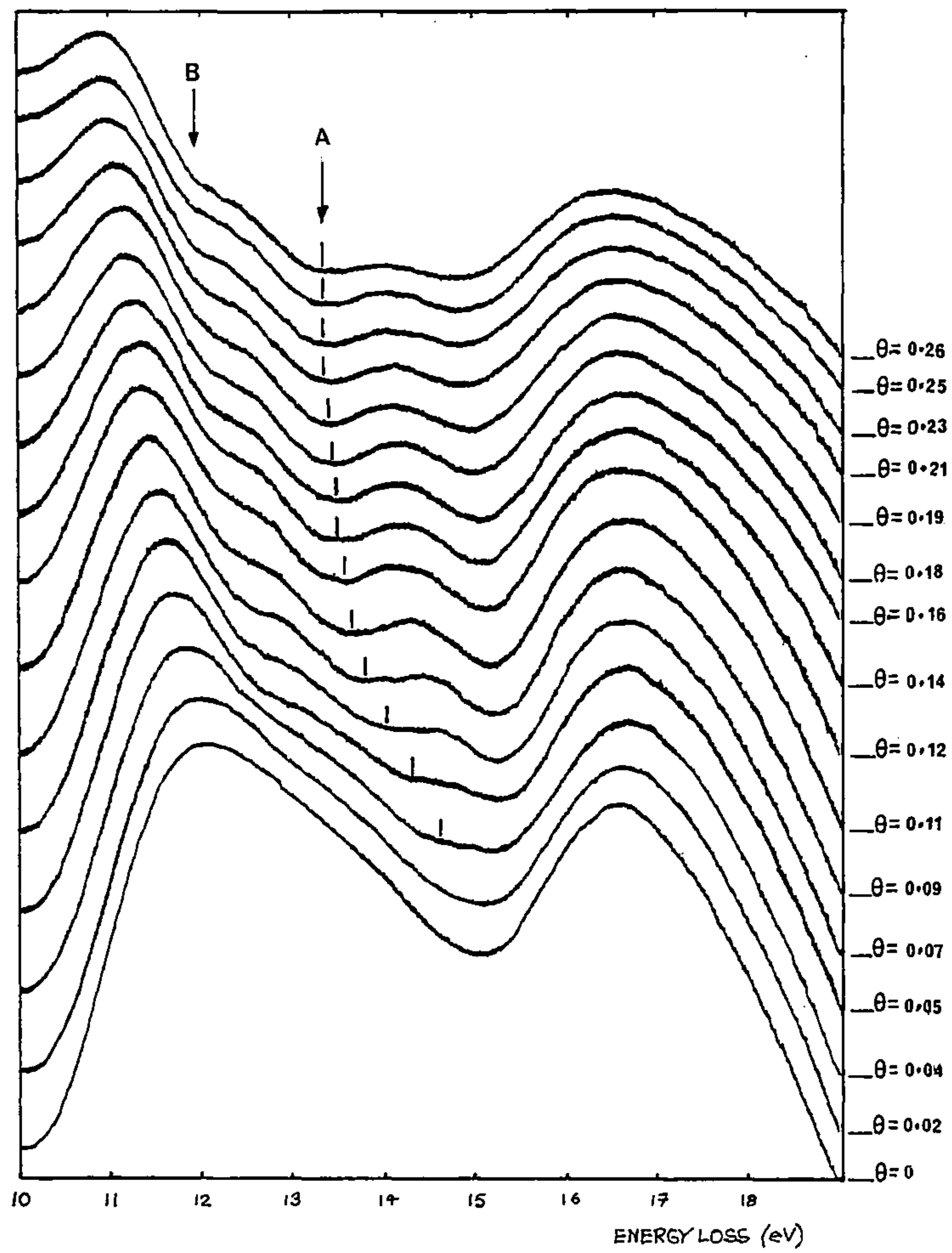

Figure 5.12: Normal incidence $\frac{dN}{dE}$ energy loss spectra as a function of caesium coverage. The primary beam energy, measured in the $\frac{dN}{dE}$ mode, is 33.8eV. Features A and B are associated with the Cs $5p_{1/2}$ and $5p_{3/2}$ core level excitation threshold.

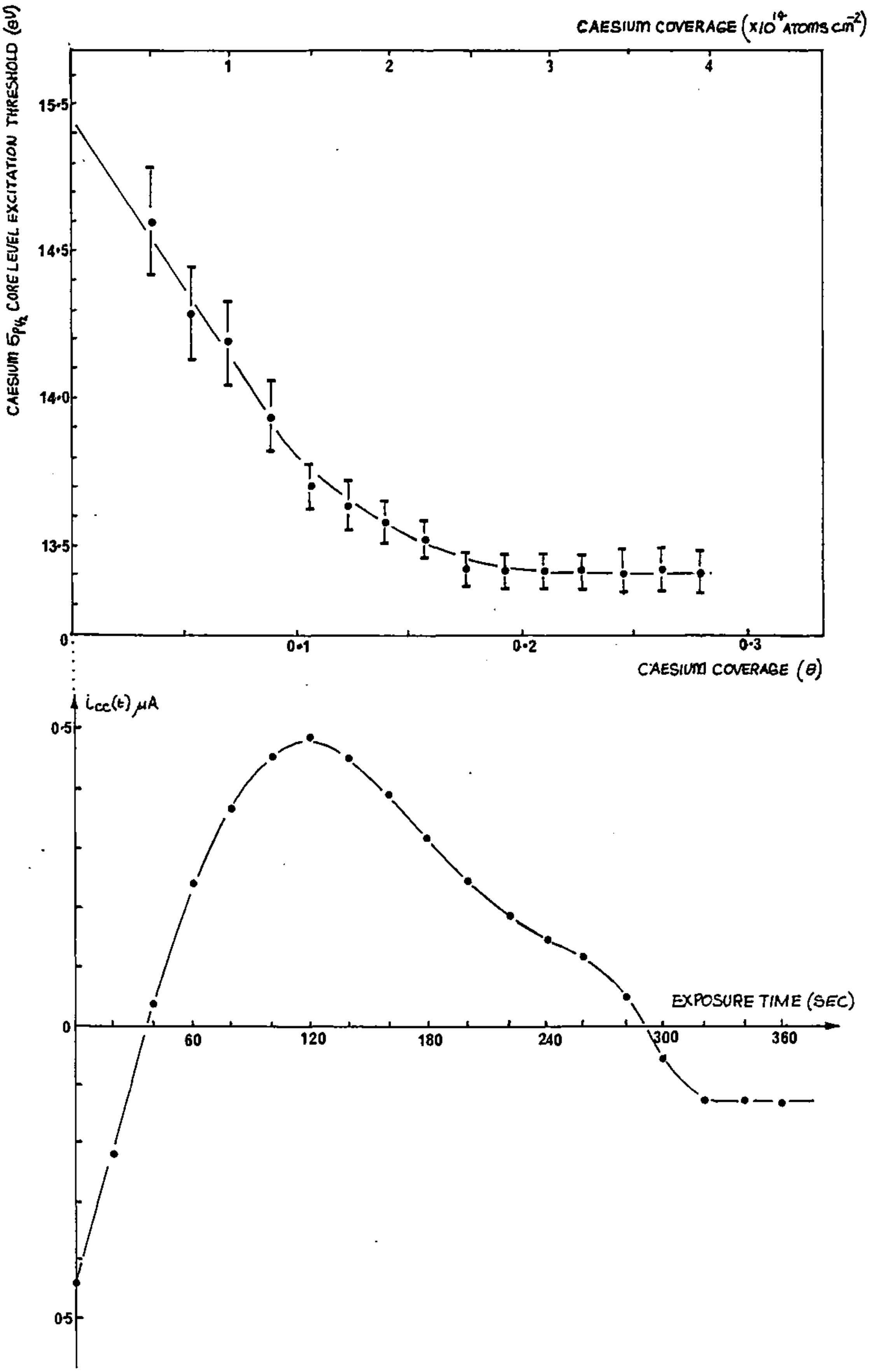

Figure 5.13: (top) Shifts in the $Cs5p_{\frac{1}{2}}$ core level excitation threshold as a function of coverage; (bottom) The accompanying crystal current measurements that were used to calibrate the coverage.

coverage range $0 < \theta < 0.28$ with most of the changes occurring before $\theta \approx 0.14$. The total shift is $\approx$ 1.5eV, which is consistent with a reversal of charge transfer during the growth of the caesium monolayer.

LINDGREN and WALLDEN (ref:- 19) who used EELS (in the $\frac{dN}{dE}$ mode) to study shifts in the core level excitation threshold of the $Cs5p_{3/2}$ level as caesium is adsorbed on Cu(111) found that it moved from a loss of 13.2eV ($\theta \rightarrow 0$) to a loss of 11.6eV ($\theta_{max} \simeq 0.25$). The total shift, 1.6eV, is in good agreement with that seen here for Cs on Al(111). Agreement between the absolute values of the core level threshold is not, of course, expected since LINDGREN and WALLDEN studied the less tightly bound $Cs5p_{3/2}$ level: in their system the Cs5p thresholds do not coincide with the substrate plasmon losses.

In contrast to the adsorption of potassium on Al(111) the adsorption of caesium does appear to be accompanied by a coverage dependent charge transfer, and this is consistent with the corresponding work function with LEED data.

Figure 5.14 shows the normal incidence N(E) spectra of a thick layer of caesium (adsorbed onto the aluminium crystal when it was cooled to liquid nitrogen temperature). Less Cs could be adsorbed than potassium in a given time, and the substrate 68eV Auger signal is not completely attenuated (see figure 5.15).

Once again, multiple plasmon losses are seen at low losses ($\approx$2;4eV): these are discussed in the next section. The Cs 5p threshold is indicated on figure 5.15 and the inflection point in its leading edge occurs at a loss of 11.8eV in good agreement with LINDGREN and WALLDEN's ($\frac{dN}{dE}$) data and photoemission experiments (ref:- 21). This

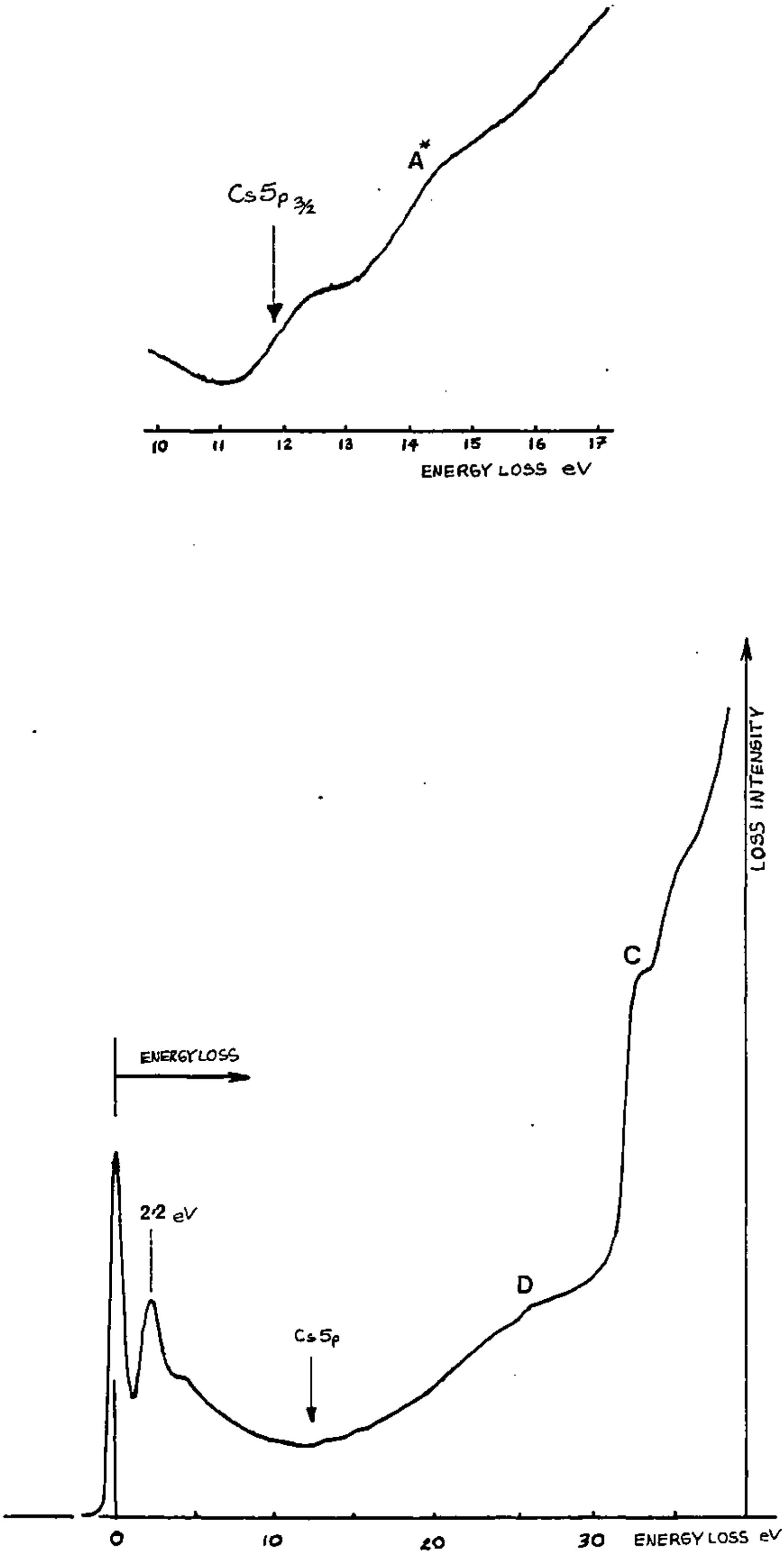

Figure 5.14: Normal incidence energy loss spectra (primary beam energy = 39.4eV) from thick films of Cs deposited on the cooled Al(111) substrate.
The spectrum at the top shows a high resolution study of the Cs $5p_{3/2\ 1/2}$ core level excitation threshold.

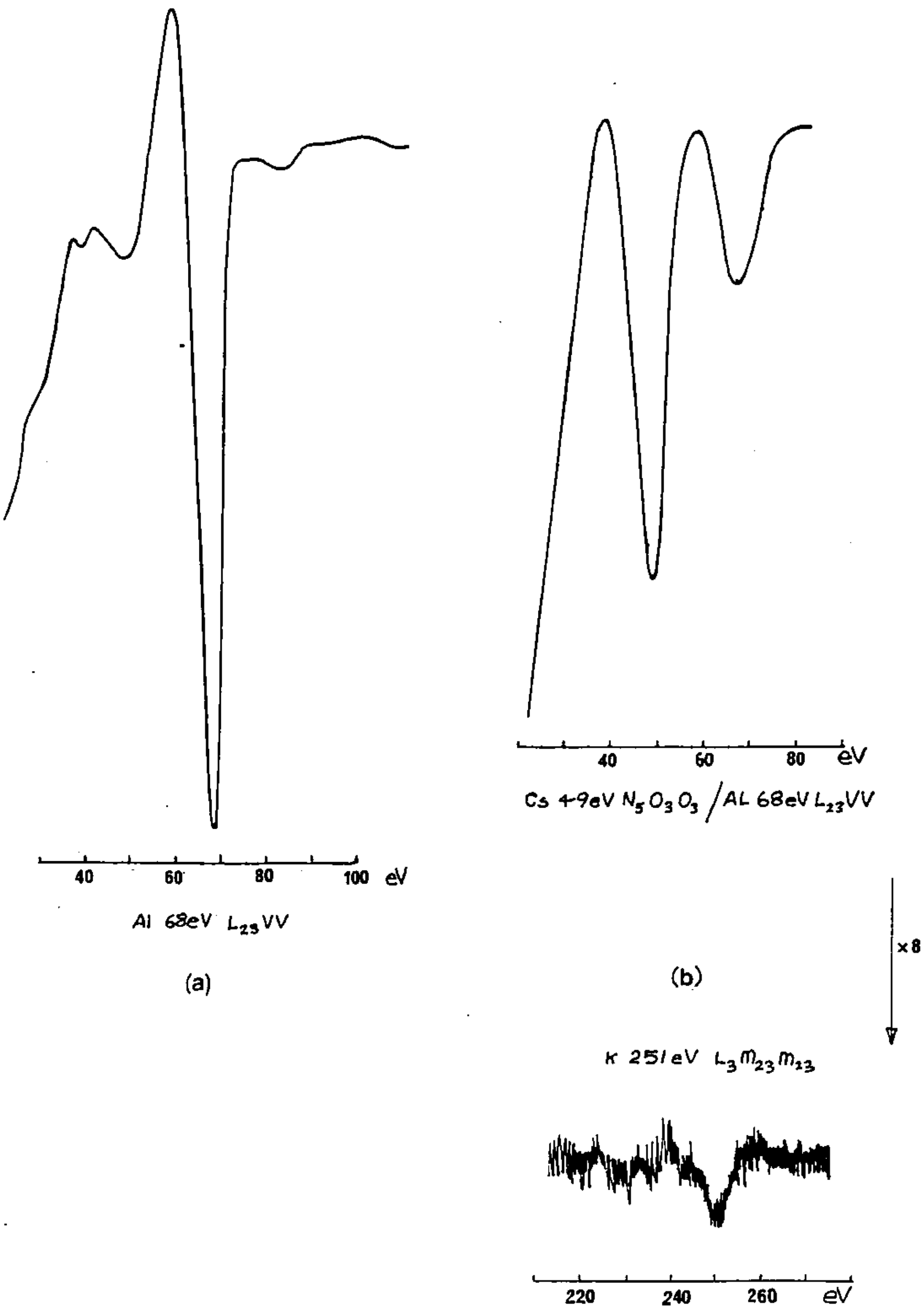

Figure 5.15: $\frac{dN}{dE}$ Auger spectra (E_p = 2.5KeV) from (a) clean Al and (b) a thick film of Cs deposited onto the cooled substrate. Insufficient Cs is deposited to completely attenuate the Al Auger feature and a small amount of K contamination was also found (see Chapter 3).

reinforces the argument in favour of associating feature B in figure 5.12 with the Cs5$p_{3/2}$ threshold. The 'hump' that occurs at a slightly larger loss, marked A*, is thought to be due to the Cs5$p_{1/2}$ threshold (c.f. A in figure 5.12), although the Cs5$p_{1/2}$ threshold would also coincide with a plasmon loss of the Cs5$p_{3/2}$ threshold. It is not thought that this would affect the measured shifts in the Cs5$p_{3/2}$ threshold at lower coverages since A and B (figure 5.12) both shift together.

The feature marked C in figure 5.14 is a Cs Auger transition and occurs at a kinetic energy relative to the analyzer of $\approx$ 7 eV. There are many Cs Auger transitions in this energy range (ref:- 11) and so it is hard to ascribe it to a specific transition.

(The feature marked D is thought to be the Cs5s threshold. It occurs at a loss of 25eV, which compares reasonably with the binding energy of the Cs5s levels 23eV (ref:- 21) and with the excitation threshold of the Cs5s levels, 27eV, of a full monolayer of Cs on Si(100) (ref:- 20). The agreement between references 20 and 21 is not so good. Feature D was not studied in detail).

5.3 Discussion of the plasmon losses in thick films of K and Cs

Table 5.1 compares the plasmon losses found in this study for K and Cs with the plasmon losses deduced from a high resolution electron energy loss experiment (ref:- 22). Also shown in the table are the theoretical values calculated from (a) the simple free electron model with $\tilde{\omega}_p = \omega_p$ (b) a much more sophisticated approach due to PAASCH

	THEORY 1 eV		THEORY 2 eV		EXPERIMENT REF 22 eV			THIS STUDY eV	
ELEMENT	$\hbar\omega_p$	$\frac{\hbar\omega_p}{\sqrt{2}}$	ΔE_p	$\Delta_{1/2}$	ΔE_p^{EXP}	ΔE_s^{EXP}	$\Delta_{1/2}^{EXP}$	ΔE	Δ
K	4·29	3·03	3·88	0·4	3·72	2·63	0·3	3·2	2·0
Cs	3·44	2·48	2·96	1·2	2·90	2·1	1·2	2·2	1·8

Table 5.1

Comparison of plasmon losses of K and Cs found here with theory and high resolution experimental data. $\hbar\omega_p$ and $\hbar\omega_p/\sqrt{2}$ are bulk and surface plasmon energies calculated with free electron theory. ΔE_p is the bulk plasmon energy calculated using a much more complicated theory due to PAASCH (ref:- 23) where band structure has been taken into account. $\Delta_{1/2}$ is the calculated half-width of the plasmon loss. ΔE_p^{EXP} and ΔE_s^{EXP} are the bulk and surface plasmon energies measured in high energy (~30KeV) high resolution experiments performed on thin alkali metal films. $\Delta_{1/2}^{EXP}$ is the measured plasmon half width. ΔE are the measured plasmon losses in this study. Due to the poorer resolution these losses are the combined surface and bulk plasmon losses and so the measured half widths Δ are much larger than expected.

(ref:- 23), who takes bandstructure (via pseudopotential) and hence plasmon damping into account.

In the high resolution experiments (ref:- 22) both the surface and bulk plamson losses of K and Cs are seen. For the K and Cs films studied in this project only multiples of one plasmon loss is seen. It is believed that this loss represents unresolved surface and bulk plasmon losses. In this experiment the measured half width of the elastic beam was taken as a practical measure of the resolution. For the beam energies used in figures 5.9 and 5.15 this half width was found to be 0.9eV. This inability to resolve the surface and bulk losses has also been encountered in other experiments with similar energy resolutions (ref:- 24). The 3.2 eV loss found here for potassium seems to be close to the average value of the high resolution surface and bulk losses. For caesium a 2.2 eV loss is found. This is almost exactly equal to the caesium surface loss found in the high resolution experiment. It is not really known why the contributions to the plasmon losses of K and Cs are different, but surface condition (roughness, contamination) and different excitation probability could account for the behaviour.

It is also difficult to estimate the half width of the plasmon losses seen in figures 5.9 and 5.14, but the half width of the Cs loss, $\approx$ 1.8, seems to be less than that of the potassium loss, $\approx$ 2.0. This, however, is reasonable because, as pointed out in the previous paragraph, the potassium loss appears to be a combined (i.e. unresolved) surface and bulk loss.

On comparing the high resolution data with theory there is a much better agreement if plasmon damping is taken into account: the half widths of the plasmons are in excellent agreement.

5.4 Investigation of the fluctuations in the crystal current on K and Cs adsorption

Throughout this work much use has been made of crystal current measurements, $i_{cc}(t)$, as a way of monitoring alkali metal uptake and/or evaporator characteristics. In Chapter 4 it was shown that the onset of the plateaus in the $i_{cc}(t)$ curves correspond to plateaus in the Auger signal versus time curves and the coverage at these points was defined as a complete monolayer. AES measurements verified that alkali metal coverage increases approximately linearly with exposure time up to these plateaus.

Figure 3.3(b) (Chapter 3) shows how the crystal current to earth varies as a function of incident beam energy ($i_{cc}(E_p)$) for clean aluminium. The form of this curve follows the form of the secondary emission yield $\delta(E_p)$ which is believed to be qualitatively similar for all materials (see review article by DEKKER, ref:- 25), that is, $\delta(E_p)$ increases with energy in the low energy region, reaches a maximum, δ_{MAX}, at a few hundred electron volts and then decreases with increasing primary beam energy.

The value of δ_{MAX} and the primary beam energy at which it occurs is not the same for all materials (ref:- 25). For most metals δ_{MAX} is greater than unity but for aluminium and the alkali metals it is less than unity. The results found here for clean aluminium (figure 3.6(b)) are therefore consistent with those previously reported since $i_{cc}(E_p)<0 \Rightarrow \delta(E_p)<1$.

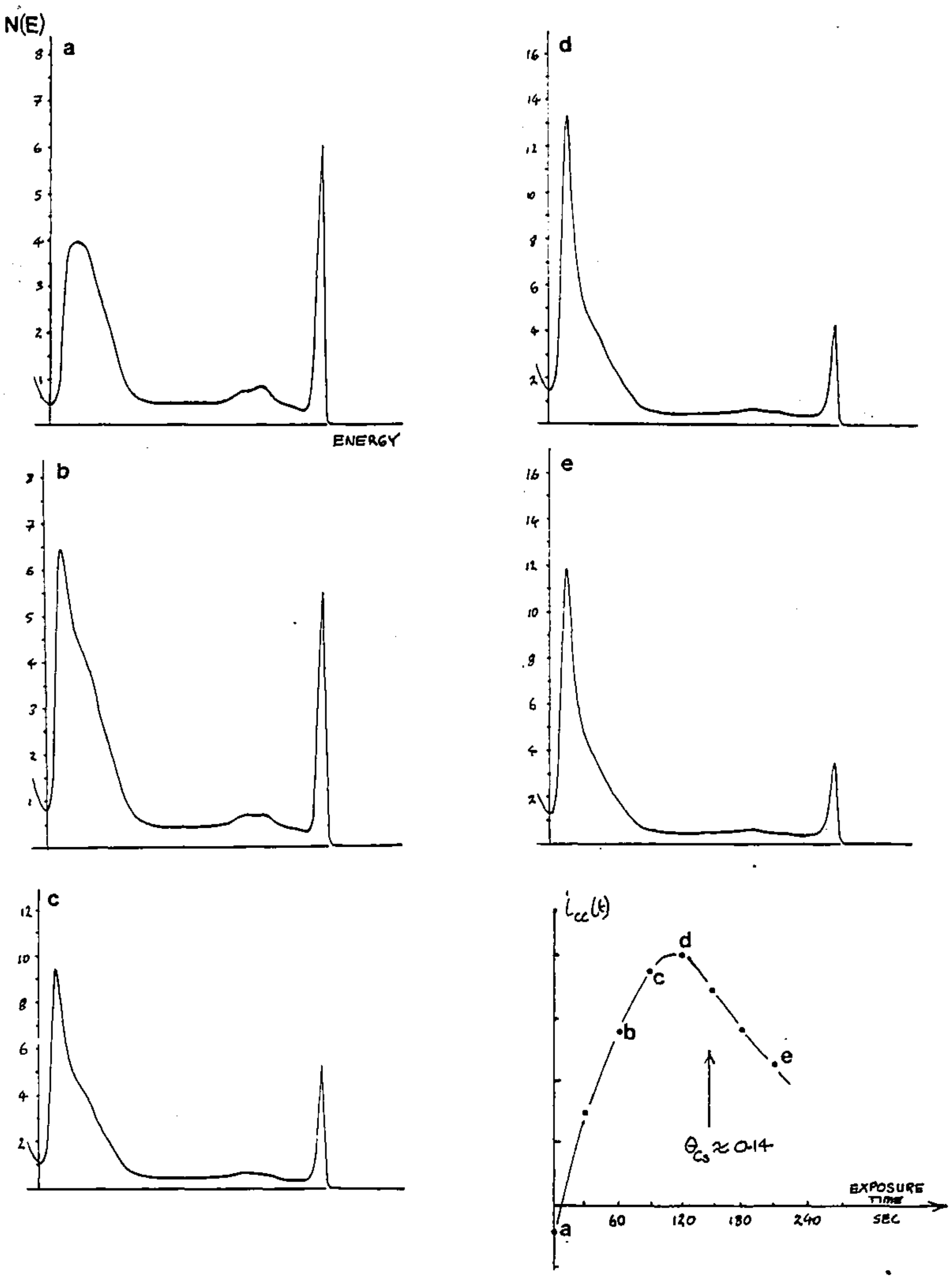

Figure 5.16: The changes in the N(E) spectra as caesium is adsorbed on Al(111) related to the crystal current measurements. Note: The different scales used on the ordinates on going from a,b ⟶ c,d,e.

Early attempts to correlate secondary electron yields directly with work functions were not successful since high work function metals tend to have high secondary electron yields, which is contrary to expectation. The greatest proportion of the secondary electron emission is due to the large peak at low energies in the backscattered electron distribution: peak C* in figure 3.9. This peak is due to a cascade process which each incident electron can initiate a whole sequence of inelastic and elastic scattering events. DEKKER, in his review article, has discussed secondary electron production in detail and has pointed out that a full quantitative description of the cascade process requires a detailed knowledge of the inelastic and elastic scattering cross sections over the entire energy range of $E_p \longrightarrow 0$ for each material. This has yet to be achieved. Superimposed on the smooth cascade predicted by simple theories may also be structure due to Auger transition (ref:- 26), plasmon decay (ref:- 27) and the effects that the band structure has on the screened electron-electron interaction (ref:- 28).

In order to investigate further the cause of the fluctuation in i_{cc} observed in this study when K or Cs was adsorbed on Al(111) (e.g. see figures 4.14 and 4.15) N(E) spectra were recorded in which the secondary electron distribution was separated from those secondaries produced in the analyser (see Chapter 3).

Figure 5.16 shows how the N(E) spectra change as Cs is adsorbed on the Al substrate. Initially, as the Cs coverage increases the size of the secondary electron cascade profile also increases. This trend continues until a maximum in the total secondary electron yield is reached at ≈ 1/2 monolayer.

Increasing the Cs coverage beyond this point, however, causes a fall in the total secondary electron cascade profile. Throughout the entire process the number of elastically backscattered electrons steadily decreases. Similar trends were observed for K adsorption, as is also reflected in the similarity between figures 4.14 and 4.15.

At maximum value, $i_{cc}>0$, which implies that $\delta_{MAX}>1$. Both aluminium and alkali metals have $\delta_{MAX}<1$, and so a premonolayer rise above $i_{cc}=0$ presumably means that i_{cc} will fall again as the adsorbed deposit becomes more bulk like. Evidently this starts to occur during the completion of the first monolayer. The plateau in the $i_{cc}(t)$ curve corresponds to the situation where the surface conditions are no longer changing - because the coverage has saturated at a complete monolayer of alkali metal and this justifies the use of the onset of the plateau as a calibration point.

The reason for the premonolayer maximum in i_{cc} (or δ) at $\approx 1/2$ monolayer coverage, however, is not clear but seems to be associated with a very sharp low energy spike in the secondary electron cascade (see figure 5.16). It has already been noted that a detailed understanding of the secondary electron cascade is complicated, and so it is not surprising that it is difficult to explain the variations of i_{cc} with coverage. The low work function of the surface at $\approx 1/2$ monolayer coverage may be a factor, but it does not explain the subsequent fall of i_{cc} - especially in the case of potassium adsorption, where the work function remains constant.

In fact, the form of the $i_{cc}(t)$ curves obtained here for K and Cs adsorbed on Al(111) are very similar to the variation in the photoelectric emission current that WANG (ref:- 29) observed as a function of caesium adsorption on W(100). He saw a submonolayer enhancement of the photoemission efficiency at about 1/2 monolayer coverage. He also points out that work function argument alone cannot explain the behaviour in a detailed way.

The variation in the crystal current to earth as a function of coverage has also been studied for other systems. RHEAD et al (ref:- 30) have compared AES, LEED and i_{cc} measurements for the following systems: Sn/Cu(111); Pb/Cu(100); Pb/Cu(410); Sn/Cu(100) and Sn/Cu(410). They found that the details of the $i_{cc}(t)$ curves appeared to depend upon the particular system. For Pb adsorption and for the Sn/Cu(111) the crystal currents were found to reach a maximum on the completion of the first monolayer. Premonolayer breaks associated with structural changes were also observed. For Sn on Cu(100) they found that a premonolayer break in the crystal currents was followed by a plateau. The end of this plateau was marked by a second break which was found to coincide with the completion of the monolayer as determined from LEED intensities. On Cu(410) the adsorption of Sn was found to cause an almost immediate sharp fall, which was ascribed to a highly disordered layer.

RHEAD et al suggest that an enhanced secondary yield may be due to electron scattering at the surface caused by the presence of the adsorbate. JONKER et al (ref:- 31), who have investigated quantum size effects in electron transmission through thin films, indirectly reinforce the arguments of RHEAD et al. They point out that as the dimensions of an adsorbed film or the structure within it become comparable to the electron's de Broglie wavelength, considerable interference and scattering may occur.

It is thought highly likely that this kind of scattering/ interference effect may be the cause of the variation in the crystal currents seen here for K and Cs adsorption on Al(111). Such a mechanism would probably not be too dependent on the work function and would therefore be consistent with figures 5.1 and 5.2. A quantitative explanation, however, cannot yet be offered.

REFERENCES

1. H.B. MICHAELSON, J. App. Physics Vol. 48 No. 11 p.4729 (1977)
2. H.B. MICHAELSON, J. App. Physics Vol. 48 No. 11 p.4729 (1977)
3. H.B. MICHAELSON, J. App. Physics Vol. 48 No. 11 p.4729 (1977)
4. S. ANDERSSON and V. JOSTELL, Surface Sci. 46 (1974) p.625
5. Introduction to Solid State Physics: by C. KITTEL (JOHN WILEY & SONS, NEW YORK 1976)
6. Excitation of Plasmons and Interband Transitions by Electrons: by H. RAETHER, SPRINGER TRACTS IN MODERN PHYSICS, VOL. 88, Ed. by G. HÖHLER (SPRINGER-VERLAG BERLIN 1980)
7. R. PARK & J. HOUSTEN, J. Vac. Sci. Technol. Vol. 10 No.1 p.176 (1973)
8. D. CHATTARJI: see bibliography Chapter 2
9. L-G. PETERSSON and S-E. KARLSSON, Physica Scripta Vol. 16 p.425 (1977)
10. G. BRODEN and H.P. BONZEL, Surface Sci. 84 (1979) p.106
11. Auger Catalogue by W.A. COGHLAN and R.E. CLAUSING (ACADEMIC PRESS NEW YORK 1973)
12. T. ISHII, Y. SAKISAKA, S. YAMAGUCHI, T. HANYU and H. ISHII. J. Phys. Soc. Jap. Vol. 42 No.3, p.876 (1977)
13. R. HAENSEL, G. KEITEL, P. SCHREIBER and B SONNTAG, Phys. Rev. Letts. Vol. 23 No.10 p.528 (1969)
14. G.D. MAHAN: Solid State Physics, ed. H. EHRENREICH F. SEITZ and D. TURNBULL, Vol.29, p.75 (ACADEMIC PRESS, NEW YORK 1974)

15. U.G. JOSTELL, Ph.D. Thesis, Chalmers University of Technology, Göteborg, Sweden (1979)

16. H. TOCHIHARA, Surface Sci. 126 (1983) p.532

17. L. SURNEV and M. TIKHOV, Surface Sci. 118 (1982) p.267

18. V.E. HEINRICH, Appl. Surface Sci. 6 (1980) p.87

19. S.A. LINDGREN and L. WALLDEN, Phys. Rev. B vol. 22 no.12 p.5967 (1980)

20. H. TOCHIHARA and Y. MURATA, J. Phys. Soc. Jap. vol.51 no.9 p.2920 (1982)

21. J.A. BEARDEN and A.F. BURR, Rev. Mod. Physics, Vol.39 No.1 p.125 (1967)

22. C. KUNZ, Z. Physik 196 p.311 (1966)

23. G. PAASCH, Physica Status Solidi 38 K123 (1970)

24. J.B. SWAN, Phys. Rev. vol. 135 No.5A A1467 (1964)

25. A.J. DEKKER: Solid State Physics ed. by F. SEITZ and D. TURNBULL vol. 6 p.251 (ACADEMIC PRESS NEW YORK 1958)

26. C.N. BERGLUND and W.E. SPICER, Phys. Rev. vol. 136 A1030 (1964)

27. M.S. CHUNG and T.E. EVERHART, Phys. Rev. B vol.15 4699 (1977)

28. E.O. KANE, Phys. Rev. vol. 159 p.624 (1967)

29. CHEN-SHOW WANG. J. Appl. Physics vol. 48 No.4 p.1477 (1977)

30. C. ARGILE and G.E. RHEAD, J. Phys. C: Solid State Phys. 30 (1982) L193

31. B.J. JONKER, N.C. BARTELT and R.L. PARK, Surface Sci. 127 (1983) p.183

CHAPTER 6

SUMMARY, CONCLUSIONS AND RECOMMENDATIONS

6.1 Summary

In Chapter 1 the basic theory of alkali metal chemisorption was outlined. It was noted that when alkali metals are adsorbed on transition metals, the work function passes through a minimum at some submonolayer coverage. LANGMUIR has pointed out that this behaviour is due to charge transfer between the adsorbate and the substrate which leads to the formation of a dipole layer, and it is this which substantially lowers the work function at low coverages. As the coverage increases the dipole layer becomes depolarised and the work function rises to a value close to that of the bulk metal at $\approx$ 1 monolayer. The quantum mechanical picture of alkali atom chemisorption due to GURNEY revealed the details of the charge transfer process and the atomic origin of LANGMUIR's depolarising effect.

Theoretical attempts at calculating the work function/coverage curve using the atomic picture of adsorption, however, are hampered because a knowledge of several parameters is required as a function of coverage (e.g. the position and width of the valence resonance and the separation between the centre of the adsorbate and the ions in the surface of the substrate) - and not all of them can yet be determined without comparison with experiment.

LANG avoided this problem by using an extremely simple jellium model and generated work function/coverage curves using the successful local density functional theory. Surprisingly, LANG's results reproduce the experimental trends very well and it is expected that the agreement would be even better for alkali metal adsorption on aluminium - i.e. good "free electron"metals.

In Chapter 2 the experimental data was discussed in more detail. For transition metal substrates it was noted that the form of the work function/coverage curve becomes more pronounced for adsorption on the smoother planes and in the sequence Na $\longrightarrow$ Cs. LEED studies indicate that the alkali metal adatoms form structures that maximise the adatom-adatom separation at all coverages - which is to be expected since the adatoms are charged to some extent and will therefore repel each other. In addition to this it has been found that incommensurate hexagonal close packed structures are usually formed at full monolayer coverage on the low index substrate planes. This indicates that such substrate planes have little effect on the ordering of the adlayer.

Almost all of the available data, however, is for adsorption on transition metals and so exact agreement with theory is not expected. Data on alkali metal adsorption on simple ('free electron') metal substrates is extremely sparse and (until this study) almost entirely due to PORTEUS' work on the adsorption of sodium on Al(111) and Al(100).

PORTEUS found no minima in the work function/coverage curves and observed LEED pattern changes that would be interpreted in terms of island growth. Both of these observations contrast with the simple theoretical modes of Chapter 1 and with the trends observed for alkali metal adsorption on transition metals.

From the LEED patterns PORTEUS concluded that when sodium is adsorbed on Al(111) a well developed ($\sqrt{3}$ x $\sqrt{3}$)R30° structure is formed by θ = 1/3 and domains of p(2x1) structure are formed by θ = 1/2. On the Al(100) surface he concluded that Na forms a c(2x2) structure by θ = 1/2 and that at higher coverages a hexagonal structure is formed.

Some of PORTEUS' results were reproduced by HUTCHINS et al in their full LEED study of the Na c(2x2)/Al(100) structure. Their LEED calculations placed the sodium atoms in high co-ordination 4-fold hollow sites (which is reasonable), but also indicated that the size of the sodium adatoms is greatly reduced. The calculations were repeated by VAN HOVE et al, and the same results were obtained; neither group of workers, however, comment on the small size of the sodium adatoms implied by their calculations.

In Chapters 4 and 5 the results of the author's work on the adsorption of potassium and caesium on Al(111) are presented.

Potassium adsorption was found to produce exactly the same sequence of diffraction pattern changes as that seen by PORTEUS for Na on Al(111) and again no minimum in the work function/coverage curve was observed. Therefore the adsorption of K on Al(111) would also seem to contrast with the simple theories of Chapter 1 and with the adsorption of alkali metal on transition metals. However, the LEED pattern changes that occurred after the formation of the K($\sqrt{3}$ x $\sqrt{3}$)R30° structure (θ_K = 1/3) took long exposure times to produce and did not appear to be accompanied by an expected increase in the potassium coverage. In addition to this, the use of PORTEUS' interpretation of the final diffraction pattern in terms of domains of p(2x1) was found to be incompatible with a hard ball model based on metallic radii - even for the case of Na on Al(111). It has already been noted, however, that for Na on Al(100), LEED calculations do imply such a contraction the size of the adatoms.

It was suggested that the final diffraction pattern change (i.e. after the formation of the ($\sqrt{3}$ x $\sqrt{3}$)R30° structures) was due to residual contamination in the alkali metal fluxes - in PORTEUS' case the fact that the sodium coverage was seen to increase throughout the LEED pattern sequence may have contributed towards the illusion that sodium was solely responsible for the observed structures.

In this study no impurities were seen, and so it is not known whether this explanation is correct or whether the observations are a manifestation of some other effect. The formation of a surface alloy has not been ruled out.

In Chapter 5 the study of core level excitation thresholds as a means of qualitatively probing the charge state of an adsorbate was discussed. For alkali metal adsorption on transition metals, shifts are observed that imply a decrease in the binding energy with coverage which is consistent with the gradual reversal of charge transfer which occurs during the growth of the first atomic layer.

When potassium is adsorbed on Al(111) no shifts are observed during the growth of the monolayer, even during the coverage range where the work function is falling. This suggests that the potassium layer is essentially neutral at all coverages, in agreement with the LEED observations which, just as in the case of Na on Al, imply 2-dimensional island growth - and this would not be expected to occur if the adatoms were highly charged.

The adsorption of caesium on Al(111), however, produced results that are more typical of alkali metal adsorption and imply initial charge transfer. An expanding spot pattern was seen in the LEED study and the work function passes through a distinct minimum during the growth of the monolayer. In addition to this, shifts in the Cs5p$_{3/2,1/2}$ core level excitation thresholds were observed - and these agreed well with existing data for Cs on Cu(111).

In spite of the apparent differences between the adsorption of Cs and K on Na on aluminium (111) important similarities do exist. The structure adopted by all three alkali metals on Al(111) are greatly influenced by the periodicity of the substrate. This in itself is not necessarily surprising since one would expect that adsorbed atoms would be attracted to the periodic array of potential minima of the substrate surface. However, the same alkali metals generally show much less evidence of this effect when adsorbed on transition metals - although it should be noted that the lattice constants of transition metals are generally smaller than those of Al, and so transition metal surfaces are likely to be 'smoother' anyway.

PORTEUS explains his results by suggesting that the observed behaviour is indicative of a more metallic bonding between sodium and aluminium and that the sodium adlayer is depolarised at much lower coverages than is normally expected, thus allowing the overlayer to be more sensitive to the structure of the substrate.

The results presented here for potassium adsorption on Al(111) are similar to those of PORTEUS for Na on Al(111) and the extra information gained from the core level excitation threshold study implies that the potassium layer is essentially neutral at all the submonolayer coverages studied.

The adsorption of caesium on Al(111), however, appears to be accompanied by significant charge transfer and the LEED work function and core level excitation thresholds show trends which are indicative of this.

Throughout this present project great care was taken to ensure that the alkali metal layers that were studied were as clean as possible and deposited onto clean surfaces. It is not known, however, to what extent this has been successful. The most important contaminant is probably oxygen, due to its strong interaction with alkali metals and aluminium. In Chapter 3 it was estimated that as little as 1/10th of a monolayer of oxygen could be detected - and no contamination of the layers could be seen. PORTEUS, however, is able to detect some oxygen contamination which he estimates to constitute at most 13% of the adsorbed layer. He believes this to have little effect on the results. HUTCHINS et al quote a much smaller oxygen contamination level, 5% of a monolayer, and although they did not study sodium adsorption as a function of coverage, the fact that annealing was required in order to obtain good diffraction patterns is not inconsistent with island growth.

In the second part of Chapter 2 existing coadsorption studies on transition metals were reviewed in an attempt to assess how the properties of adsorbed alkali metal layers could be affected by contamination. It was noted that the coadsorption of alkali metals and small quantities of oxygen appeared to exaggerate the form of the work function/coverage curve. The double-layer model is often used to explain this behaviour, i.e. that the oxygen is located between the (saturated) alkali metal layer and the substrate. If this model is correct, then the Auger signals from the oxygen layer will be attenuated by the alkali metal layer and this may cast doubt on the values of the estimated contamination levels quoted in the previous paragraph. The location of the contamination must be known or found.

It was also noted that when alkali metals are adsorbed on oxidised transition metal substrates no minimum in the work function/coverage curves is seen. This behaviour, however, is also displayed by the adsorption of sodium and potassium on 'clean' aluminium.

6.2 Conclusions

It may well be that the behaviour observed here for K and Cs adsorption and that seen by PORTEUS for Na adsorption is truly representative of the nature of the aluminium-alkali metal bond and that this bond becomes less metallic and more ionic in the sequence Na ⟶ Cs. For K or Na adsorption a more metallic bond would be formed if the sharing of the adatom and substrate electrons was more equal. This would occur if the valence resonances of the adsorbates were broadened to such an extent that their widths were no longer small compared with the conduction band width of the aluminium substrate. This would result in a considerable mixing of adsorbate and substrate electron-states and may account for the greater influence that the periodicity of the substrate would appear to have on the overlayers. As a corollary to this, LEED studies for Na on Al(100) do imply a smaller than expected Na - Al bond length, which would mean that the valence levels of the sodium adatom would be broadened more than expected. In particular, it may be possible that the apparently anomalous sequence of diffraction patterns seen for Na and K on Al(111) is a consequence of some form of unexpected surface alloying or reconstruction. If this is the case, then the simple theories of Chapter 1 would not be expected to be applicable. LANG's model uses a discrete slab characterised by a variable density and the atomic model requires that the adatoms retain their atomic nature: the mixing between atomic and substrate states is assumed small.

However, there is another simpler explanation of the observed behaviour that cannot be ignored. This explanation is suggested by the suspicions which arose about the origin of the structures seen for K on Al(111) where it may be argued that:

* (undetected) residual impurities were present in the potassium flux;

* that these encouraged the nucleation of potassium atoms and hence island growth;

* that this led to the observed LEED pattern changes and in particular to the final diffraction pattern;

* and that under these conditions coverage dependent charge transfer would not be expected and that the work function curve would therefore not display a minimum.

If this explanation is correct (see next section), then doubt must be cast on PORTEUS' results for the adsorption of Na on Al(111) and Al(100) and possibly also on the experimental data that HUTCHINS et al and VAN HOVE et al used in their calculations.

Because of the suspicion that contamination may be responsible for some of the observations it is felt that it would be premature at this stage to make any definite conclusions about the nature of the alkali metal - aluminium bond.

6.3 Recommendations

It is therefore strongly recommended that experiments be performed to explicitly investigate how contamination would affect adsorbed alkali metal layers on aluminium. With hindsight (!) an obvious future experiment would be to investigate how a pre-prepared $(\sqrt{3} \times \sqrt{3})$R30° structure of K or Na on Al(111) is affected by the introduction of a small amount of oxygen (for example) into the vacuum system. If the suspicions are correct, then a diffraction pattern of p(2x2) symmetry may be formed. If this proves not to be the case then the possibility of surface alloying or reconstruction must be thoroughly investigated. For this, full LEED intensity analysis would be required in order to find the contents of the primitive unit cell of the surface structure. Information about how the valence band local density of states at the aluminium surface is changed by alkali metal adsorption would also be very useful. Ultra-violet photoelectron spectroscopy could provide such information and may indicate the likelihood of alloy formation.

Crystal current measurements have been very useful throughout this study as a simple means of calibrating the alkali metal coverage - once they, themselves, were calibrated against AES measurements. The origin of the rapid fluctuation in the crystal currents as a function of alkali metal coverage, however, is not fully understood. A scattering-interference mechanism would seem to be the most likely explanation. It is recommended that experiments should be performed to study the angle resolved backscattered electron energy distribution as a function of primary beam energy and adsorbate coverage in an attempt to isolate the main processes more clearly.

APPENDIX 1

Na/Al(100)

Preliminary experiments were performed on the adsorption of sodium on Al(100). The aluminium crystal was prepared in exactly the same way as is described in Chapter 3, except that it was spark machined into a thin rectangular block. S.A.E.S. getters were used as the source of the sodium. The experiments ran into serious difficulties from the start, because it was not possible to use the sodium Auger signals to monitor the sodium coverage. (The use of crystal current measurements had not yet been considered). Sodium has two prominent sets of Auger transitions; the KLL transitions that occur in the energy range $900 \longrightarrow 1000$ KeV and the $L_1L_{23}M_1$ and $L_{23}M_1M_1$ transitions that occur in the energy range $20 \rightarrow 30$ eV (ref:- 1). The high energy transitions were found to be too weak to be used with the retarding field analyser used in this study (i.e. with a primary beam energy of 2.5 KeV and 5V pK-pK modulation), as has been found by others using similar spectrometers (ref:- 2,3,4). Conversely, the very low energy sodium transitions occur at an energy where the secondary electron cascade (whose profile will be altered by sodium adsorption anyway, c.f. figure 5.16) is very steep, and so these transitions could not be used to monitor coverage either.

Nevertheless, some useful results were obtained. In agreement with PORTEUS and HUTCHINS et al, it was observed that at low coverages ($\theta_{Na} \approx \frac{1}{2}$) sodium forms a c(2x2) structure on the aluminium (100) surface (see figure A1.1). Moreover, some evidence of a beam annealing effect was found. So much sodium could be deposited onto the crystal at room temperature that its surface assumed a milky appearance.

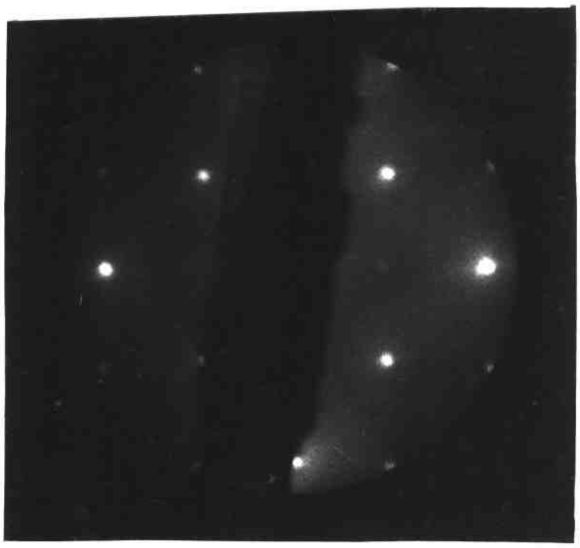

Photo k : Na/Al(100)

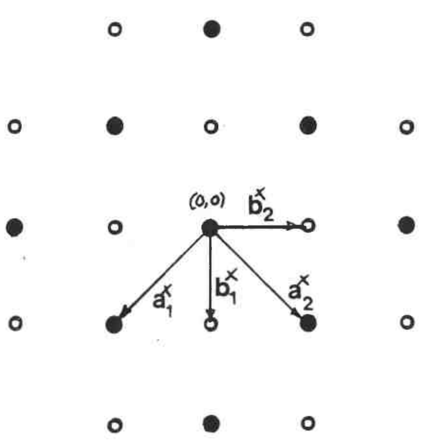

LEED PATTERN OF PHOTO K

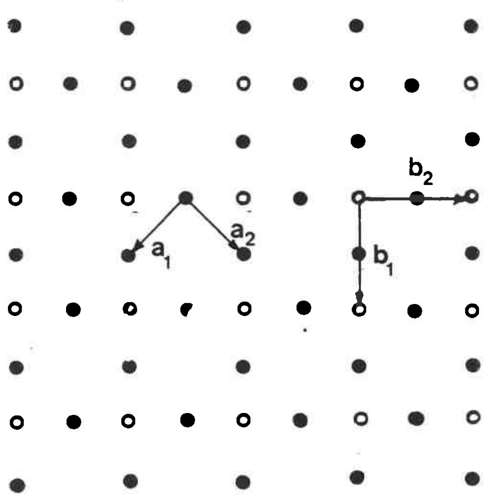

c(2x2) Na/Al(100) STRUCTURE

a_1 & a_2	are the lattice vectors of the Al(100) surface
$a_1^{\times}$ & $a_2^{\times}$	are the corresponding reciprocal lattive vectors
$b_1^{\times}$ & $b_2^{\times}$	are the reciprocal lattive vectors of the Na structure
b_1 & b_2	are the corresponding real space vectors

Figure A1.1: (top) normal incident LEED pattern beam energy = 91eV of sodium on Al(100) which is shown to be due to a Na c(2x2) structure (bottom)

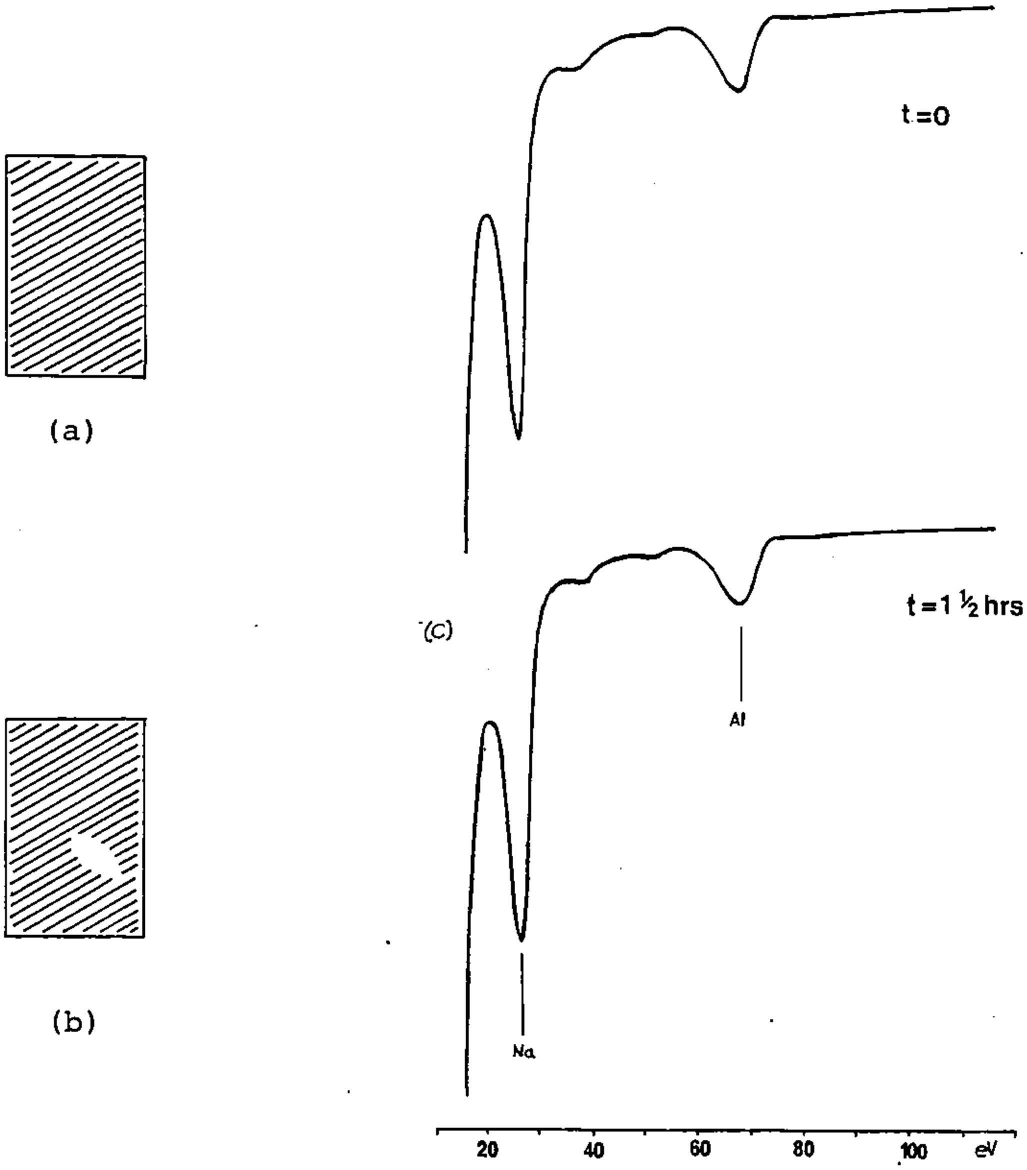

<u>Figure A1.2</u>: (a) is a schematic diagram of the front of the Al(100) sample after a thick layer of sodium has been deposited. The shading represents the 'milky' appearance of the sodium layer; (b) shows the effect that the Auger beam has on this deposit - the unshaded area is the shiny Auger beam impact area; (c) shows the accompanying $\frac{dN}{dE}$ Auger data at $t = 0$ and after 1½ hours of continuous exposure to the Auger primary beam (E_p = 1KeV, 5V pK-pK mod, $\approx 4\ \mu$Amps).

After an attempted AES study, however, a small patch of shinier surface could be seen (see figures A1.2(a) and (b)). It was found that this shiny patch coincided with the AES beam impact area. At first, diffusion or desorption from the beam impact area was suspected - leaving behind perhaps only a very thin layer of Na. However, on comparing the AES signals that were measured immediately after deposition with those measured ~1½ hours later (by which time the shiny area had appeared) it was found that there was apparently no large loss of sodium from the sampled region. These spectra are shown in figure A1.2(c) where the peak at 68eV is the $L_{23}VV$ (dN/dE) Auger signal of the aluminium substrate that has been greatly attenuated by the thick layer of sodium. The features at 27eV is due to one, or a combined mixture, of the aforementioned low energy sodium Auger transition.

It is likely, therefore, that initial sodium deposition results in a rough layer that is annealed by the energetic primary electron beam to produce a locally smoother deposit with little loss of material due to desorption or diffusion outside the beam impact area. In principle this type of growth mode (a new layer started before the previous one had been completed) can be investigated using AES - but for reasons already mentioned, in this case this was not possible.

References

1. Auger Catalogue by W.A. COGHLAN and R.E. CLAUSING (ACADEMIC PRESS NEW YORK 1973)
2. S. THOMAS and T.W. HAAS, J. Vac. Sci-Technol. Vol. 9 No.2 p.840 (1972)

3. S. THOMAS and T.W. HAAS, J. Vac. Sci. Technol. Vol.10 No.1 p.218 (1973)

4. R.A. MARBROW and R.M. LAMBERT, Surface Sci. <u>61</u> (1976) p.329.

Appendix 2

MICRODENSITOMETRY

In order to find the intensity profile of the LEED beams, photographs of the LEED patterns were taken. A JOYCE, LOEBL AUTODENSIDATER microdensitometer was used to obtain the profiles of the LEED spots in terms of optical density units (D). Optical density units are defined by

$$D = \mathrm{Log}_{10} I_i - \mathrm{Log}_{10} I_t \qquad \text{A2.1}$$

where I_i is the light incident on the negative and I_t is the light transmitted.

This particular microdensitometer works by scanning a narrow slit-shaped detection aperture through the image of the spot and automatically plotting density units as a function of position (x) along the negative. Strictly speaking, the machine gives the convolution of the aperture shape with the spot intensity perpendicular to the direction of scan - because the aperture is a slit of finite extent. See figure A2.1. To reduce this effect a narrow, short slit (i.e. less than half the estimated spatial extent of the diffraction spot) was used.

The density profiles so obtained can be related back to the intensity of the light that was originally responsible for the image, once the 'characteristic curve' of the film is known. This curve relates the energy of the incident light (i.e. intensity x exposure time) to the optical density of the film after processing. Of course there are many factors other than the energy of the incident light that can affect this curve, e.g. the type of films and the processing conditions, but since we are primarily interested in comparing profile shapes these will be ignored.

The film used for the photographs was ILFORD HP5. This is quite a fast film, and so a fine grain developer, ILFORD MICROPHEN, was used. The characteristic curve for this type of film is shown in figure A2.2 and the film exposure time (t) and camera aperture were chosen so that the linear portion of this curve could be utilised. Hence

$$D = \gamma \operatorname{Log}_{10}(It) + C \qquad \text{A2.2}$$

where I is the incident light intensity, γ = gradient of linear portion of the curve and C is a constant. It should be remembered that in this present case both D and I are functions of position.

Because the signal intensity (I^S) that we are interested in will be superimposed on a background signal (I^B), the total intensity impingeing on the film is

$$I^{S+B} = I^S + I^B \qquad \text{A2.3}$$

hence $I^S = I^{S+B} - I^S = I^B\left[\frac{I^{S+B}}{I^B} - 1\right]$ A2.4

Using equation A2.2, we may write

$$\left[\frac{I^{S+B}}{I^B} - 1\right] = \left\{10^{\Delta D/\gamma} - 1\right\} \qquad \text{A2.5}$$

where ΔD is the difference between the total measured density and an estimated local background density. Therefore

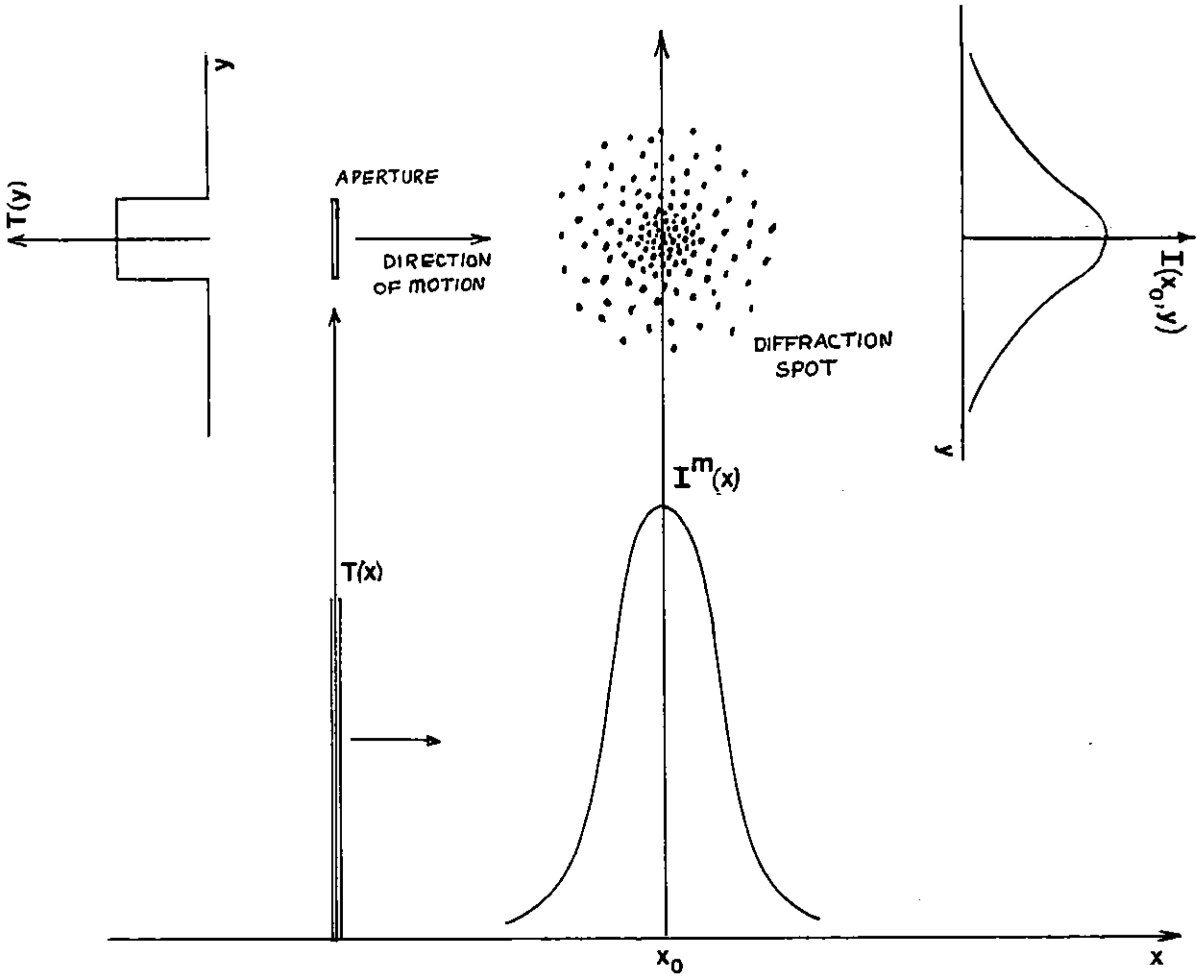

Figure A2.1: Schematic representation of the factors that contribute to the final measured intensity profile. T(x) and T(y) are the transfer functions of the microdensitometers aperture in the x and y directions. Because the slit scans the diffraction spot the measured intensity profile is

$$I^m(x) = T(x) * T(y) * I(x, y)$$

Since T(x) is approximately a delta function for narrow slits,

$$I^m(x) = T(y) * I(x, y)$$

For example, the measured intensity at x_0 is

$$I^m(x_0) = T(y) * I(x_0, y)$$

Hence, by making the slit lengths small $I^m(x_0) \longrightarrow I(x_0)$ the true intensity. In practice, however, a compromise must be reached in order to obtain sufficient signal strength and so a slit length slightly less than the estimated FWHM of the diffracted spot intensity was used.

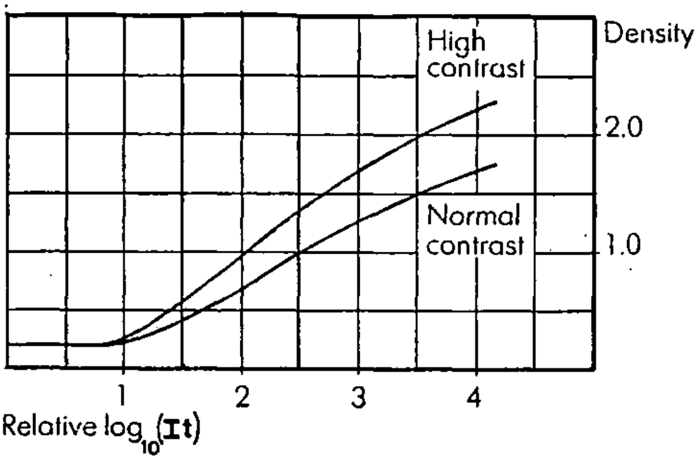

Figure A2.2: The characteristic curve for Ilford HP5 film. A high contrast fine grain developer was used.

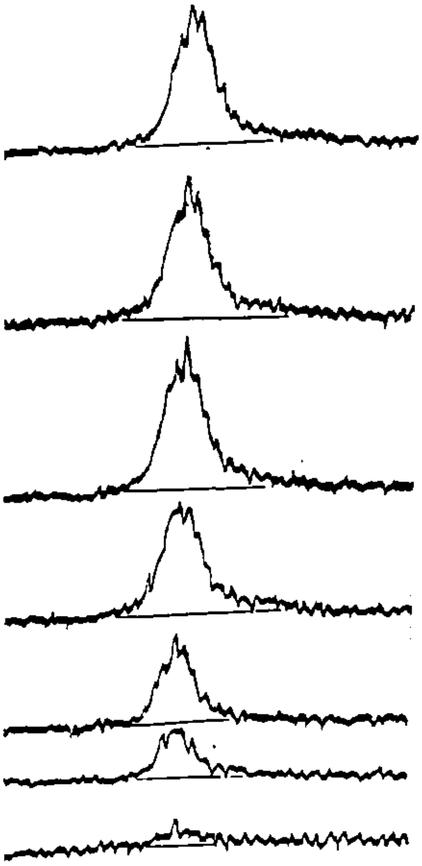

Figure A2.3: The measured optical density profiles of the K $(\sqrt{3} \times \sqrt{3})$R30° beams. These profiles were used to construct the intensity profilesof figure 4.7 and were 'hand smoothed' before using equation A2.6.

intensity profiles can be found from the measured density profiles using

$$I^{S}(x) \propto \left\{ 10^{\Delta D(x)/\gamma} - 1 \right\} \qquad \text{A2.6}$$

The main interest in this analysis was to study the FWHM of the $(\sqrt{3} \times \sqrt{3})R30°$ diffracted beams as a function of K coverage (see Chapter 4, section 4.2). The major source of uncertainty in these measurements was caused by the fact that the grids in the LEED optics were not fine enough. This causes the image of the diffraction beams to have a 'speckled' appearance, as can be seen in the photographs of Chapter 4. This effect accounts for the very rough profile of the raw data, e.g. figure A2.3. It is quite likely, therefore, that small changes in the FWHM of the beam profiles would go undetected.

For some experiments a measure of the total beam intensity was required. This was found by integrating the area under the intensity profile using Simpsons rule.

More information on the extraction of intensity information from photographic negatives may be found in:-

IMAGE SCIENCE: J.C. DAINTY & R. SHAW (Academic Press, 1974).

ACKNOWLEDGEMENTS

I should like to acknowledge the help of my supervisor, Dr. P.J. Dobson and the help of Drs. P.R. Webber and T. Gardiner. Thanks are also due to Dr. R. Tuck (E.M.I., Hayes, Middlesex) for his help with the laser welding of the samples.

I should also like to thank my family and my friends and, in particular, Isobel, for their support and encouragement throughout this work.

Deanne, thank you for typing this thesis.